

Master Thesis

Development of Calibration Methods for
the New T2K Neutrino Detector SuperFGD and
Evaluation of New Wavelength Shifting Fiber
(T2K実験における新型ニュートリノ検出器
SuperFGDの校正手法開発と
新型波長変換ファイバーの性能測定)

January 26, 2023

Department of Physics, Graduate School of Science
The University of Tokyo
東京大学大学院理学系研究科物理学専攻

Shoma Kodama
児玉将馬

Abstract

This thesis describes the calibration method developed for the new near detector of the T2K experiment, SuperFGD (Super Fine Grained Detector). SuperFGD consists of about two million scintillator cubes. The scintillation light is collected and transported by the wavelength-shifting fiber and detected at the MPPC. The precision of light yield and timing calibration is evaluated using Monte Carlo simulations of cosmic ray events. The achievable light yield uniformity with one day of cosmic ray data acquisition is estimated to be 3.6%, 4.5%, and 2.7% for x , y , and z fibers, respectively. The expected precision of timing calibration for time offset and time-walk is 0.30, 0.33, and 0.29 ns for x , y , and z fibers, respectively. They are all within requirements, and the calibration methods have been established.

We also report the measurement of the decay time of newly released wavelength shifting fibers, YS-2, 4, and 6. The YS series fibers are announced to have a faster response compared to Y-11. Our measurement results are:

$$\tau(\text{Y-11}) = 7.159 \pm 0.024 \text{ (stat.)} \pm 0.065 \text{ (syst.)}$$

$$\tau(\text{YS-2}) = 3.695 \pm 0.011 \text{ (stat.)} \pm 0.065 \text{ (syst.)}$$

$$\tau(\text{YS-4}) = 2.063 \pm 0.014 \text{ (stat.)} \pm 0.065 \text{ (syst.)}$$

$$\tau(\text{YS-6}) = 1.502 \pm 0.008 \text{ (stat.)} \pm 0.065 \text{ (syst.)}.$$

We confirm that the decay time of the YS series is shorter than that of Y-11.

Contents

1	Neutrino Oscillation and Interaction	5
1.1	Neutrino oscillation	5
1.1.1	Neutrino mixing	5
1.1.2	Neutrino oscillation in vacuum	6
1.1.3	CP violation	6
1.2	Neutrino interaction	7
1.2.1	Charged-current quasi-elastic scattering (CCQE)	7
1.2.2	Charged-current resonance scattering (CC RES)	8
1.2.3	Charged-current deep inelastic scattering (CC DIS)	9
1.2.4	Nuclear effect	10
2	T2K Experiment	11
2.1	Overview	11
2.2	J-PARC accelerator and T2K neutrino beamline	11
2.2.1	J-PARC accelerator	11
2.2.2	Neutrino beamline	12
2.2.3	Off-axis method	13
2.3	Near detectors	14
2.3.1	ND280	14
2.3.2	INGRID	15
2.4	Far detector (Super-Kamiokande)	15
2.5	Latest results on δ_{CP}	16
2.6	Limitation of the current ND280	16
2.6.1	High angle scattered particles	16
2.6.2	Low momentum particles	17
2.6.3	Electron neutrino interactions	17
2.7	T2K-II	17
2.7.1	Beam Upgrade	18
2.7.2	SK-Gd	18
2.7.3	ND280 Upgrade	18
3	SuperFGD	22
3.1	Components	22
3.1.1	Scintillator cubes	22
3.1.2	Wavelength shifting fiber	22
3.1.3	Multi-pixel photon counter (MPPC)	23
3.1.4	Electronics	24

3.1.5	LED calibration system	24
3.2	Expected performance	27
3.2.1	High angle scattered particle	27
3.2.2	Low momentum particle	27
3.2.3	Electron neutrino	27
3.3	Calibration and necessary measurement	29
3.3.1	Pedestal and gain calibration	29
3.3.2	Fiber calibration	29
3.3.3	Scintillator cube properties	29
3.3.4	Timing calibration	29
3.3.5	Position allignment	30
3.4	Plan of the construction and installation	30
3.4.1	Construction	30
3.4.2	Commissioning and installation into the ND280 pit	31
3.5	Subject of this thesis	32
3.5.1	Calibration and measurement for SuperFGD	32
3.5.2	Measurement of new types of wavelength-shifting fiber	32
4	Simulation of Cosmic Ray Events	33
4.1	Geant4 simulation	33
4.2	Detector response simulation	34
4.2.1	Energy and number of photons	35
4.2.2	Timing	37
4.2.3	Example of generated cosmic event	37
4.3	Estimation of cosmic event rate and required time	39
5	Basic Light Yield Calibration	40
5.1	Motivation and required precision	40
5.2	Light yield at the cube and attenuation in the fiber	40
5.2.1	Horizontal fibers	41
5.2.2	Vertical fibers	43
5.3	Reflection at the fiber edge	49
5.3.1	Expected value	49
5.3.2	Measurement of the reflection	49
5.3.3	Degeneration	51
5.3.4	Treatment of the reflection	53
5.4	Uncertainty of light yield calibration	54
6	Additional Effects on Light Yield	55
6.1	Motivation	55
6.2	Optical crosstalk	55
6.2.1	Beam test results	55
6.2.2	Monte Carlo simulation and possibility of calibration using cosmic muons	57
6.3	Quenching effect	60
6.3.1	Empirical formula	60
6.3.2	Estimation of the effect	60
6.3.3	Future prospects	60

7	Timing Calibration	61
7.1	Required precision	61
7.1.1	Summary of required precision	62
7.1.2	Source of time resolution	62
7.2	Time offset calibration	63
7.2.1	Basic methods	63
7.2.2	Capability of time offset calibration	64
7.3	Time-walk correction	68
7.3.1	Fiber time-walk	68
7.3.2	MPPC-Electronics time-walk	68
7.3.3	Methods for time-walk correction	68
7.3.4	Capability of time-walk correction and time synchronization	70
7.4	Expected precision of timing calibration	73
8	Measurement of new wavelength-shifting fiber products with short decay time	74
8.1	Experimental setup	74
8.1.1	Dark box and jigs	75
8.1.2	Laser	76
8.1.3	MPPC and circuit	76
8.1.4	Digitizer	77
8.1.5	Wavelength-shifting fiber	77
8.1.6	Light-shielding films	77
8.2	Analysis method	78
8.2.1	Waveform and timing determination	78
8.2.2	Event selection	78
8.2.3	Fitting function	79
8.2.4	Single photon time resolution	79
8.3	Results and discussions	80
8.4	Possible improvement of neutron measurement	83
9	Summary and Conclusion	85

Chapter 1

Neutrino Oscillation and Interaction

1.1 Neutrino oscillation

This thesis is about a new detector for the T2K experiment to study neutrino oscillation. In this chapter, we introduce the physics of neutrino oscillation and neutrino interaction briefly.

1.1.1 Neutrino mixing

Neutrino has flavor and mass eigenstates. The relationship between flavor eigenstates $|\nu_\alpha\rangle$ ($\alpha = e, \mu, \tau$) and mass eigenstates $|\nu_i\rangle$ ($i = 1, 2, 3$) is

$$|\nu_\alpha\rangle = \sum_i U_{\alpha i} |\nu_i\rangle, \quad (1.1)$$

where U is a unitary mixing matrix called Pontecorvo-Maki-Nakagawa-Sakata (PMNS) matrix.

The number of total degrees of freedom and rotation angles of the n -dimensional unitary matrix are n^2 and $n(n-1)/2$, respectively. If neutrinos are Dirac particles, $2n-1$ parameters are unphysical because they can be removed by phase transformation. Remained $(n-1)(n-2)/2$ parameters give rise to CP violations. The number of CP -violating phases is one if $n=3$. If neutrinos are Majorana particles, the number of CP -violating phases is $n(n-1)/2$.

The PMNS matrix can be written with three mixing angles $\theta_{12}, \theta_{13}, \theta_{23}$ and one CP -violating phase δ_{CP} :

$$U = \begin{pmatrix} U_{e1} & U_{e2} & U_{e3} \\ U_{\mu1} & U_{\mu2} & U_{\mu3} \\ U_{\tau1} & U_{\tau2} & U_{\tau3} \end{pmatrix} \quad (1.2)$$

$$= \begin{pmatrix} 1 & 0 & 0 \\ 0 & c_{23} & s_{23} \\ 0 & -s_{23} & c_{23} \end{pmatrix} \begin{pmatrix} c_{13} & 0 & s_{13}e^{-i\delta_{CP}} \\ 0 & 1 & 0 \\ -s_{13}e^{i\delta_{CP}} & 0 & c_{13} \end{pmatrix} \begin{pmatrix} c_{12} & s_{12} & 0 \\ -s_{12} & c_{12} & 0 \\ 0 & 0 & 1 \end{pmatrix} \quad (1.3)$$

$$= \begin{pmatrix} c_{12}c_{13} & s_{12}c_{13} & s_{13}e^{-i\delta_{CP}} \\ -s_{12}c_{23} - c_{12}s_{13}s_{23}e^{i\delta_{CP}} & c_{12}c_{23} - s_{12}s_{13}s_{23}e^{i\delta_{CP}} & c_{13}s_{23} \\ s_{12}s_{23} - c_{12}s_{13}c_{23}e^{i\delta_{CP}} & c_{12}s_{23} - s_{12}s_{13}c_{23}e^{i\delta_{CP}} & c_{13}c_{23} \end{pmatrix}, \quad (1.4)$$

where $c_{ij} = \cos \theta_{ij}$ and $s_{ij} = \sin \theta_{ij}$.

1.1.2 Neutrino oscillation in vacuum

A free particle in a mass eigenstate propagates like

$$|\nu_i(t)\rangle = \exp(-i(E_i t - p_i L)) |\nu_i(0)\rangle, \quad (1.5)$$

where t, L are flight time and length, and E_i, p_i are neutrino energy and momentum. By taking the ultrarelativistic limit

$$E_i = \sqrt{p_i^2 + m_i^2} \simeq p_i + \frac{m_i^2}{2p_i} \simeq p_i + \frac{m_i^2}{2E}, \quad t \simeq L, \quad (1.6)$$

the propagation is written as

$$|\nu_i(t)\rangle \simeq \exp\left(-i\frac{m_i^2 L}{2E}\right) |\nu_i(0)\rangle. \quad (1.7)$$

The time evolution of a flavor eigenstate $|\nu_\alpha\rangle$ is

$$|\nu_\alpha(t)\rangle = \sum_i U_{\alpha i} \exp\left(-i\frac{m_i^2 L}{2E}\right) |\nu_i(0)\rangle \quad (1.8)$$

$$= \sum_{i,\beta} U_{\alpha i} U_{\beta i}^* \exp\left(-i\frac{m_i^2 L}{2E}\right) |\nu_\beta\rangle, \quad (1.9)$$

where $|\nu_\alpha(t)\rangle$ is a neutrino created with a certain flavor α at time $t = 0$. The neutrino oscillation probability from ν_α to ν_β is

$$P(\nu_\alpha \rightarrow \nu_\beta) = |\langle \nu_\beta | \nu_\alpha(t) \rangle|^2 \quad (1.10)$$

$$\begin{aligned} &= \delta_{\alpha\beta} - 4 \sum_{i<j} \text{Re}(U_{\alpha i} U_{\beta i}^* U_{\alpha j}^* U_{\beta j}) \sin^2\left(\frac{\Delta m_{ij}^2 L}{4E}\right) \\ &\quad + 2 \sum_{i<j} \text{Im}(U_{\alpha i} U_{\beta i}^* U_{\alpha j}^* U_{\beta j}) \sin\left(\frac{\Delta m_{ij}^2 L}{2E}\right), \end{aligned} \quad (1.11)$$

where $\Delta m_{ij}^2 = m_i^2 - m_j^2$ is the difference of the mass squared. The oscillation probability of antineutrino from $\bar{\nu}_\alpha$ to $\bar{\nu}_\beta$ is

$$P(\bar{\nu}_\alpha \rightarrow \bar{\nu}_\beta) = |\langle \bar{\nu}_\beta | \bar{\nu}_\alpha(t) \rangle|^2 \quad (1.12)$$

$$\begin{aligned} &= \delta_{\alpha\beta} - 4 \sum_{i<j} \text{Re}(U_{\alpha i} U_{\beta i}^* U_{\alpha j}^* U_{\beta j}) \sin^2\left(\frac{\Delta m_{ij}^2 L}{4E}\right) \\ &\quad - 2 \sum_{i<j} \text{Im}(U_{\alpha i} U_{\beta i}^* U_{\alpha j}^* U_{\beta j}) \sin\left(\frac{\Delta m_{ij}^2 L}{2E}\right). \end{aligned} \quad (1.13)$$

1.1.3 CP violation

The difference in the oscillation probabilities between neutrino and antineutrino is

$$\Delta P_{\alpha \rightarrow \beta} = P(\nu_\alpha \rightarrow \nu_\beta) - P(\bar{\nu}_\alpha \rightarrow \bar{\nu}_\beta) \quad (1.14)$$

$$= 4 \sum_{i<j} \text{Im}(U_{\alpha i} U_{\beta i}^* U_{\alpha j}^* U_{\beta j}) \sin\left(\frac{\Delta m_{ij}^2 L}{2E}\right). \quad (1.15)$$

If α and β are identical, $\Delta P_{\alpha\beta}$ is 0, which means no difference in the survival probabilities between neutrino and antineutrino.

Let us consider $\nu_\mu \rightarrow \nu_e$ and $\bar{\nu}_\mu \rightarrow \bar{\nu}_e$ oscillations. The difference in the oscillation probabilities between the two is

$$\Delta P_{\mu \rightarrow e} = P(\nu_\mu \rightarrow \nu_e) - P(\bar{\nu}_\mu \rightarrow \bar{\nu}_e) \quad (1.16)$$

$$= -16s_{12}c_{12}s_{23}c_{23}s_{13}c_{13}^2 \sin \delta_{CP} \sin \left(\frac{\Delta m_{32}^2 L}{4E} \right) \sin \left(\frac{\Delta m_{21}^2 L}{4E} \right) \sin \left(\frac{\Delta m_{31}^2 L}{4E} \right) \quad (1.17)$$

$$= -2 \cos \theta_{13} \sin(2\theta_{12}) \sin(2\theta_{23}) \sin(2\theta_{13}) \sin \delta_{CP} \\ \times \sin \left(\frac{\Delta m_{32}^2 L}{4E} \right) \sin \left(\frac{\Delta m_{21}^2 L}{4E} \right) \sin \left(\frac{\Delta m_{31}^2 L}{4E} \right). \quad (1.18)$$

Conditions for CP violation in neutrino oscillations are

$$\theta_{ij} \neq 0 \quad (1.19)$$

$$m_i \neq m_j \quad (1.20)$$

$$\delta_{CP} \neq 0, \pi. \quad (1.21)$$

1.2 Neutrino interaction

In this section, neutrino-nucleon interactions are described. Modern neutrino experiments are performed with nuclear targets. In the energy range up to a few GeV, the main interaction modes are charged-current quasi-elastic scattering (CCQE), charged-current resonance scattering (CC RES), and charged-current deep inelastic scattering (CC DIS). Figure 1.1 shows the cross-section of neutrino-nucleus interactions.

1.2.1 Charged-current quasi-elastic scattering (CCQE)

Charged-current quasi-elastic interaction

$$\nu_l + n \rightarrow l^- + p \quad (1.22)$$

$$\bar{\nu}_l + p \rightarrow l^+ + n \quad (1.23)$$

is the two-body process between a neutrino and a nucleus. This is the dominant interaction mode at the sub-GeV neutrino energy range. Figure 1.2 shows the diagram of CCQE. Assuming a nucleon at rest, the initial neutrino energy E_ν can be reconstructed only with the lepton kinematics as:

$$E_\nu = \frac{2m_n E_l - m_l^2 + (m_p^2 - m_n^2)}{2(m_n - E_l + p_l \cos \theta)}, \quad (1.24)$$

where E_l , p_l , and m_l are the energy, momentum, and mass of the final state lepton, respectively. m_n and m_p are the mass of neutrons and protons. θ is the scattering angle of the lepton with respect to the direction of the initial neutrino.

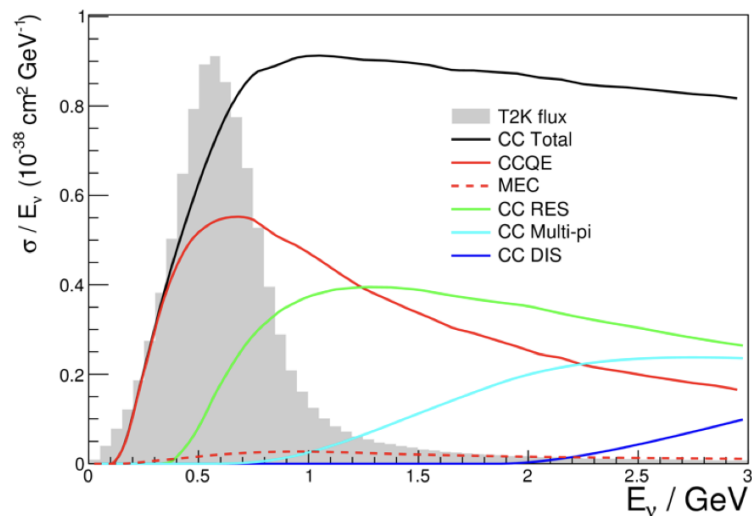


Figure 1.1. Cross-section of neutrino-nucleus interactions for neutrino mode [1]. The shape of the expected neutrino beam flux in T2K is shown with the shaded area.

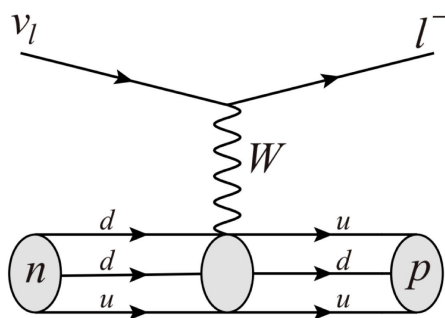


Figure 1.2. A diagram of CCQE [1].

1.2.2 Charged-current resonance scattering (CC RES)

For the neutrino energy around a few GeV, the most dominant interaction process is resonance scattering. A nucleon struck by a neutrino is able to become a baryon resonant state. It decays into a final state with a nucleon and a single pion, kaon, eta, or gamma. Figure 1.3 shows an example of the case of decaying into a pion. The resonant pion production process can be written as:

$$\nu_l + N \rightarrow N^* + l^- \rightarrow N' + l^- + \pi, \quad (1.25)$$

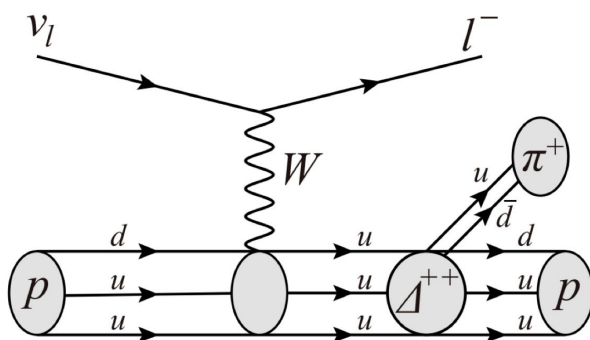


Figure 1.3. A diagram of CC RES pion production [1].

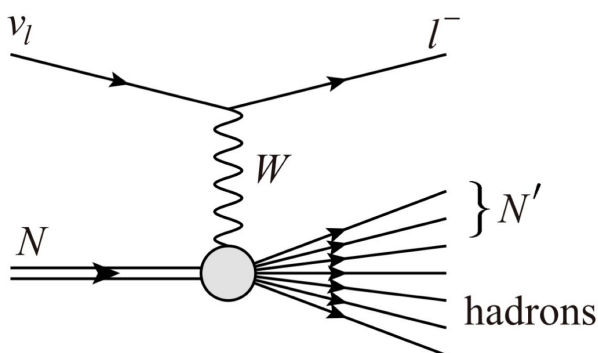


Figure 1.4. A diagram of CC DIS [1].

where $N, N' = n, p$ and N^* is the resonant state. The possible resonant single-pion production via ν_μ or $\bar{\nu}_\mu$ charged-current are

$$\nu_\mu p \rightarrow \mu^- p \pi^+ \quad (1.26)$$

$$\nu_\mu n \rightarrow \mu^- p \pi^0 \quad (1.27)$$

$$\nu_\mu n \rightarrow \mu^- n \pi^+ \quad (1.28)$$

$$\bar{\nu}_\mu p \rightarrow \mu^+ p \pi^- \quad (1.29)$$

$$\bar{\nu}_\mu p \rightarrow \mu^+ n \pi^0 \quad (1.30)$$

$$\bar{\nu}_\mu n \rightarrow \mu^+ n \pi^- \quad (1.31)$$

1.2.3 Charged-current deep inelastic scattering (CC DIS)

At the higher energy region around 10 GeV, the deep inelastic scattering process dominantly contributes. Neutrinos are able to directly interact with quarks inside a nucleon via weak bosons. It typically breaks the nucleon and produces a jet of hadrons as shown in Fig. 1.4.

DIS becomes dominant around 10 GeV. It has a small contribution in a few GeV regions. There is an interaction with a small invariant mass of the hadronic system in the final state. For example, there is a process of a few pions in the final state hadrons known as the “multi-pion” process.

1.2.4 Nuclear effect

In the descriptions above, we have assumed free nucleons. This assumption is not reliable in the case of nucleus targets such as carbon or oxygen targets. We need to think of three effects due to the nucleus target: the initial state effect, the correlation in the nuclear medium, and the final state interactions.

The initial state motion of nucleons inside the nucleus can affect the neutrino interactions. This is called the initial state effect. In order to describe the initial state effect, some models are proposed such as the global relativistic Fermi gas model (RFG) [2], the local Fermi gas model (LFG) [3], and the spectral function model (SF) [4].

Because the target nucleon is not free, neutrino-nucleus interactions should be corrected to include scattering off a bound state of multiple nucleons inside the nucleus. Nieves [5] and Martini [6] proposed the models describing multi-nucleon interactions. Those models consider n particles n holes excitation (n_pn_h). In this expression, the CCQE interaction is 1p1h. Neutrino interactions with multiple nucleons are also considered, such as 2p2h interactions. The meson exchange current (MEC) is the dominant process for the 2p2h interaction.

The final state particles such as proton or pion produced at the neutrino interactions can re-interact inside the nuclear medium. Those interactions are called the final state interactions. Those particles can be absorbed and get their kinematics distorted or eject additional hadrons.

Chapter 2

T2K Experiment

2.1 Overview

The T2K (Tokai to Kamioka) experiment is a long baseline neutrino oscillation experiment in Japan [7]. T2K began accumulating neutrino beam data for physics analysis in January 2010. ν_μ and $\bar{\nu}_\mu$ beams are generated at Japan Proton Accelerator Research Complex (J-PARC). Neutrinos are detected at the near detector 280 m away from the production target and at the far detector (Super-Kamiokande) 295 km away from the target as shown in Fig. 2.1.

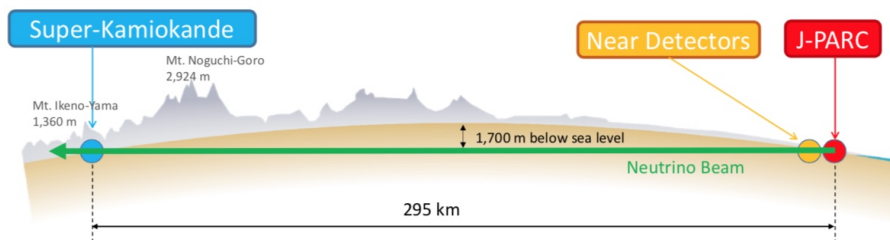


Figure 2.1. Overview of the T2K experiment.

2.2 J-PARC accelerator and T2K neutrino beamline

2.2.1 J-PARC accelerator

J-PARC consists of three accelerators: a 400 MeV linear accelerator (LINAC), a 3 GeV rapid cycling synchrotron (RCS), and a 30 GeV main ring (MR) synchrotron. A H^- beam is accelerated up to 400 MeV by the LINAC and is converted to a proton beam by charge-stripping foils at the RCS injection. The beam is accelerated up to 3 GeV by the RCS then injected into MR and accelerated up to 30 GeV.

Each proton beam spill consists of eight proton bunches. Each bunch typically has a timing spread of 15 ns and is separated by 580 ns.

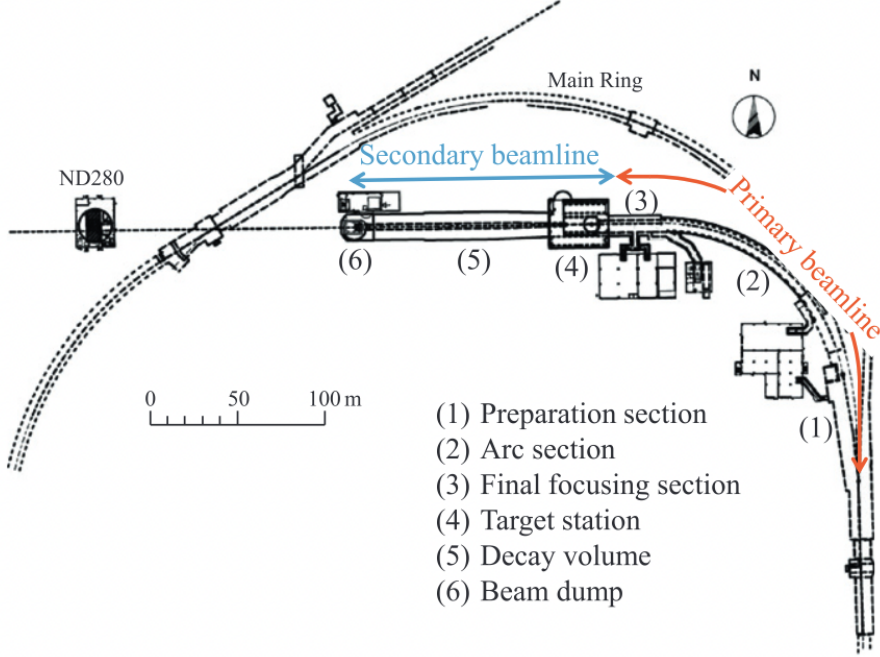


Figure 2.2. Overview of the T2K neutrino beamline [7].

2.2.2 Neutrino beamline

The neutrino beamline is composed of two sequential sections: the primary and secondary beamlines as shown in Fig. 2.2.

In the primary beamline, the extracted proton beam is transported to point toward Kamioka. It consists of the preparation, arc, and final focusing sections.

The secondary beamline contains a target station, a decay volume, and a beam dump as shown in Fig. 2.3. In the target station, a graphite target with a length of 91.4 cm and a diameter of 2.6 cm is located. The 30 GeV proton beam strikes this graphite target to emit pions with other hadrons. There are three magnetic horns to collect and focus the charged pions. The horn polarity is controlled to alter the beam modes. The polarity for the neutrino beam mode is defined as a forward horn current (FHC) and that for the anti-neutrino beam mode is defined as a reversed horn current (RHC).

The focused charged pions enter the decay volume. It is an about 96 m long steel tunnel. As transferred through the decay volume, pions decay into muons and muon neutrinos. The dominant decay modes are

$$\pi^+ \rightarrow \mu^+ + \nu_\mu \quad (2.1)$$

$$\pi^- \rightarrow \mu^- + \bar{\nu}_\mu. \quad (2.2)$$

The beam dump is located 109 m downstream from the target in order to stop all the particles from the beamline except for neutrinos and high-energy muons. The high-energy muons can penetrate the beam dump and are measured by a muon monitor (MUMON) [8]. MUMON is composed of two independent detectors: ionization chambers and silicon PIN photodiodes. MUMON can measure the two-dimensional profile of the muons and check the neutrino beam direction and intensity.

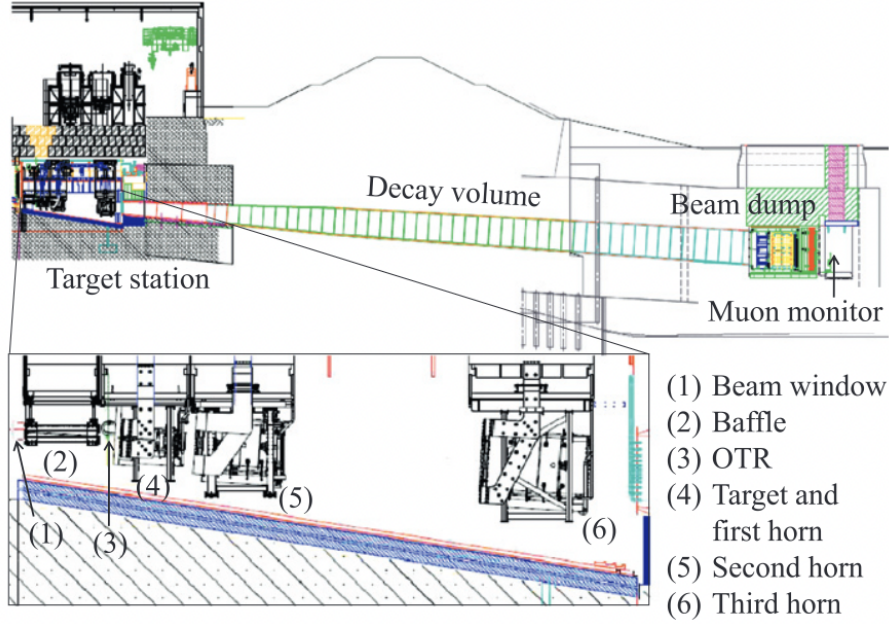


Figure 2.3. Side view of the secondary beamline [7].

2.2.3 Off-axis method

In the case of a two-body decay of a pion, the neutrino energy E_ν is calculated as:

$$E_\nu = \frac{m_\pi^2 - m_\mu^2}{2(E_\pi - p_\pi \cos \theta_\nu)}, \quad (2.3)$$

where m_π and m_μ are the masses of a pion and muon, p_π is the momentum of a pion, and θ_ν is the angle between the initial pion and the neutrino. The energy of neutrino is related to the angle. T2K adopts the off-axis 2.5° to set the peak energy of the neutrino beam to be around 600 MeV, which maximizes the neutrino oscillation probabilities at 295 km and to generate the narrow-band neutrino beam [9]. Figure 2.4 shows the muon neutrino survival probability at 295 km and neutrino fluxes for different off-axis angles.

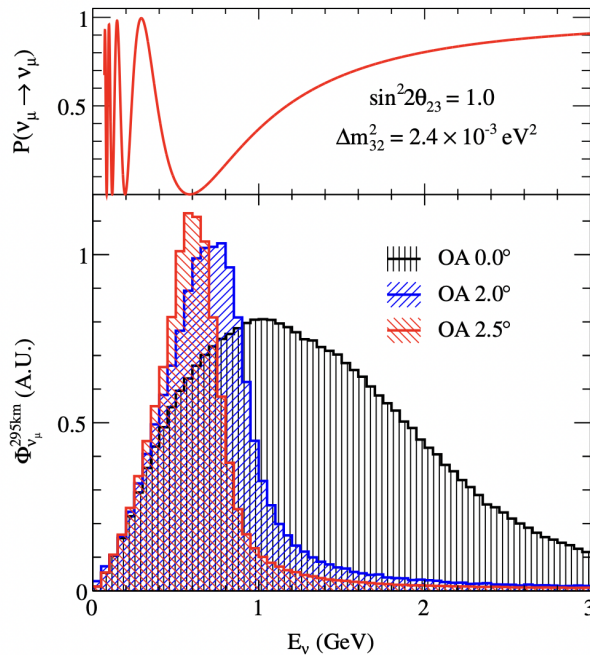


Figure 2.4. Muon neutrino survival probability at 295 km and neutrino fluxes for different off-axis angles [9].

2.3 Near detectors

2.3.1 ND280

In a long baseline experiment, the role of the near detector is to reduce the flux and cross-section uncertainties associated with neutrino production and interactions and allow a prediction of the expected spectra at the far detector. The ND280 is a complex of several sub-detectors. It is 280 m downstream from the neutrino beam target. The schematic view of the current ND280 is shown in Fig. 2.5. Two Fine Grained Detectors (FGDs) and three Time Projection Chambers (TPCs) are the main tracking detectors in ND280. FGDs are also the active target of neutrino interactions. In the analysis, we mainly use neutrino interaction in one of the FGDs whose final-state leptons enter one of the TPCs. The π^0 detector (P0D) is placed at the most upstream part of the detectors. It aims at measuring the neutral current interactions. FGDs, TPCs, and P0D are surrounded by electromagnetic calorimeters (ECals). Sub-detectors are contained inside the magnet recycled from the UA1 experiment at CERN. It also serves as a side muon range detector (SMRD) with plastic bars inserted at gaps between the magnet yokes.

FGD

Each FGD has plastic scintillator tracking planes, which also work as the main target of neutrino interactions [11]. The FGD module at the upstream (FGD1) is fully composed of the scintillators, while the downstream one (FGD2) contains water target parts sandwiched between the scintillator layers. FGDs consist of scintillator bars with the size of $184 \times 0.96 \times 0.96 \text{ cm}^3$ as shown in Fig. 2.6. FGD1 has 15 sub-modules and FGD2 has 7 sub-modules.

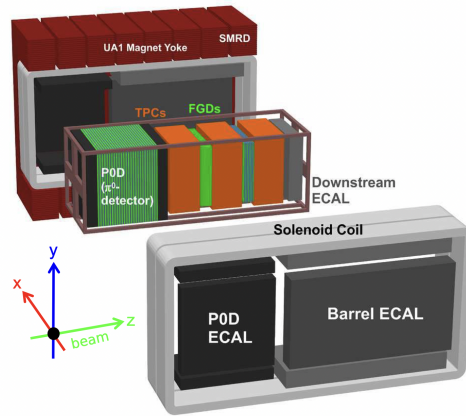


Figure 2.5. The current ND280 [10].

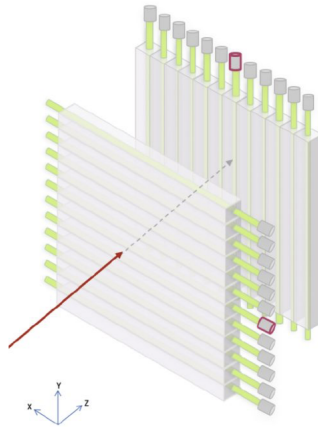


Figure 2.6. One sub-module structure of FGD [12].

2.3.2 INGRID

In order to monitor the neutrino beam intensity, the INGRID modules are placed on the neutrino beam axis. An INGRID module consists of an alternating layer structure of 9 iron target plates and 11 plastic tracking scintillator planes, surrounded by four veto scintillator planes.

2.4 Far detector (Super-Kamiokande)

T2K experiment uses Super-Kamiokande (SK) as the far detector placed 295 km away from the target. It is a 50 kton water Cherenkov detector with a cylindrical stainless-steel tank, with 39.3 m in diameter and 41.4 m in height. The detector is separated into optically isolated two volumes: the inner detector (ID) and the outer detector (OD). The inner wall of the water tank is covered by 11,200 20-inch photomultiplier tubes (PMTs) and the outer wall is covered by 1,185 8-inch PMTs for the purpose of veto.

2.5 Latest results on δ_{CP}

T2K published the latest results [13] based on the data collected up to the end of May 2018. This corresponds to an exposure of 1.494×10^{21} protons on target (POT) in FHC mode and 1.635×10^{21} POT in RHC mode.

Figure 2.7 shows the $\Delta\chi^2$ and obtained 3σ intervals of δ_{CP} for both mass orderings. In both mass orderings, the two CP -conserving values of 0 and π are outside the 2σ confidence intervals. We exclude the conservation of CP symmetry in neutrino oscillation at the 2σ level. For the inverted mass ordering, both CP -conserving values are outside of the 3σ confidence intervals. For the normal mass ordering, $\delta_{CP} = 0$ is outside the 3σ confidence interval, while $\delta_{CP} = \pi$ is inside.

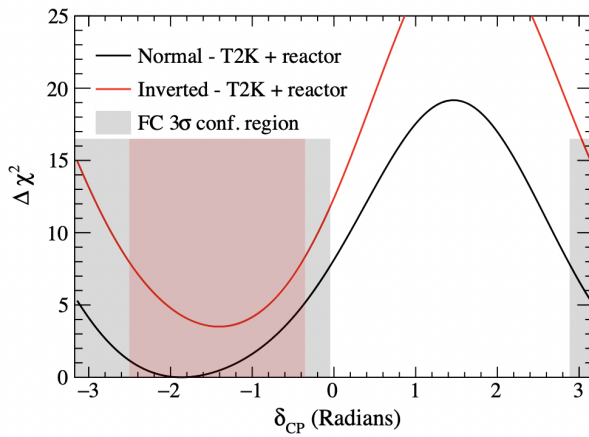


Figure 2.7. $\Delta\chi^2$ and obtained 3σ Feldman-Cousins (FC) confidence intervals [13].

2.6 Limitation of the current ND280

Though the current ND280 shows good performance, it has limitations. When we use large statistics for future precise measurements, systematic uncertainties will become dominant.

2.6.1 High angle scattered particles

The main limitation of the current ND280 is that most leptons are selected at the TPC downstream of the FGD in which the neutrino interaction occurred. The efficiency in the forward region is good but it decreases considerably for the higher scattered regions compared to the beam direction.

On the other hand, Super-Kamiokande has 4π acceptance and the efficiency is flat with respect to the beam direction. To extrapolate the expected spectra obtained at the near detector to the far detector, we need interaction models to describe the dependency on the kinematics such as momentum and angle. Figure 2.8 shows reconstructed charged lepton angle distributions at ND280 and SK.

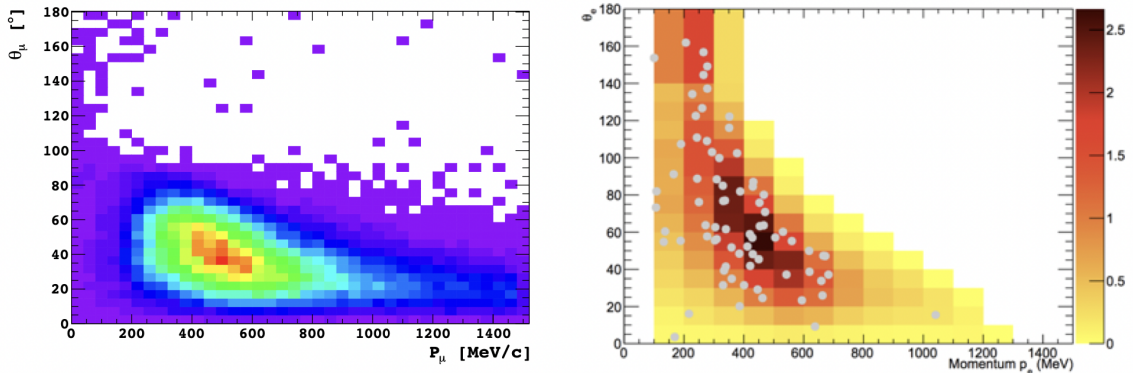


Figure 2.8. Reconstructed momentum and angle for muons selected at ND280 (left) and electrons selected at SK (right) [14].

2.6.2 Low momentum particles

We use FGDs as target detectors and they are composed of two orthogonal layers. To reconstruct a track, we need three points in each plane and this is about 6 cm for FGDs. In the case of the proton, this length corresponds to about 600 MeV/ c . We need to detect protons with momentum below 600 MeV/ c to understand the details of neutrino-nucleon interactions.

2.6.3 Electron neutrino interactions

Another limitation of the current near detector is its low efficiency in selecting electron neutrino interactions below 1 GeV. It is related to contaminations of gammas generating electromagnetic showers in the detector. The method used in T2K to constrain flux and cross-section systematic uncertainties relies on the selection of muon neutrinos at ND280 for both ν_μ and ν_e . We need the cross-section model to describe electron neutrino interactions. The model has 3% uncertainty and it is included in the oscillation analysis. ND280 has already measured ν_e interactions but it is able to constraint the ν_e/ν_μ cross-section difference at only 10% level.

2.7 T2K-II

The T2K oscillation parameter measurements are limited by statistics now. T2K needs to collect more data in both neutrino and antineutrino modes by continuous data-taking and upgrading the beamline. As the statistics increase, the effect of the systematic uncertainties will become more crucial to the δ_{CP} measurement. The present configuration of ND280 leads to systematic errors of the order of 6%. We need to bring this number down to 4% to achieve the observation of CP violation at the 3σ level. Also, SK is upgraded by dissolving the gadolinium to detect the neutron with a higher efficiency.

year	power (kW)	number of protons per spill	repetition time (s)
2021	515	2.66×10^{14}	2.48
2023	750	2.1×10^{14}	1.32
by 2027	1300	3.3×10^{14}	1.16

Table 2.1. Accelerator upgrade summary.

2.7.1 Beam Upgrade

The J-PARC Main Ring accelerated protons every 2.48 s with a power of 515 kW until the last T2K physics run. The accelerator upgrade aims to improve the beam power towards 750 kW in 2023 and 1.3 MW until the start of the Hyper-Kamiokande experiment. The repetition time will be 1.32 s in 2023 and 1.16 s in the future. The beam power, the number of protons per pulse, and the repetition time are summarized in Table 2.1.

The neutrino beamline is also upgraded. The power supply of the horn is from 250 kA to 320 kA to focus more charged pions. Cooling systems for the horn and target are improved.

2.7.2 SK-Gd

For most of the operation time of SK, it is filled with ultrapure water. However, we added gadolinium (Gd) to the water. Some of the neutrons produced with the neutrino interaction such as the inversed beta decay

$$\bar{\nu}_e + p \rightarrow e^+ + n \quad (2.4)$$

are captured by Gd. Excited Gd nuclei emit photons when they de-excite. We use the presence of the neutron as event selection.

In 2020, we loaded Gd to 0.01%, and the capture efficiency was about 50%. In 2022, we loaded an additional Gd to 0.03%, and the neutron capture efficiency became 75%.

2.7.3 ND280 Upgrade

To reduce systematic uncertainties related to the limitation of the current near detectors, we are working on upgrading the near detector. Because the current ND280 has proven the combination of active targets and TPCs as a successful configuration, we keep the basic concept. The requirements for the upgraded near detector are as follows.

- Full polar angle acceptance with similar performance in terms of momentum resolution, energy loss, and charge measurement as the current ND280.
- Fiducial mass of at least a few tons (each of the two FDGs has a fiducial mass of about one ton).
- High-efficiency 4π tracking for low energy pions and protons stopping inside the active target detector in order to determine the event topology with proton-pion identification.
- Good timing resolution for tracking in order to determine the direction to reject particles from the outside the detectors.

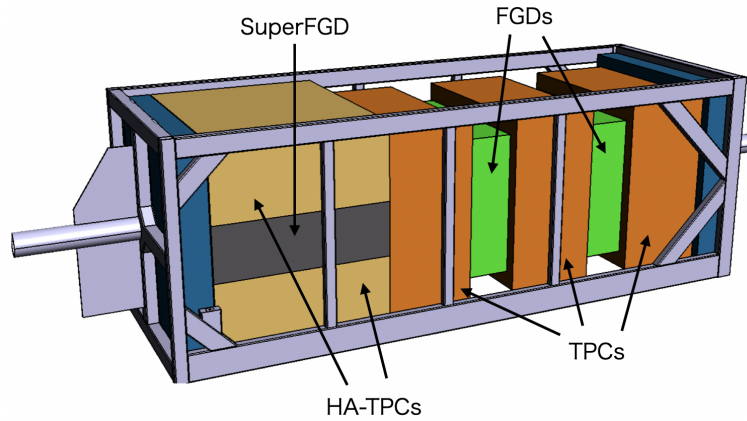


Figure 2.9. Schematic view of the upgraded ND280 [15].

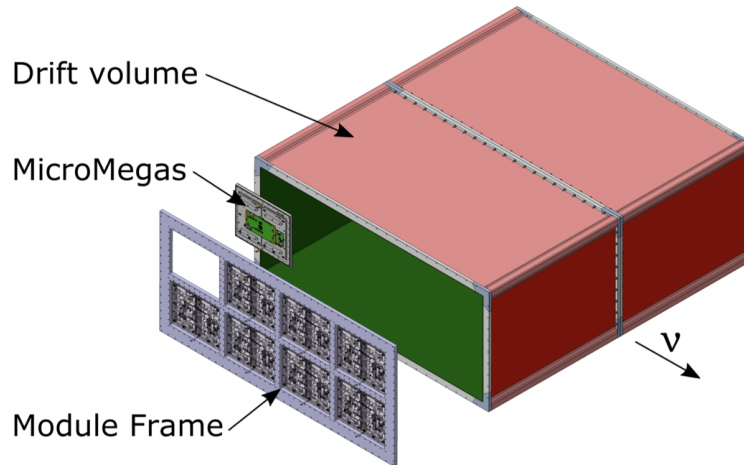


Figure 2.10. Schematic view of the HA-TPC [14].

In order to satisfy these requirements, we decide to replace the POD detector with new detectors as shown in Fig. 2.9. The active target detector is Super Fine Grained Detector (SuperFGD). It is sandwiched by two High Angle Time Projection Chambers (HA-TPCs). These detectors are surrounded by six Time of Flight (ToF) detectors.

SuperFGD

The main part of this thesis is about SuperFGD. We describe this detector in the next chapter.

HA-TPC

Two HA-TPCs are placed top and bottom sides of the SuperFGD. The schematic view of the HA-TPC is shown in Fig. 2.10. It consists of a gas-tight rectangular box subdivided by a common high-voltage cathode located in its midpoint and supporting the

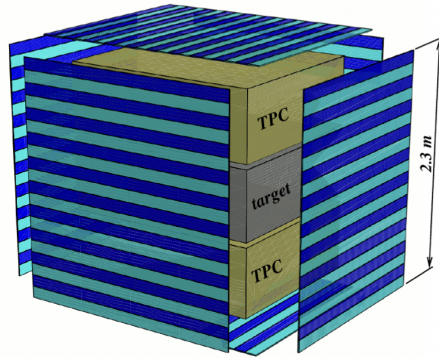


Figure 2.11. Schematic layout of the ToF detector planes [14].

eight Micromegas readout modules that are located in a plane parallel to the cathode at each end of the box.

They provide crucial information for the event reconstruction and analysis, such as

- Track reconstruction in 3D.
- Charge measurement.
- Momentum measurement.
- Particle identification by combining the energy deposit with momentum measurement.

ToF

Six ToF detectors surround the SuperFGD and HA-TPCs as shown in Fig. 2.11. The ToF system aims at precisely measuring the crossing time of the charged particle in ND280. Combined with a timing measurement in SuperFGD, we determine the direction of the particle to separate neutrino interactions in SuperFGD from backgrounds originating from outside the detectors. ToF planes consist of several plastic scintillator bars. The bar dimension is $200 \times 1 \times 12 \text{ cm}^3$ (along the beam) or $230 \times 1 \times 12 \text{ cm}^3$ (perpendicular to the beam) to cover SuperFGD and HA-TPCs. We decide to use EJ-200 as bars to achieve precise timing [16]. Figure 2.12 shows the time resolution of 2.3 m ToF bar as a function of the position. Large-area MPPCs are placed directly to the scintillator bars on both ends.

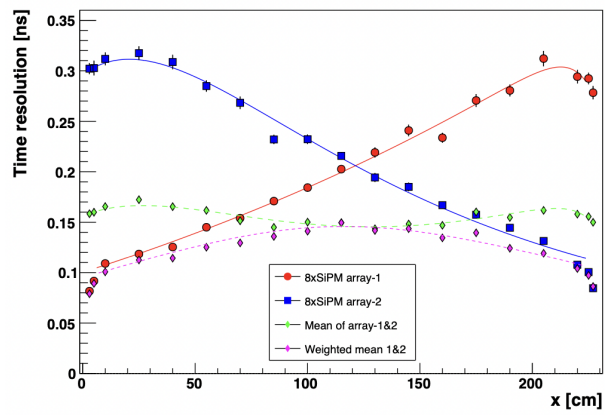


Figure 2.12. Measured time resolution with MPPC at both ends of a 2.3 m long bar as a function of the beam impact position along the bar [14].

Chapter 3

SuperFGD

3.1 Components

As written in the previous chapter, SuperFGD is a new scintillator target detector of the near detector. SuperFGD consists of $192 \times 56 \times 182 = 1,956,864$ plastic scintillator cubes. Each cube has three dimension holes to insert wavelength-shifting fibers. A schematic view of SuperFGD is shown in Fig. 3.1. The scintillation light produced in the scintillator cubes is transported in the wavelength-shifting fiber and detected at the multi-pixel photon counter (MPPC) attached to one side of the fiber.

3.1.1 Scintillator cubes

The scintillator cubes are produced by UNIPLAST Co. in Vladimir (Russia) using injection molding [17]. The scintillator composition is polystyrene doped with 1.5% paraterphenyl (PTP) and 0.01% POPOP as wavelength shifters. The decay time of each dye is about 1 ns and 2 ns, respectively. The cubes are covered by a reflecting layer by etching the surface of the scintillator with a chemical agent. As a result of etching, the surface of the cubes becomes white. The thickness of this reflecting layer is within 50 - 80 μm . Each cube has three orthogonal holes for wavelength-shifting fibers and its diameter is 1.5 mm.

3.1.2 Wavelength shifting fiber

Wavelength-shifting fibers are used to collect light from large areas of scintillators. We use Y-11 (200) produced by KURARAY CO., LTD [18]. It is a multi-cladding and round shape fiber and the same fiber as the current ND280. The diameter of the fiber is 1.0 mm. The cross-section and cladding thickness of Y-11 is shown in Fig. 3.2. The refractive indices of the core, middle clad, and outer clad are listed in Table 3.1.

part	refractive index	material
core	1.59	Polystyrene
middle clad	1.49	Polymethylmethacrylate (PMMA)
outer clad	1.42	Fluorinated polymer (FP)

Table 3.1. The refractive index of each part of wavelength-shifting fiber Y-11 and its material.

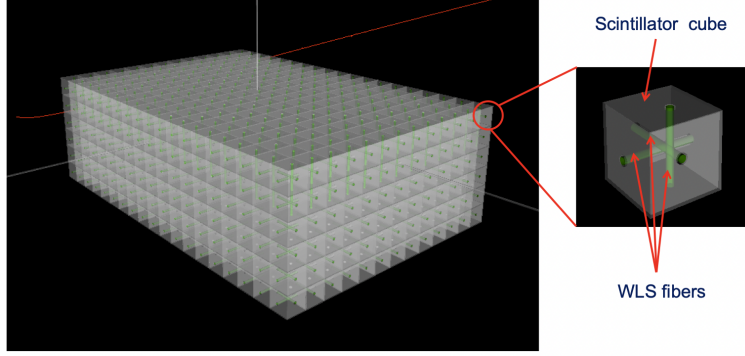


Figure 3.1. Schematic view of the SuperFGD. The number of cubes is reduced for ease of viewing. The size of each cube is $1 \times 1 \times 1 \text{ cm}^3$. The number of readout channels is 55,888 [14].

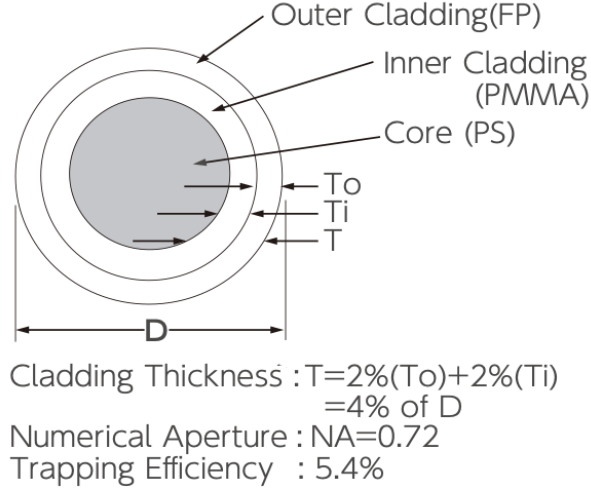


Figure 3.2. Cross-section and cladding thickness of wavelength-shifting fiber Y-11 [18].

The absorption and emission spectrum is shown in Fig. 3.3. The absorption peak of Y-11 is overlapped with the emission peak of POPOP. The attenuation length is longer than 3.5 m. This is longer than the length of the fiber used in SuperFGD.

3.1.3 Multi-pixel photon counter (MPPC)

We use MPPCs produced by Hamamatsu Photonics K.K. to detect the light from wavelength-shifting fibers. The MPPC type chosen for SuperFGD is S13360-1325PE [19]. Its sensitive area is $1.3 \text{ mm} \times 1.3 \text{ mm}$. The pixel pitch is $25 \mu\text{m}$ and this is smaller than that for the current ND280 in order to obtain a larger dynamic range. The number of pixels is 2,668. MPPCs for the SuperFGD are mounted on $8 \text{ cm} \times 8 \text{ cm}$ PCB boards in 8×8 arrays. This MPPC has advantages over that of the current ND280, such as a lower dark noise rate, crosstalk probability, and afterpulse probability.

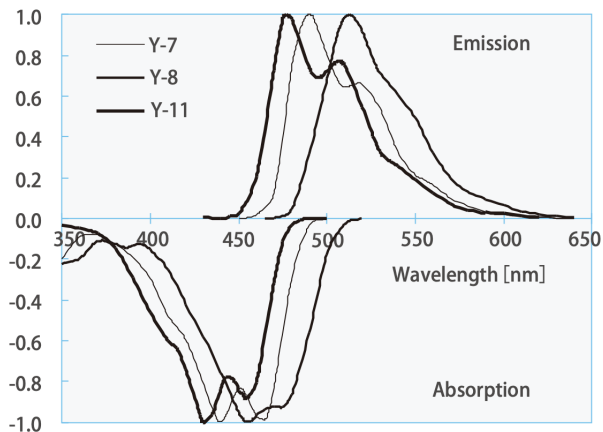


Figure 3.3. Absorption and emission spectra of Y series wavelength shifting fiber [18]. We use Y-11 for SuperFGD.

3.1.4 Electronics

We use Cherenkov Imaging Telescope Integrated Read Out Chip (CITIROC) as a readout chip. CITIROC is a frontend ASIC developed by Omega laboratory at Ecole Polytechnique [20]. As shown in Fig. 3.4, each signal input is processed by two main adjustable signal paths: a high gain (HG) path and a low gain (LG) path. Each of these two signal paths has a dedicated slow shaper. Timing information for each signal is provided by an independent fast shaper that can either be switched to the HG or LG path pre-amplifier output. A discriminator with adjustable thresholds follows the fast shaper. Both the rising and falling edges of these outputs are recorded. The time difference between rising and falling edges (Time-over-Threshold, ToT) gives some measure of signal amplitude. One CITIROC can read 32 channels of MPPC outputs.

Eight CITIROC chips are mounted on one front-end board (FEB). Fourteen FEBs are connected to one optical concentrator board (OCB). All sixteen OCBs are connected to the master clock board (MCB). OCBs are also connected to DAQ PC.

We have two modes for cosmic triggers. One is triggered by the coincidence found at the FEB level, called self-coincidence mode. The other is triggered by the MCB signal, called MCB coincidence mode. The MCB signal issues when the number of coincidences between the OCBs is within a certain range. Figure 3.5 shows the propagation of HITS_OUT signals for the coincidence at the MCB level.

3.1.5 LED calibration system

To measure the pedestal and high gain, the LED calibration system is attached to the opposite side from the MPPC [21]. Figure 3.6 shows the conceptual drawing of the light injection method for a large number of channels and a picture of the LGP prototype. The LED light propagates in the acrylic plate called Light Guide Plate (LGP) and is scattered at the notches arrayed at the same pitch as the fibers to inject light into the fiber.

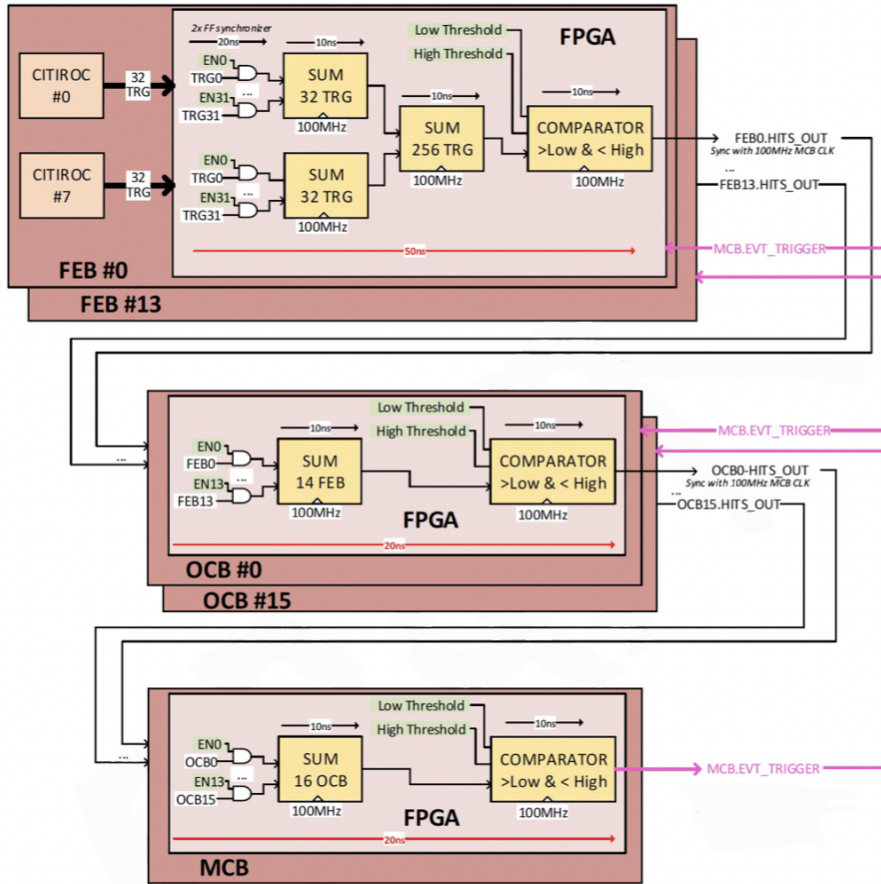


Figure 3.5. Cosmic trigger detection from FEB HITS_OUT signals to MCB EVT_TRIGGER signal.

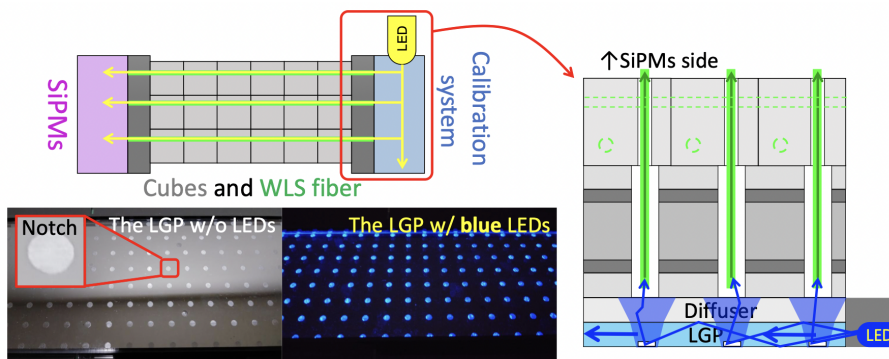


Figure 3.6. Conceptual drawing of the light injection method for a large number of channels and a picture of the LGP prototype [21].

3.2 Expected performance

3.2.1 High angle scattered particle

Because each cube of SuperFGD has 3-dimensional readouts and HA-TPCs exist above and below SuperFGD, angular acceptance is improved. Figure 3.7 shows the expected muon reconstruction efficiency as a function of the true muon polar angle.

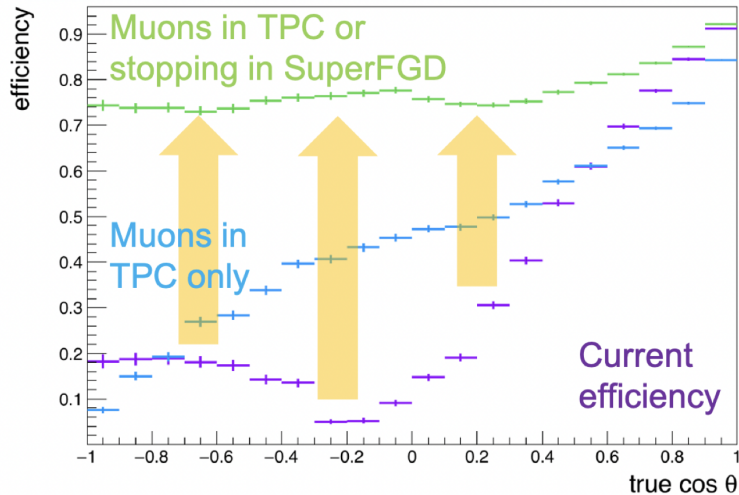


Figure 3.7. Muon reconstruction efficiency as a function of true muon polar angle [22].

3.2.2 Low momentum particle

Figure 3.8 shows the proton reconstruction efficiency in current ND280 and the momentum spectrum of protons generated in the neutrino interactions. We have events below $600 \text{ MeV}/c$ but the reconstruction efficiency is small.

Using SuperFGD, we can lower the detection threshold as shown in Fig. 3.9. We can detect protons down to $300 \text{ MeV}/c$ with SuperFGD.

3.2.3 Electron neutrino

Because SuperFGD has fine granularity, we can separate electrons and gamma rays by looking at the initial point of the shower. The shower begins with the only electron in the case of ν_e interactions while the shower begins with the electron-positron pair in the case of the gamma rays. Thanks to this fine granularity, we can reconstruct short positron tracks. Also by calculating the energy loss of the initial part of the electron track, we can get twice the larger energy deposit in the overlapped region of the electron-positron pair.

For tracks fully contained inside superFGD, we can achieve 50% efficiency for electron particle gun samples while keeping the misidentification rates for other particles less than 0.5% when we apply appropriate cuts described in [23].

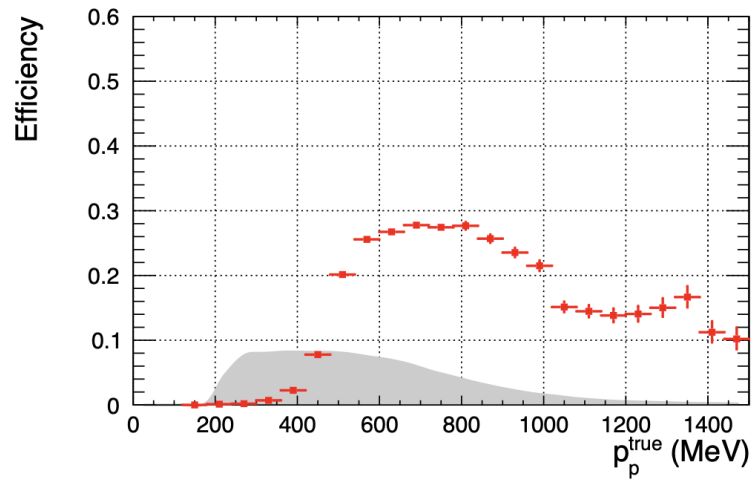


Figure 3.8. Proton reconstruction efficiency in current ND280 (red plots) and spectrum of generated protons according to NEUT MC (grey region) [14].

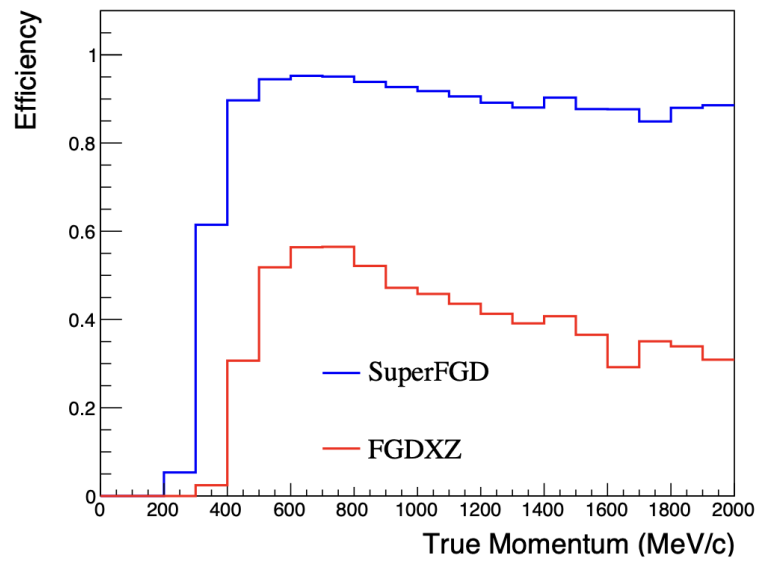


Figure 3.9. Proton reconstruction efficiency as a function of the true proton momentum. [15]

3.3 Calibration and necessary measurement

We describe the expected performances of SuperFGD above. To extract such performances, we need to know the parameters related to scintillator cubes, wavelength-shifting fibers, MPPCs, and electronics. For analysis, we use three kinds of information: light yield, timing, and position. It is important to know these properties precisely.

3.3.1 Pedestal and gain calibration

We have three kinds of information related to the signal amplitude: High-Gain ADC (HG), Low-Gain ADC (LG), and Time over Threshold (ToT). We need to obtain conversion factors from them to the number of observed photons (p.e.) at the MPPC.

3.3.2 Fiber calibration

The number of photons reaching the MPPC is affected by the property of wavelength-shifting fiber. We have to take into account two effects: attenuation and reflection. As photons propagate in the wavelength-shifting fiber, the light intensity decreases. We need to measure the attenuation fiber by fiber after the installation of the detector.

At the other edge of the fiber from MPPC, some photons are reflected. The ratio of reflected light and transmitted light depends on the treatment of the fiber edge. In the SuperFGD, to determine the treatment of fiber edge, measurements were performed and we decided just to cut and no treatment [24]. Even if we do not treat anything at the edge of the fiber, Fresnel reflection occurs. We need to know the level of the reflection.

3.3.3 Scintillator cube properties

The number of photons flowing into the wavelength-shifting fiber from the scintillator cube is affected by the property of the scintillator cubes even if the same energy is deposited in the cube. We have to take into account three effects: overall light yield, optical crosstalk, and scintillator quenching effect. We need to know the conversion factor from deposited energy (MeV) to the number of photons (p.e.). Actually, we cannot separate effects such as generated number of photons in the scintillator cube, the trapping efficiency of the wavelength-shifting fiber, and the photon detection efficiency (PDE) at the MPPC.

Each cube has a coating on the surface to reflect photons within the cube as we described above, but some fractions of photons flow into adjacent cubes. We call this phenomenon optical crosstalks. Figure 3.10 shows an image of crosstalks. If we underestimate the crosstalk rate, we may misreconstruct the track. We have to know the level of the optical crosstalk.

Scintillation light yield does not respond linearly. If dE/dX is large, the density of ionized molecules surrounding the particle is high and the proportionality of the energy loss (dE/dX) and light yield (dL/dX) becomes worse. This quenching effect is important when we analyze the particle that loses a large amount of energy in the cube such as the stopping point of the proton.

3.3.4 Timing calibration

Timing information is also used for the physics analysis. We have to take into account two items for time calibration, one is the time offset calibration and the other is the time-walk

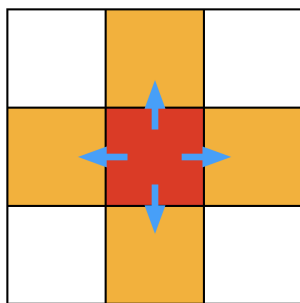


Figure 3.10. 2D image of crosstalks.

effects. We need to correct the time offset of all channels in SuperFGD and with other sub-detectors. If the time of the channels is different too much, we cannot take data or we cannot reconstruct the track.

There are two sources of the time-walk effect. The first one comes from the decay time of the scintillator and fiber. Because of the decay time, the detection timing can be late if the observed number of photons is small. The other comes from the threshold of electronics. The timing of passing the threshold depends on the pulse height.

3.3.5 Position alignment

We need to check the relative positions and rotations of SuperFGD to reconstruct particle tracks with other sub-detectors. We check the relative positions and rotations with TPC1 and HA-TPCs because they are neighborhood sub-detectors. In addition to the relative positions and rotations, we need to check the sag of the SuperFGD. Because of the weight of the SuperFGD, it can bend. According to the simulation study, it is about 2 mm. We need to check this effect using cosmic and beam data.

3.4 Plan of the construction and installation

In this section, we describe the status and schedule of SuperFGD as of January 2023. A summary of the construction and installation is shown in Fig. 3.11.

3.4.1 Construction

Box and cube

Assembly and integration work of SuperFGD at J-PARC started in August 2022. The scintillator cubes and the mechanical box were delivered from Russia and CERN, respectively. Cubes were put into the box in October and November 2022. At this stage, for mechanical integration, fishing lines are inserted in holes instead of WLS fibers. We closed the box at the end of 2022.

Fiber, MPPC, and LED calibration system

After that, we remove fishing lines from the cubes and insert wavelength-shifting fibers. MPPC-PCBs are attached in parallel. In this period, fibers are checked once using a

Date	Contents
Aug. 2022	Preparation started
Oct. 2022	Box + cube assembly
Dec. 2022	Box closure
Jan. 2023	Fiber insertion, MPPC attachment
Feb. 2023	LED calibration system attachment
Mar. 2023	Light barrier, cable installation
Apr. 2023	Electronics attachment
Spring 2023	Commissioning on the ground
Summer 2023	Installation into the pit, commissioning in the pit
Oct. 2023	Operation starts

Figure 3.11. Brief summary of the construction and installation.

dedicated system because fibers can be damaged while the insertion work. LED calibration systems and light barriers are also attached soon after the insertion work.

Cabling and electronics

Then, cabling work and integration with electronics are performed. Evaluation tests are performed in each step of the assembly and integration works. Fiber QC, light tightness check, and crate test are scheduled.

3.4.2 Commissioning and installation into the ND280 pit

Commissioning on the ground

After the assembly and integration work, we will check all the systems on the ground, because once the detector is installed in the ND280 pit, it is difficult to replace the components even if issues are found. In this commissioning, all the triggers which are the beam trigger, cosmic trigger, and LED calibration trigger will be checked. We will take the data with every trigger mode and check everything is fine. We can take cosmic or LED calibration data during this period, we have no magnet though.

Cables from MPPC may be swapped due to misconnection. By taking LED calibration and cosmic data, we need to check whether the positions of MPPCs are correct. If channels are swapped, we need to fix them.

In this commissioning period, we will decide on the gain settings. If the gain is too low, several p.e. peaks are overlapped and we cannot calibrate the pedestal and gain properly. On the other hand, if the gain is too high, the output saturates with a relatively small light yield. In this period, we tune the cosmic trigger scheme.

Installation, commissioning in the pit, and data taking

Then, SuperFGD will be installed into the ND280 pit. Currently, it is planned for the summer of 2023. Because components can get damaged during the installation of SuperFGD

into the pit, we need to check the components again. We plan to take data as a detector commissioning in the pit. We also plan to take cosmic data for calibration in this period. We consider using data taken in this period for the calibration method described in this thesis. We plan to take data before every physics run to check the stability.

SuperFGD is expected to start its operation in October 2023. After starting the physics run, we plan to flash the LED calibration system during every beam spill to check the pedestal and gain constantly. We also plan to take cosmic data during the physics run. We can also use muons derived from the neutrino beam for calibration. Because the ND280 pit is surrounded by a sand rock wall, we call these muons “sand muons”. In addition to the run time, we plan to take data for calibration on weekly accelerator maintenance days.

3.5 Subject of this thesis

3.5.1 Calibration and measurement for SuperFGD

In this thesis, the methods to measure the property of wavelength-shifting fibers, scintillator cubes, and timing information are introduced. To develop the calibration methods, we need simulation data. How to simulate the cosmic events is described in Chap. 4. We develop methods for fiber calibration using cosmic data. We also perform external measurements for the reflection at the edge of the fiber, described in Chap. 5. The overall photon yield of the scintillator is also described in Chap. 5. We also develop methods for the measurement of the scintillator cube properties: optical crosstalk and quenching effect, described in Chap. 6 as additional effects on the light yield. As for timing calibration, we develop calibration methods using cosmic muons, described in Chap. 7.

3.5.2 Measurement of new types of wavelength-shifting fiber

In addition to the development of calibration methods, we measure new types of wavelength-shifting fibers. The feature of these fibers is a short decay time. We describe the measurement in Chap. 8.

Chapter 4

Simulation of Cosmic Ray Events

To develop the calibration method, cosmic ray events are simulated using the Monte Carlo simulation. In this chapter, we describe how to simulate cosmic events.

4.1 Geant4 simulation

We simulate the upgraded ND280 using the Geant4 package [25]. Figure 4.1 shows the simulated detector geometry. All subdetectors except for ToF are implemented in the magnet. A magnetic field of 0.2 T is applied.

As for the SuperFGD, we have $192 \times 56 \times 184$ cubes and each cube is composed of $10.07 \text{ mm} \times 10.07 \text{ mm} \times 10.07 \text{ mm}$ scintillator with three holes whose diameters are 1.5 mm, and 0.1 mm coating outside the cubes as shown in Fig. 4.2. Inside the holes, wavelength-shifting fibers with 1.0 mm diameter are placed.

The energy and angle of cosmic rays are simulated based on the measured distributions. The intensity at the surface of the earth as a function of the momentum p and the cosine of zenith angle θ , $I(p, \cos \theta)$, is parametrized as described in [26]. The vertical component of the intensity I_V can be written as the function of the vertical component of the momentum $\zeta = p \cos \theta$:

$$I(p, \cos \theta) = \cos^3 \theta \times I_V(\zeta) \quad (4.1)$$

$$I_V(\zeta) = c_1 \times \zeta^{-1(c_2+c_3 \log_{10}(\zeta)+c_4(\log_{10}(\zeta))^2+c_5(\log_{10}(\zeta))^3)}. \quad (4.2)$$

Here, c_1 to c_5 are free parameters. We use the values obtained from a fit to data in [26]:

$$c_1 = 0.00253 \quad (4.3)$$

$$c_2 = 0.2455 \quad (4.4)$$

$$c_3 = 1.288 \quad (4.5)$$

$$c_4 = -0.2555 \quad (4.6)$$

$$c_5 = 0.0209. \quad (4.7)$$

We use the ratio of positive and negative muons based on the measurement at the CMS detector [27],

$$\frac{\mu^+}{\mu^-} = 1.28. \quad (4.8)$$

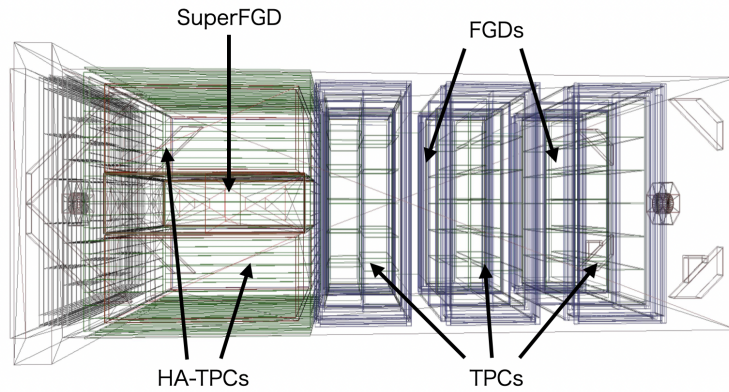


Figure 4.1. Input detector geometries for Geant4 simulation without ECals, magnet, and sand walls (side view).

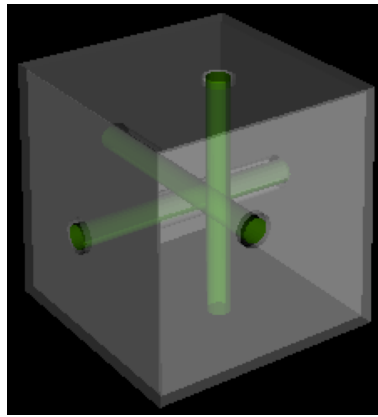


Figure 4.2. SuperFGD cube in the Geant4 simulation.

Other conditions for the simulation are the azimuth angle and the generation point. A uniform distribution is assumed for the azimuth angle distribution. As for the generation point, one point on the top surface of SuperFGD is chosen, then to include the effect of HA-TPC and magnet above the SuperFGD, the point which is 5 meters away from the top surface of the SuperFGD is calculated using the zenith and azimuth angles, and we define this point as the generation point. The effect of the sand wall surrounding ND280 is not considered.

After deciding the initial conditions, the Geant4 simulation is performed. In the Geant4 simulation, each cube's energy deposit and time are calculated.

4.2 Detector response simulation

After the Geant4 simulation, to produce the outputs of cosmic events, we simulate the detector response.

parameter	value	number of corresponding cubes
crosstalk ratio	0.034	6

Table 4.1. Parameter value describing optical crosstalk used in the detector response simulation.

parameter	meaning	value
L	Number of photons after attenuation	
L_0	Number of photons before attenuation	
A_L	Long component of the attenuation	463.4 cm
A_S	Short component of the attenuation	33.2 cm
α	Long fraction of the attenuation	0.77
R	Reflection	
x	Length from cube to MPPC	
l	Length of the fiber	

Table 4.2. Parameter lists and values describing attenuation and reflection used in the detector response simulation.

4.2.1 Energy and number of photons

In the detector response simulation, first, we consider the optical crosstalk between scintillator cubes. Some photons generated by charged particles leak to adjacent six cubes. Crosstalks to cubes touched at the edge or corner are not considered here because the such effect is considered negligible. According to the result of the beam test at CERN using prototype [28], values are set as shown in Table 4.1.

Then, the energy is converted into the number of photons. This conversion factor is 160 photons/MeV/fiber/direction. If one cube has a hit and the energy deposit is E MeV, the number of photons flowing into a fiber from the cube and going toward the MPPC N_0 is

$$N_0 = E \times (1 - 0.034 \times 6) \times 160 = 127.36E \quad (4.9)$$

and the number of photons flowing into a fiber from the adjacent cube and going toward the MPPC N_1 is

$$N_1 = E \times 0.034 \times 160 = 5.44E. \quad (4.10)$$

Then, the attenuation in the wavelength-shifting fiber is considered. The attenuation is simulated as:

$$L = L_0 \times \left\{ \alpha \times \exp\left(-\frac{x}{A_L}\right) + (1 - \alpha) \times \exp\left(-\frac{x}{A_S}\right) \right\}. \quad (4.11)$$

The meaning of each variable and used values in the simulation are listed in Table 4.2. These values come from the measurement at the University of Rochester. In the measurement, the edge of the fiber was mirrored but the fibers of SuperFGD will not be treated so these numbers can be different from the actual ones.

For the evaluation of the reflection, the reflection at the fiber edge is also included in

parameter	value
Dark noise rate	3000 Hz
Gain	7.1×10^5
Pixel crosstalk probability	0.005
Afterpulse probability	0.005

Table 4.3. Parameter lists and values describing MPPC in the detector response simulation

some of the simulations. In this case, we use the following equation:

$$L = L_0 \times \left\{ \alpha \times \exp\left(-\frac{x}{A_L}\right) + (1 - \alpha) \times \exp\left(-\frac{x}{A_S}\right) \right\} + L_0 \times R \times \left\{ \alpha \times \exp\left(-\frac{2l - x}{A_L}\right) + (1 - \alpha) \times \exp\left(-\frac{2l - x}{A_S}\right) \right\}. \quad (4.12)$$

The number of photons reaching the MPPC fluctuates. We assume the Poisson distribution of attenuated value to decide the number.

After the simulation of the fiber, we simulate the response of MPPC. For each channel, the number of photons is converted into pixel hits. We assume the Gaussian distribution for the determination of the pixel that the photon hits. Here, the photon detection efficiency at the MPPC is applied. It is assumed to be 25% in the simulation, according to the datasheet by Hamamatsu Photonics K.K. [19]. Then, we simulate dark noise hits, pixel crosstalks, afterpulses, and pixel voltage recovery time using the value listed in Table 4.3.

By the simulation above, we have lists of pixel hits including time and which pixel is hit, we then calculate the gain of a pixel at the time to simulate the response of MPPC. We consider the n -th pixel voltage V_n of timing $t + \Delta t$ using the equation below:

$$V_n(t + \Delta t) = V_n(t) + (V_{target}(\Delta t) - V_n(t)) \times \left(1 - \exp\left(-\frac{\Delta t}{T_{short}}\right)\right) \quad (4.13)$$

$$V_{target}(\Delta t) = \frac{1}{N} \sum_{i=1}^N V_i(t) + \left(V_{op} - \frac{1}{N} \sum_{i=1}^N V_i(t)\right) \times \left(1 - \exp\left(-\frac{\Delta t}{T_{long}}\right)\right), \quad (4.14)$$

where T_{short} and T_{long} are short and long recovery times respectively. V_{op} is the operation voltage and N is the number of pixels ($N = 2668$). Using this voltage, the gain of the n -th pixel G is calculated photon by photon using the timing of the photon:

$$G(V_n) = (V_n - V_{bd}) \times \frac{C}{1.6 \times 10^{-19}}, \quad (4.15)$$

where C is the pixel capacitance. Each hit is a single-pixel hit, so the charge is just 1.0 if the pixel has full voltage:

$$\text{p.e.} = \frac{G(V_n)}{G(V_{op})}. \quad (4.16)$$

Finally, the charge is smeared by the Gaussian distribution of p.e. peak width. Used values for the calculation of MPPC outputs are listed in Table 4.4. In the simulation of the electronics, we use the sum of those hits as the output charge of the channel.

parameter	meaning	value
T_{short}	short recovery time	8.75 ns
T_{long}	long recovery time	300.0 ns
V_{op}	operation voltage	31.3 V
V_{bd}	breakdown voltage	30.0 V
C	pixel capacitance	8.75×10^{-13} F
σ	p.e. peak width	0.05 p.e.

Table 4.4. Parameter lists and values describing MPPC avalanche in the detector response simulation

4.2.2 Timing

As for the timing, the hit timing of the cube t_0 is calculated by averaging the initial step time in Geant4 simulation t_i and final step time t_f in the cube as:

$$t_0 = \frac{t_i + t_f}{2}. \quad (4.17)$$

Then, the decay time t_d and propagating time t_p at the fiber are added. The decay time at the fiber is considered by assuming single exponential distribution and the used value is 12 ns. This decay time is considered photon by photon. The propagating time is simply calculated using the distance between the cube and the MPPC x . The speed of light in the wavelength-shifting fiber is assumed as 16.0 cm/ns. The propagating time is

$$t_p = \frac{x}{16.0}. \quad (4.18)$$

So, the arrival time t of the photon at the MPPC is calculated as:

$$t = t_0 + t_d + t_p. \quad (4.19)$$

Assuming the CITIROC, we generate the waveform and calculate the timing passing the threshold. We use 3.0 p.e. as a threshold to imitate the beam test at CERN. We impose additional time smearing given by a Gaussian with $\sigma = 0.72$ ns. The standard deviation of the Gaussian is 0.72 ns. This value comes from the time resolution study using the beam test of the SuperFGD Prototype at CERN [29]. An example of the generated waveform is shown in Fig 4.3.

4.2.3 Example of generated cosmic event

An example of a cosmic event is shown in Fig. 4.4. Figure 4.4 (a-c) shows three 2D outputs. These are the raw outputs from SuperFGD. Figure 4.4 (d) shows a 3D event display of a cosmic event. By combining three 2D event readouts, we reconstruct the track of the particle.

The z axis is along the neutrino beam. The x and y axis are perpendicular to the beam and the y axis is vertical.

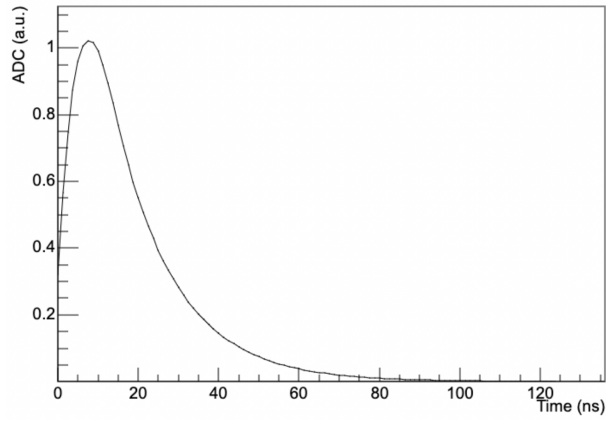


Figure 4.3. An example of the generated waveform.

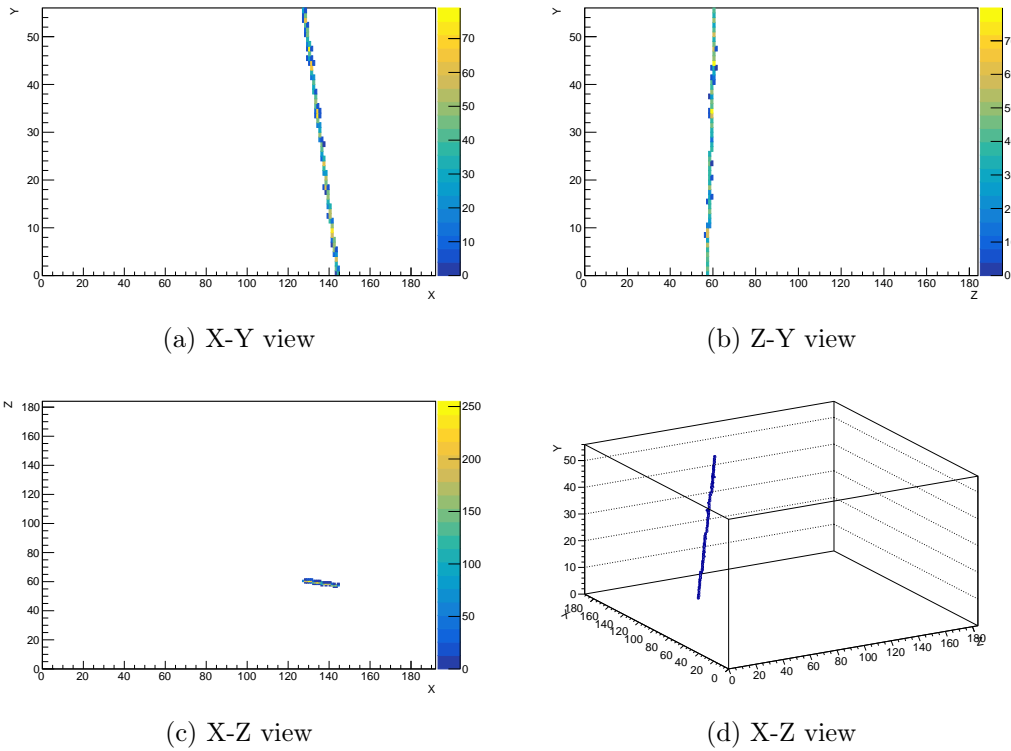


Figure 4.4. 2D and 3D event display of a cosmic event. The unit of 2D readouts is the number of photons.

4.3 Estimation of cosmic event rate and required time

As mentioned in Chap. 3, we plan to take cosmic data for calibration before starting the operation. We have at least one month after the installation into the pit and before the physics run. Since we also need to work on other preparations, we assume to have about two weeks to take cosmic data. The methods we develop must meet the requirements using the number of events we obtain in that time period.

By tuning the trigger scheme, we try to take cosmic data uniformly over the detector as much as possible. However, if we do not tune the trigger, about five times fewer events are hit at the edge of the detector as shown in Fig. 4.5. In this thesis, the uniform distribution of hit positions is assumed. All the channels, even channels close to the edge of the detector should meet the requirements, so we discuss using cosmic ray data for one day in this thesis.

We calculate cosmic muon flux by integrating differential cosmic muon flux given by Eq. (4.1) over the position of cosmic muons reaching the surface of SuperFGD, the direction of cosmic muons, and their energies. The region we integrate is listed in Table 4.5. We have more cosmic muons outside these ranges, especially low momentum regions, so the calculated flux below is underestimated. According to the calculation, the cosmic muon flux is about 206 particles/second.

The data acquisition system limits the data-taking rate for the actual detector. When we take cosmic ray data for calibration, we expect the event rate to be 10–50 Hz for SuperFGD. Since this thesis assumes one day, the number of events is 864,000 assuming 10 Hz. The developed calibration methods are evaluated assuming these statistics.

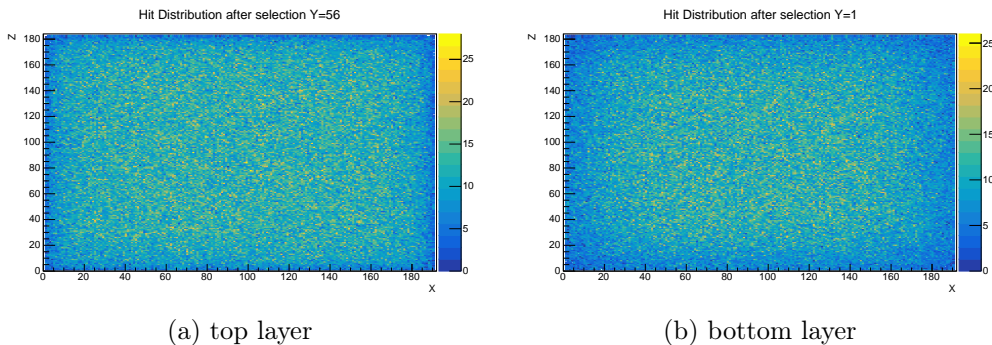


Figure 4.5. Number of hits at each cube for one million cosmic events of our simulation. For the center of the top layer, the number of hits is about fifteen on average. For the edge of the bottom layer, the number of hits is about three on average.

parameter	meaning	region
x	x coordinate on the top surface of SuperFGD	$[0, 192]$ cm
z	z coordinate on the top surface of SuperFGD	$[0, 182]$ cm
θ	zenith angle	$[0, \pi/2]$
ϕ	azimuth angle	$[0, 2\pi]$
ζ	vertical component of energy	$[1, 100]$ GeV

Table 4.5. Regions of integration for the calculation of cosmic muon flux.

Chapter 5

Basic Light Yield Calibration

We develop calibration methods for the basic light yield. The calibration of light attenuation and reflection in the fiber is considered to estimate the light yield from the scintillator cube.

5.1 Motivation and required precision

It is important to achieve good uniformity of light yield because neutrino energy reconstruction and particle identification (PID) are done using the light yield at the cube. The neutrino energy for CCQE interaction can be reconstructed from the lepton momentum and direction. The lepton momentum is reconstructed using TPCs and HA-TPCs because the tracking efficiency is better than the scintillator. Because the effect of the Fermi momentum of the nucleon introduces an intrinsic uncertainty of neutrino energy of about 10%, the requirement of momentum resolution for TPCs and HA-TPCs is set to 10% [14].

For shower events or the particle stopping inside SuperFGD, the energy is estimated using the observed number of photons. We set the requirement for the light yield uncertainty of SuperFGD to be 10%. To reconstruct a track, we need a track length of at least 3 cm. The total light yield for a MIP is expected to be more than 300 p.e. The resolution related to the Poisson fluctuation is less than $1/\sqrt{300} = 5.8\%$. To achieve the total uncertainty of 10%, the calibration is need to be better than $\sqrt{10^2 - 5.8^2} = 8.1\%$.

As for PID, the differences of energy deposit between proton and pion or electron and converted gamma-ray are about two times or more [30] [23]. To distinguish these particles at 3σ , the requirement for the light yield uncertainty of SuperFGD is 33% including the effect of the statistical fluctuation. It is looser than the requirement for the momentum resolution.

Based on these considerations, we set the requirement for the uniformity of light yield calibration over the whole detector, including the variation along the fiber and each readout channel, to be 8.1%.

5.2 Light yield at the cube and attenuation in the fiber

The attenuation for the light produced at a distance x from the MPPC is expressed as

$$L = L_0 \times \left[\alpha \times \exp\left(-\frac{x}{A_L}\right) + (1 - \alpha) \times \exp\left(-\frac{x}{A_S}\right) \right], \quad (5.1)$$

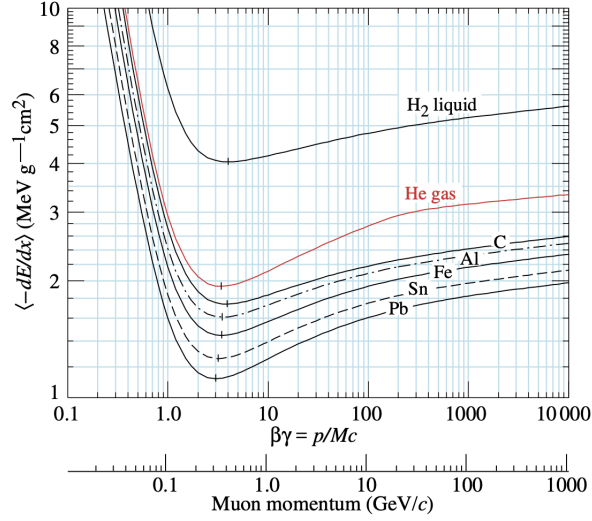


Figure 5.1. Mean energy loss rate in some substances [31].

where the reflection at the fiber edge is ignored and the effect of the reflection will be discussed in the next section. We assume two attenuation lengths A_L and A_S for the long and short attenuation length components, respectively, and α as the fraction of the long attenuation length component because the attenuation length of the fiber depends on the wavelength of the photons propagating in the fiber. L_0 is the light yield without the attenuation effect including the scintillator light yield, capture efficiency of the scintillation light of the wavelength-shifting fiber, fiber-MPPC coupling, and photon detection efficiency of MPPC. Because these effects cannot be disentangled in the real detector, we determine the effective light yield L_0 which includes all of these effects.

To obtain A_L , A_S , and α , we use cosmic events. The peak momentum of cosmic muons is around 1 GeV, which is close to the minimum ionizing as shown in fig 5.1. Because the energy that cosmic muons lose in the unit length is relatively constant, we can use cosmic data.

5.2.1 Horizontal fibers

When only one x (z) fiber in a y layer has a hit, it is called a “single fiber hit.” Figure 5.2 shows an example of single fiber hits. A muon track is reconstructed by linear fits in x - y and z - y planes using these single-fiber hits:

$$x = ay + b, \quad (5.2)$$

$$z = cy + d. \quad (5.3)$$

For each single fiber hit, the position along the x (z) fiber is defined using hit information in the z (x) fiber of the same y layer. When multiple z (x) fibers have hits, the position of a hit with the largest light yield is defined as the z (x) position.

The charge normalized by the path length of the track through the cube q is calculated as:

$$q = \frac{q_0}{\sqrt{a^2 + 1^2 + c^2} \times 1.007}, \quad (5.4)$$

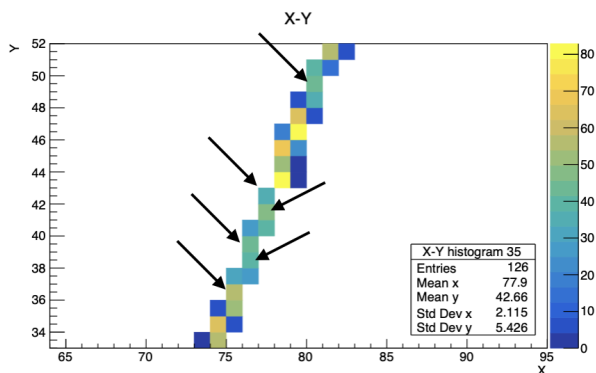


Figure 5.2. Display of hits for z fibers in a simulated cosmic ray event. Color represents the number of photoelectrons observed by each MPPC. The ‘single fiber hits’ are indicated by arrows.

parameter	α	A_L	A_S
Simulation Input	0.77	463.4	33.2
x fiber	0.7895 ± 0.0007	449.1 ± 1.3	34.1 ± 0.3
z fiber	0.7948 ± 0.0007	439.8 ± 1.4	33.4 ± 0.3

Table 5.1. Parameters used in the simulation and obtained by fittings.

where q_0 is the observed charge before normalization and 1.007 is the width of the sensitive region of the cube in the simulation (unit is cm).

The attenuation parameters are estimated from the dependence of q on the distance from MPPC. Hits are grouped into a unit of four consecutive cubes along the fiber. Figure 5.3 shows an example of q distribution for four cubes. The mean of each position is fit with Eq. (5.1) to obtain the parameters.

In the simulation, the same attenuation parameters are used for all the fibers. We sum up hits in all the x (z) fibers in one million simulated events to increase the statistics. The mean of q as a function of the distance to MPPC together with the fitting results are shown in Fig. 5.4. The values of parameters used in the simulation and obtained by fitting are summarized in Table 5.1. Obtained values are not consistent with the input value. By summing up one million cosmic events, we evaluate the systematic uncertainty of this method. Figure 5.5 shows the mean of q as a function of the distance to MPPC together with 1σ confidence interval at each cube normalized by obtained attenuation curve using one million events. The maximum deviations from fit lines for x and z fibers are 0.9% and 1.2%, respectively.

To check if there is any dependence of attenuation calibration on the y position, we simulate one million cosmic events and repeat the calibration procedure for each y layer. Figure 5.6 shows the results of fittings. No y dependence is observed.

As hits of about 10,000 channels are summed, 86 simulated events correspond to the statistics of one-day data taking. The mean of q as a function of the distance to MPPC together with 1σ confidence interval at each cube using 86 events are shown in Fig. 5.7. The 1σ confidence intervals are calculated using the gradient of each fitting parameter at that point and the covariance matrix of fitting parameters. The one σ confidence intervals

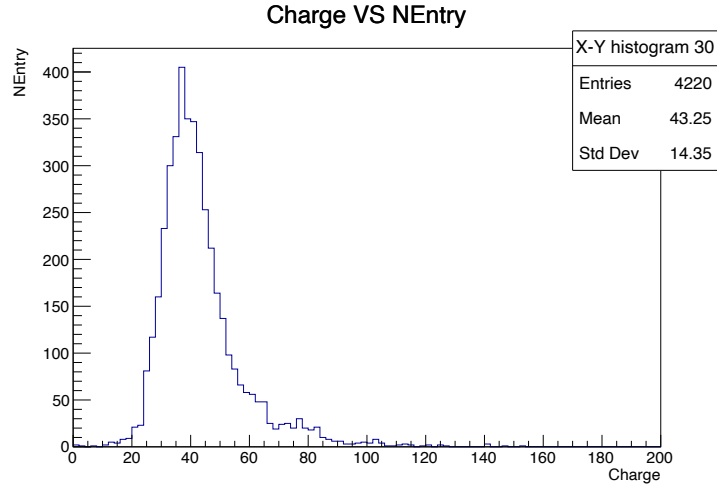


Figure 5.3. Normalized charge distribution for four cubes.

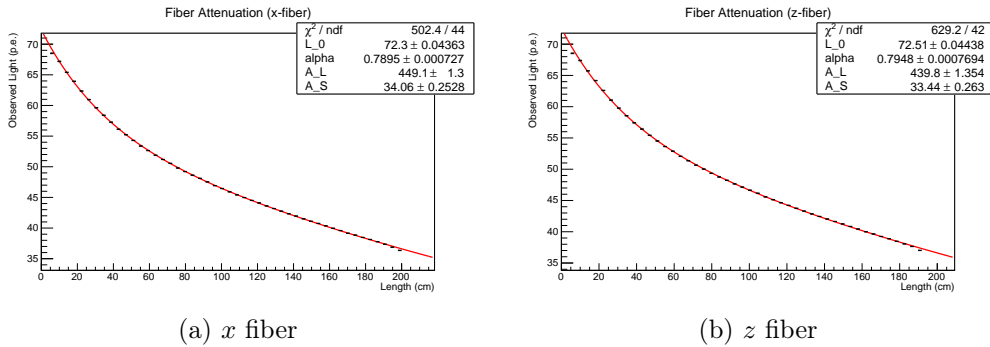


Figure 5.4. Mean of q as a function of the distance to MPPC together with the fitting results.

are within the requirement for the whole region. The largest confidence intervals for x and z fibers are 2.7% and 1.5%, respectively.

Table 5.2 shows the summary of the statistical uncertainty assuming one-day data-taking and systematic uncertainties for horizontal fibers. Data-taking for one day is enough for the requirement.

5.2.2 Vertical fibers

Because the direction of the cosmic muon is mostly vertical, it is difficult to find a single-fiber hit in the x - z plane. We cannot use the same method as horizontal fibers for vertical (y) fibers. For y fibers, the corresponding path lengths are estimated from the information of the tracks reconstructed using single fiber hits in x - y and z - y planes. The position is defined as the center of the path.

We need to take into account the effect of optical cross-talk between scintillator cubes. For a middle layer, the fiber collects cross-talk photons from the layers above and below. For the top and bottom layers, there is less contribution from cross talk and thus light yields

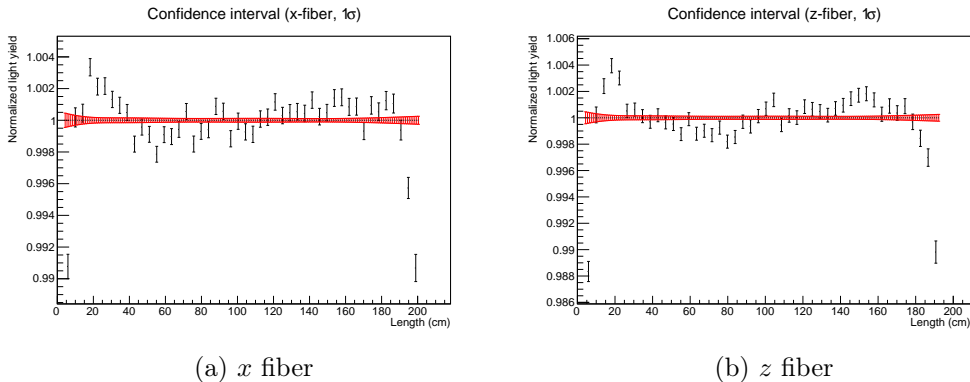


Figure 5.5. Mean of q as a function of the distance to MPPC (black) with 1σ confidence interval at each position of the cube (red) using one million events for x and z fibers. Observed light yields are normalized by obtained attenuation curve.

fiber	statistical	systematic
x fiber	2.7%	0.9%
z fiber	1.5%	1.2%

Table 5.2. Summary of statistical uncertainty assuming one-day data-taking and the systematic uncertainties for horizontal fibers.

are smaller. Hence we do not use top and bottom layers for the light yield and attenuation calibration. Since the direction of the cosmic muon is mostly vertical, rejecting only the top and bottom layers is not enough. To determine the unused region, we check the path length of tracks for each fiber along the y direction. As shown in Fig. 5.8, the fraction of fibers with more than 6 cm of path length along y direction is less than 1%. Since we define the position as the center of the path, we decide not to use the points within 3 cm from the top and bottom surfaces in the fitting. The light yield for an y fiber could be very large. We use the truncated mean by discarding hits with the smallest 10% and largest 10% signal.

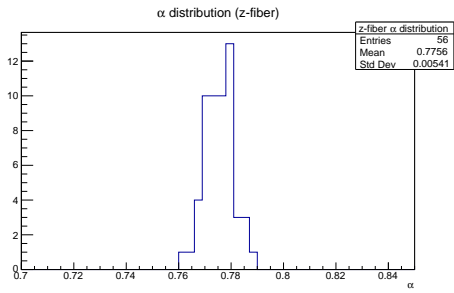
The mean of q as a function of the distance to MPPC together with the fitting results are shown in Fig. 5.9. Here, we fix the value of the long component because y fibers are short. The long component does not affect the attenuation. Table 5.3 summarizes the results. Obtained values are not consistent with the input value. By summing up one

parameter	α	A_L	A_S
Simulation Input	0.77	463.4	33.2
y fiber	0.7997 ± 0.0008	400	36.6 ± 0.4

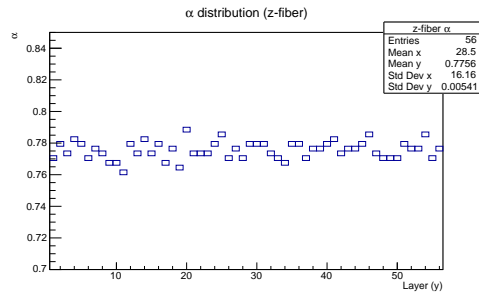
Table 5.3. Parameter values used in MC simulation and the obtained values for y fiber.

million cosmic events, we evaluate the systematic uncertainty of this method. Figure 5.10 shows the mean of q as a function of the distance to MPPC together with 1σ confidence interval at each cube normalized by obtained attenuation curve using one million events. The maximum deviation from the fit line is 0.4%.

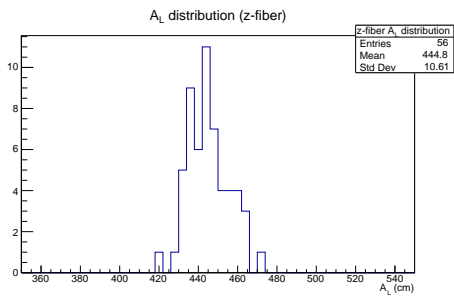
As hits of about 40,000 channels are summed, 22 simulated events correspond to the



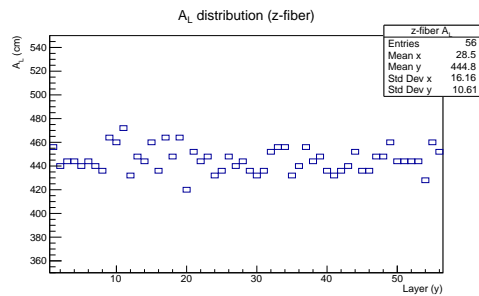
(a) α distribution



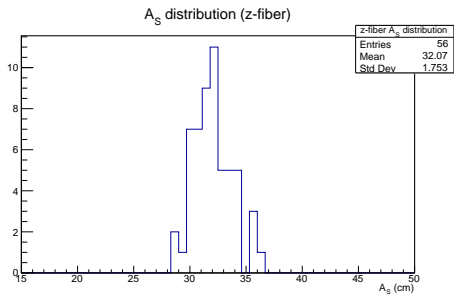
(b) α according to y coordinate



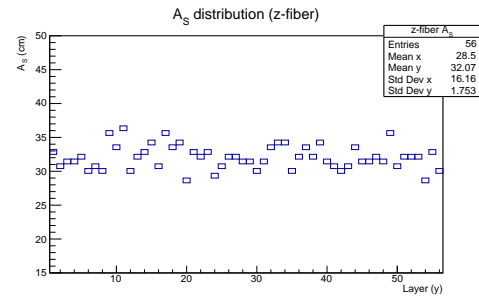
(c) A_L distribution



(d) A_L according to y coordinate



(e) A_S distribution



(f) A_S according to y coordinate

Figure 5.6. Results of horizontal slice fits.

statistics of one-day data taking. Means of q as a function of the distance to MPPC together with 1σ confidence interval at each cube normalized by obtained attenuation curve using 22 events are shown in Fig. 5.11. The one σ confidence intervals are within the requirement in the fit region. The largest confidence interval for y fibers is 4.1% in the fitting region.

Table 5.4 shows the summary of statistical uncertainty assuming one-day data-taking and systematic uncertainties for horizontal fibers. Data-taking for one day is sufficient to satisfy the requirement.

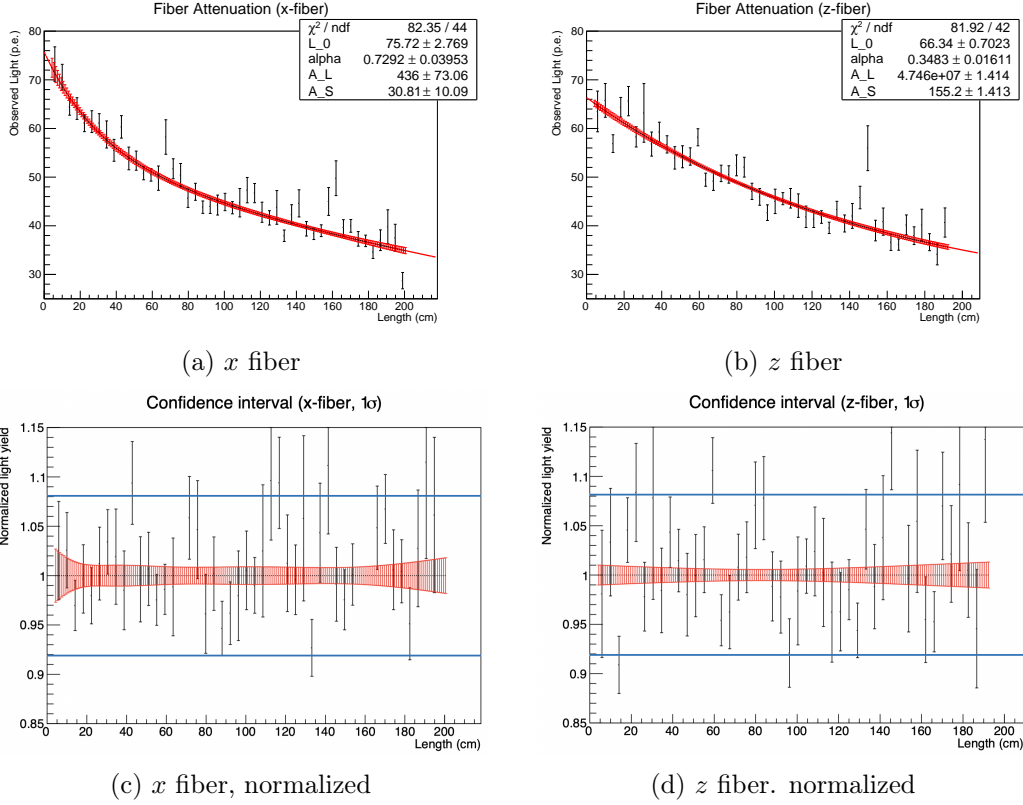


Figure 5.7. Mean of q as a function of the distance to MPPC (black) with 1σ confidence interval at each position of the cube (red) using 86 events for x and z fibers. Observed light yields normalized by obtained attenuation curve are also shown. Blue lines show the requirement (8.1%).

fiber	statistical	systematic
y fiber	4.1%	0.4%

Table 5.4. Summary of statistical uncertainty assuming one-day data-taking and systematic uncertainties for vertical fibers.

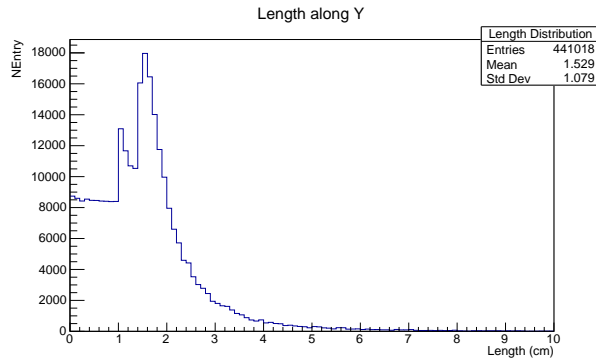


Figure 5.8. Distribution of length of tracks in each channel along the y direction.

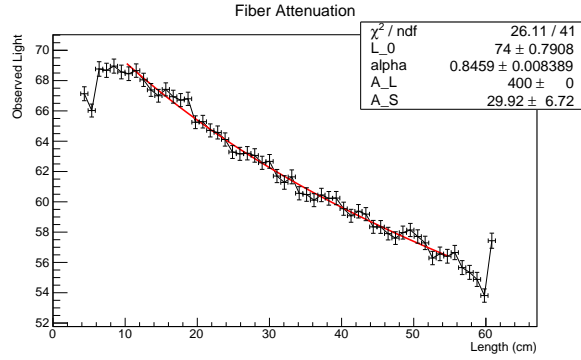


Figure 5.9. Mean of q as a function of the distance to MPPC together with the fitting results.

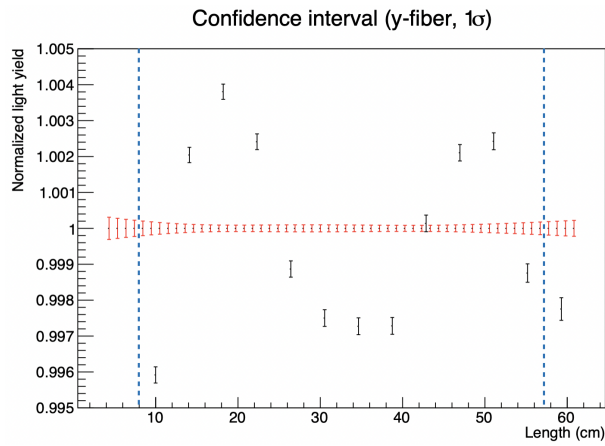


Figure 5.10. Mean of q as a function of the distance to MPPC (black) with 1σ confidence interval at each position of the cube (red) using one million events for y fiber. Observed light yields are normalized by obtained attenuation curve. Points between the two blue vertical dot lines are used for fitting.

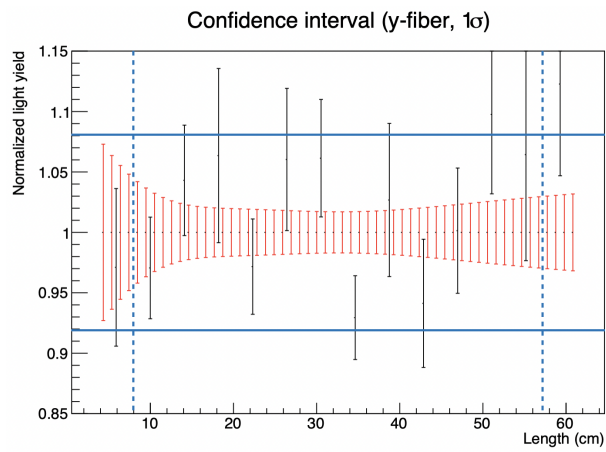


Figure 5.11. Mean of q as a function of the distance to MPPC (black) with 1σ confidence interval at each position of the cube (red) using 22 events for y fiber. Observed light yields are normalized by obtained attenuation curve. Horizontal blue lines show the requirement (8.1%) and points between the two blue vertical dot lines are used for fitting.

5.3 Reflection at the fiber edge

5.3.1 Expected value

The reflection rate depends on the polarization of the photon: p-wave or s-wave, and the angle of incidence α and the angle of refraction β . The reflection rate for p-wave r_p and s-wave r_s can be written as:

$$r_p = \left(\frac{n_2 \cos \alpha - n_1 \cos \beta}{n_2 \cos \alpha + n_1 \cos \beta} \right)^2 = \left(\frac{\tan(\alpha - \beta)}{\tan(\alpha + \beta)} \right)^2 \quad (5.5)$$

$$r_s = \left(\frac{n_1 \cos \alpha - n_2 \cos \beta}{n_1 \cos \alpha + n_2 \cos \beta} \right)^2 = \left(\frac{\sin(\alpha - \beta)}{\sin(\alpha + \beta)} \right)^2 \quad (5.6)$$

Here, n_1 is the refractive index of the inside of the fiber. Assuming the core of Y-11, n_1 is 1.59. n_2 is the refractive index of the outside of the fiber. Assuming the air, n_2 is 1.0. Assuming all the light comes perpendicular to the edge of the fiber, the estimated reflection rate R can be calculated as

$$R = \left(\frac{n_1 - n_2}{n_1 + n_2} \right)^2 \simeq 0.052 \quad (5.7)$$

For the light with a critical angle of propagation in the fiber, $\alpha = 26.7^\circ$ and $\beta = 45.7^\circ$, the reflection rates are

$$r_p \simeq 0.012 \quad (5.8)$$

$$r_s \simeq 0.117 \quad (5.9)$$

Because the edge of fibers will not be polished, the angle of the light can change, so a part of reflected photons cannot propagate in the fiber anymore. Therefore, the reflection rate R can be estimated to be about or less than 5%.

5.3.2 Measurement of the reflection

To check the size of the reflection, we measure the reflection at the edge of the fiber by injecting laser light. The principle of the measurement is as follows.

We inject a laser at 10 cm from the MPPC. We tune the intensity of the laser so that the average output is less than one photon. If I photons are reemitted at the injection point of the laser and start to travel in both directions, the average number of photons at the MPPC can be written as:

$$N_{dir} = I \times F(x) \times k, \quad (5.10)$$

$$N_{ref} = I \times R \times F(2l - x) \times k, \quad (5.11)$$

where N_{dir} and N_{ref} are the number of photons observed at MPPC directly and reflected. l is the length of the fiber and R is the reflectivity. k is the photon detection efficiency at MPPC. $F(x)$ is the attenuation factor:

$$F(x) = \alpha \exp\left(-\frac{x}{A_L}\right) + (1 - \alpha) \exp\left(-\frac{x}{A_S}\right), \quad (5.12)$$

where A_L and A_S are long and short attenuation length, respectively, and α is the fraction of long component.

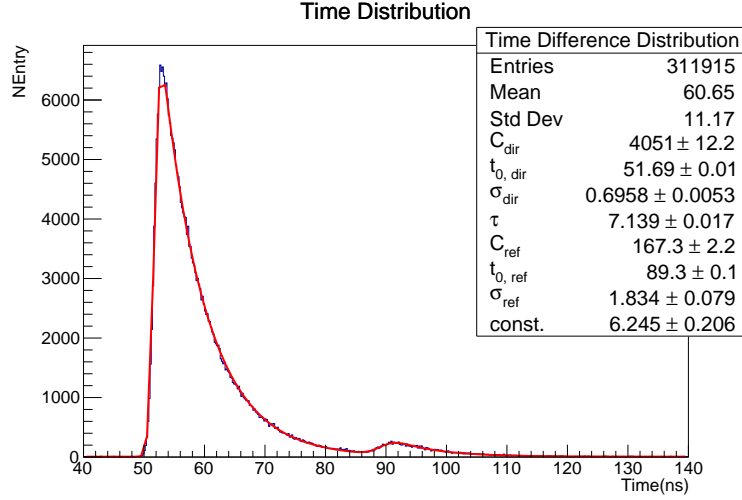


Figure 5.12. Time distribution of one photon events.

We use data that just only one photon is observed at the MPPC. If the ratio that we detect one photon at MPPC is P_{dir} and P_{ref} , the relationship between P and N is

$$P_{dir} = Poisson(N_{dir}, 1) \quad (5.13)$$

$$P_{ref} = Poisson(N_{ref}, 1). \quad (5.14)$$

Here, $Poisson(N, 1)$ means the probability of one photon when the mean is N , assuming Poisson distribution.

$$Poisson(N, 1) = \frac{N^1 e^{-N}}{1!} = N e^{-N} \quad (5.15)$$

By measuring P_{dir} and P_{ref} , we estimate N_{dir} and N_{ref} . The ratio of N_{dir} and N_{ref} is

$$\frac{N_{ref}}{N_{dir}} = \frac{R \times F(2l - x)}{F(x)} \quad (5.16)$$

So if we know the attenuation factor, we estimate R by this measurement.

To distinguish the direct and reflected photon, we use timing that the photon is detected at the MPPC. Figure 5.12 shows the time distribution of detected photons. The fitting function is the sum of the two convolution functions of Gaussian and exponential plus a constant term to represent random background:

$$C_{dir} \left\{ 1 + \operatorname{erf} \left(\frac{t - t_{0,dir} - \frac{\sigma_{dir}^2}{\tau}}{\sqrt{2}\sigma_{dir}} \right) \right\} \cdot \exp \left(-\frac{t - t_{0,dir}}{\tau} \right) \quad (5.17)$$

$$+ C_{ref} \left\{ 1 + \operatorname{erf} \left(\frac{t - t_{0,ref} - \frac{\sigma_{ref}^2}{\tau}}{\sqrt{2}\sigma_{ref}} \right) \right\} \cdot \exp \left(-\frac{t - t_{0,ref}}{\tau} \right) + const., \quad (5.18)$$

where C_{dir} and C_{ref} are area constants, $t_{0,dir}$ and $t_{0,ref}$ are starting time, σ_{dir} and σ_{ref} are time resolutions, and τ is the decay time of the fiber.

The length of the fiber is longer than 3 m. Because the effective length of the fiber for direct and reflected photons in this measurement is different, we use different attenuation

parameter	short	long
A_L	150.6	280.4
A_S	5.87	15.41
α	0.77	0.68

Table 5.5. Parameters and values used for the calculation taken from [32].

length (cm)	R
330	4.2%
329	3.7%
328	2.9%
327	2.9%
326	3.3%
325	2.8%

Table 5.6. Results of reflection measurement.

factors for direct and reflected photons. For direct photons, the path length in the fiber is 10 cm, so we use the attenuation factor measured with 60 cm wavelength-shifting fiber [32]. On the other hand, for reflected photons, the path length in the fiber is about 650 cm, so we use the attenuation factor measured with 2 m wavelength-shifting fiber. Used values are summarized in Table 5.5. We repeat the measurement six times by cutting the edge of the fiber every time. The result is summarized in Table 5.6. As expected, the reflection rate is less than 5%.

5.3.3 Degeneration

If we consider the reflection, four components can contribute to the light yield; each of direct and reflected light has long and short components. The function of each component is listed below:

$$L_1 = L_0 \times \alpha \times \exp\left(-\frac{x}{A_L}\right) \quad (5.19)$$

$$L_2 = L_0 \times (1 - \alpha) \times \exp\left(-\frac{x}{A_S}\right) \quad (5.20)$$

$$L_3 = L_0 \times R \times \alpha \times \exp\left(-\frac{2l - x}{A_L}\right) \quad (5.21)$$

$$L_4 = L_0 \times R \times (1 - \alpha) \times \exp\left(-\frac{2l - x}{A_S}\right), \quad (5.22)$$

where x is the length from the MPPC. If the reflection rate is 5%, the contribution of each component is as shown in Fig. 5.13. The reflected short component L_4 is small enough. For example, assuming $L_0 = 70.0$ p.e., $R = 0.05$, $\alpha = 0.77$, $A_S = 33.2$ cm, and $l = 200$ cm, $L_4 \simeq 1.9 \times 10^{-3}$ at $x = 200$ cm. Since it is much smaller than 1, we ignore L_4 .

As for long components L_1 and L_3 , because A_L is larger than the length of the fibers, the two components are almost linear, as seen in Fig. 5.13. If A_L is long enough, long

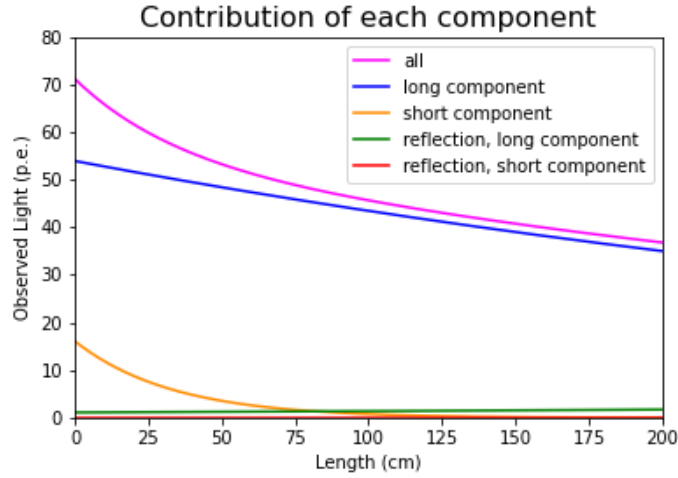


Figure 5.13. Attenuation curve including reflection $R = 0.05$ (pink) as the function of x in the case of 2 m fiber. Each component L_1 to L_4 is also shown.

components can be written as:

$$L_1 \simeq L_0 \times \alpha \times \left(1 - \frac{x}{A_L}\right) \text{ and} \quad (5.23)$$

$$L_3 \simeq L_0 \times R \times \alpha \times \left(1 - \frac{2l - x}{A_L}\right). \quad (5.24)$$

Using

$$K = 1 + R - \frac{2lR}{A_L} \text{ and} \quad (5.25)$$

$$A'_L = \frac{A_L \times K}{1 - R}, \quad (5.26)$$

the sum of long components can be written as:

$$L_1 + L_3 \simeq L_0 \times \alpha \times K \times \left(1 - \frac{x}{A'_L}\right). \quad (5.27)$$

This is an approximation function of another exponential function. If we use an exponential form, the sum of long components is

$$L_1 + L_3 \simeq L'_0 \times \exp\left(-\frac{x}{A'_L}\right), \quad (5.28)$$

where L'_0 is

$$L'_0 = L_0 \times \alpha \times K. \quad (5.29)$$

We can write the sum of four components as:

$$L \simeq L'_0 \times \exp\left(-\frac{x}{A'_L}\right) + L_0 \times (1 - \alpha) \times \exp\left(-\frac{x}{A_S}\right) \quad (5.30)$$

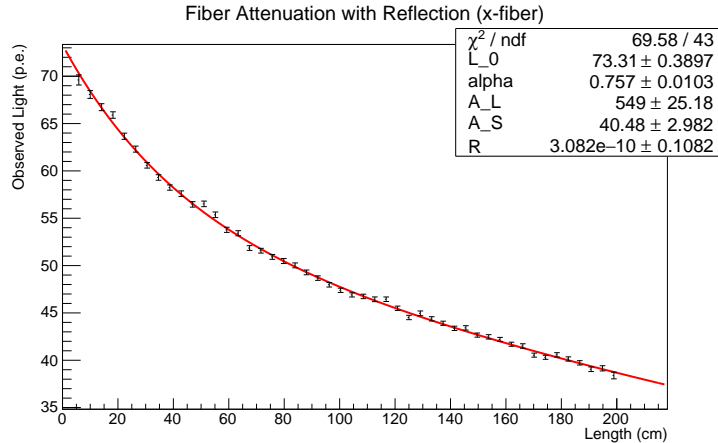


Figure 5.14. Fitting result of fiber attenuation. R in the simulation is 5%. The fitting function includes reflection terms.

If we take another parameterization, this equation is written as:

$$L \simeq L_c \times \left[\beta \times \exp\left(-\frac{x}{A'_L}\right) + (1 - \beta) \times \exp\left(-\frac{x}{A_S}\right) \right] \quad (5.31)$$

This is the same form as the function without reflection Eq. (5.1). For this reason, it is difficult to obtain R by fitting, and we can find that L_0 , α , and A_L are biased. An example of the result is shown in Fig. 5.14. We simulate 10,000 cosmic events and sum up all the fibers. As for R , it seems difficult to measure using cosmic data, as we expect. R is consistent within 1σ but the error is large even if we use large statistics.

5.3.4 Treatment of the reflection

Because we cannot obtain the parameter R by fitting, we need to decide how to treat this parameter. As mentioned above, the attenuation including the reflection can be fitted with a function without reflection Eq. (5.1) with some parameters biased. One possibility is using this function to describe attenuation and reflection. In this case, L_0 and A_L are biased with the length of the fiber. Another possibility is obtaining R at the external measurement and using that value.

To evaluate the systematic uncertainty of the first option, we compare the true attenuation curve with reflection and fit with the function not including the reflection term, as shown in Fig. 5.15. The true attenuation curve is calculated using Eq. 4.12 with $R = 0.05$. The maximum difference between the two is 0.04% and 0.1% for horizontal and vertical fiber, respectively. The effect of reflection is negligible because they are small enough compared to the uncertainty coming from the attenuation.

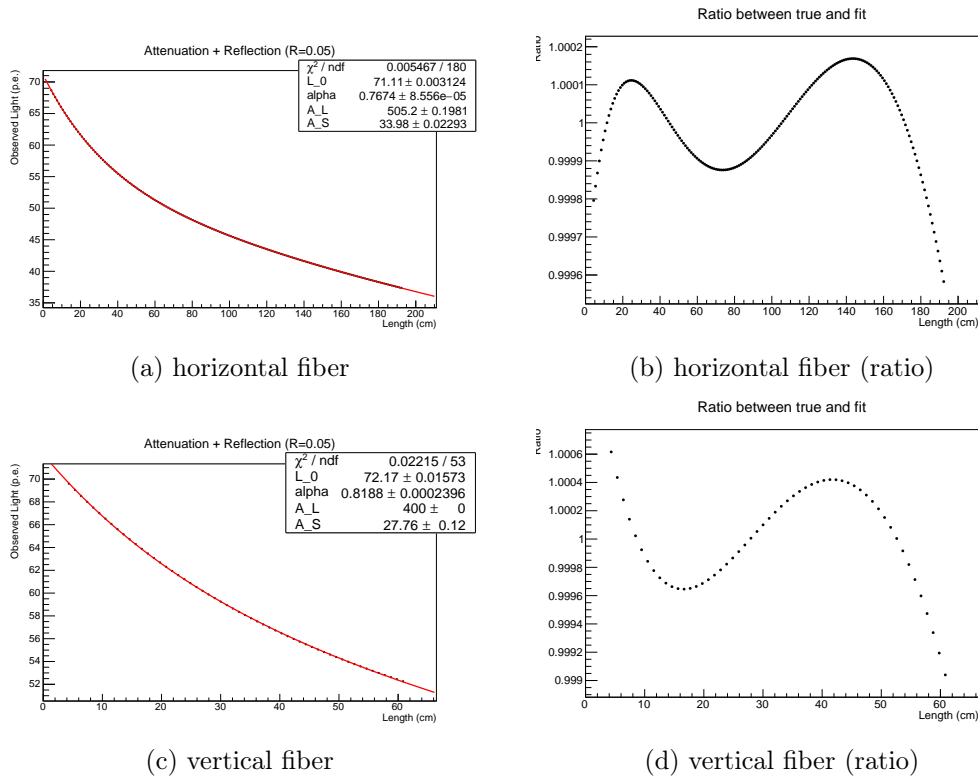


Figure 5.15. True mean of q as a function of the distance to MPPC together with fitting curve not including attenuation term (left). The ratio of true points and fit curve (right).

5.4 Uncertainty of light yield calibration

The uncertainties related to fiber (attenuation and reflection) and light yield are summarized in Table 5.7. We assume cosmic events for one day. They are within the requirement of 8.1%.

Direction	statistical	systematic	total
x fiber	2.7%	0.9%	3.6%
y fiber	4.1%	0.4%	4.5%
z fiber	1.5%	1.2%	2.7%

Table 5.7. Statistical and systematic uncertainties related to fiber and light yield assuming cosmic data of one day.

Chapter 6

Additional Effects on Light Yield

In addition to the basic light yield, we need to take into account the optical crosstalk and quenching effect of the scintillator. They affect the observed light yield, especially when it is large.

6.1 Motivation

As for the optical crosstalk, measuring how much light is shared among neighboring cubes is crucial. If a large amount of photons leaks to the adjacent cubes, 3D reconstruction from 2D readouts becomes complicated. It is measured to be about 3% at the test beam experiments at CERN [28] [30] and at ELPH at Tohoku University [33]. Nevertheless we need to check it using the real detector. It affects the observed number of photons because some photons flow into the adjacent cubes and are not captured by the same fiber.

The quenching effect is also important for the points the particle loses large energies, especially the stopping point of the particle. Assuming that the same quenching level as the SciBar detector in the K2K experiment [34], light yield decreases about 13% for a proton with a momentum of 500 MeV. To measure the energy with 10% precision, this number is not negligible.

6.2 Optical crosstalk

6.2.1 Beam test results

We have estimates of the crosstalk rate based on the beam test results. One of such estimate is based on the beam test at CERN using a prototype with $24 \times 8 \times 48$ cubes [30]. Figure 6.1 (a) shows one hit cube and four crosstalk cubes. The definition of each parameter is also shown. We define the crosstalk parameter κ as

$$\kappa = \frac{M_{xtalk}}{M_{main} + 2M_{xtalk}}. \quad (6.1)$$

The numerator is the output of one crosstalk channel and the denominator is the output of the center cube and four crosstalk cubes because M_{main} is the sum of the light from the center cube and two crosstalk cubes. If the crosstalks between the beam direction z are completely canceled, this denominator is all the output from photons produced at the one cube, and κ is the crosstalk rate for one adjacent cube. Figure 6.1 (b) shows the result.

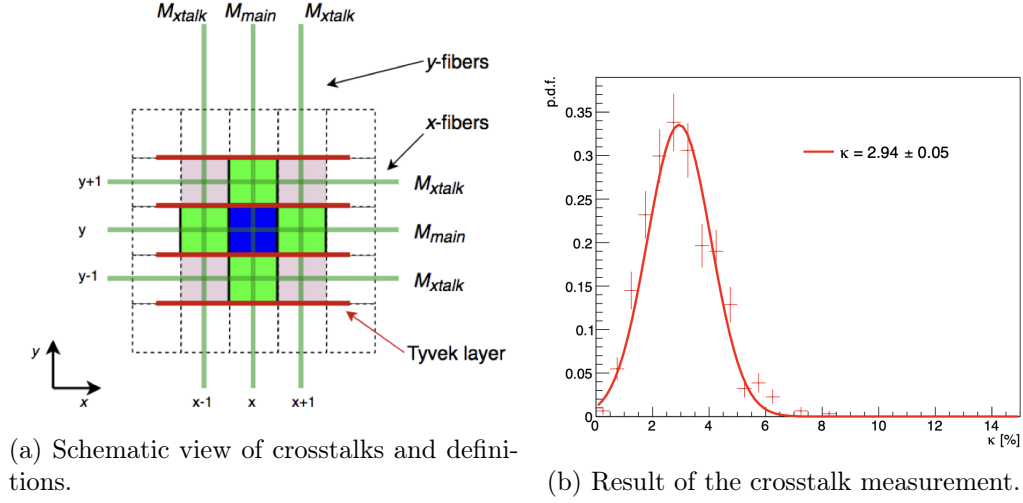


Figure 6.1. Definition and result of the beam test at CERN [30].

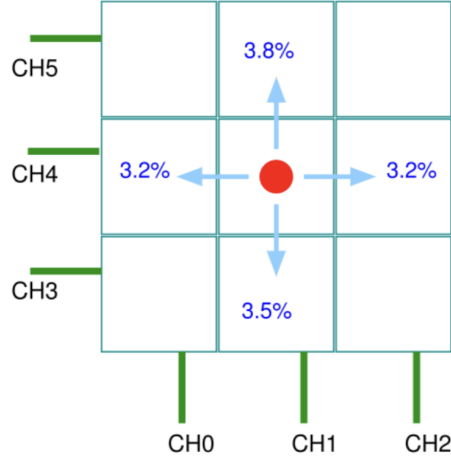


Figure 6.2. Crosstalk from the central cube to adjacent cubes [28].

This measurement was done using a stopping point of protons to make not only M_{main} but also M_{xtalk} larger than the readout threshold. Because we used the stopping point of protons, the crosstalks in the z direction were not canceled and κ should be larger than the obtained value.

We have another measurement result using $5 \times 5 \times 5$ cubes prototype at CERN [28]. Figure 6.2 shows the result of the measurement. In this measurement, they used 6 GeV/ c positive particles: mainly protons and positrons. The average crosstalk is 3.4% per side.

Another measurement was done at ELPH at Tohoku University [33] using $3 \times 3 \times 1$ cubes. The result of the optical crosstalk ratio is 3.0% using the readouts along the beam. The results of three measurements are summarized in Table 6.1.

configuration	result
$24 \times 8 \times 48$ cubes	> 2.9%
$5 \times 5 \times 5$ cubes	3.4%
$3 \times 3 \times 1$ cubes	3.0%

Table 6.1. Beam test results.

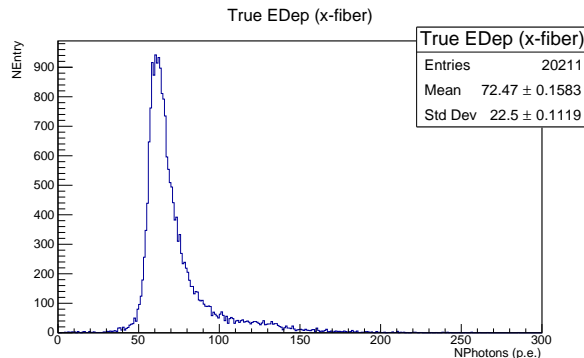


Figure 6.3. True energy deposit in a channel normalized by path length for x fiber.

6.2.2 Monte Carlo simulation and possibility of calibration using cosmic muons

In the MC simulation, based on the result using $5 \times 5 \times 5$ cubes prototype at CERN, we use 3.4% to six adjacent cubes.

For a typical cosmic muon whose light yield is about 40 p.e., the estimated light yield from the crosstalk cube is less than 1.5 p.e. Currently, we plan to set the threshold of SuperFGD to be about 2.5 or 3 p.e. to avoid electronic noise, so most of the crosstalks of cosmic muons will not be recorded. However, light yields statistically fluctuate and some cosmic muons lose a large amount of energy in a cube as shown in Fig. 6.3. The optical crosstalk ratio can be measured using such cosmic muons.

In order to distinguish the crosstalk events and events in which a track passes the edge of the cube, we use three successive single-cube hits as shown in Fig. 6.4. The pink and red cubes have hits and we use outputs of the center layer.

Figure 6.5 shows the observed light distributions from the main cube and crosstalk cube using simulation. We use 3 p.e. as a threshold in the simulation and about half of the events with 3 p.e. are counted as 0 p.e. From the output from the main cube, we can predict the charge distribution for a certain value of κ . By changing κ and comparing the predicted distribution and the observed distribution, we can get the most probable value of κ . Figure 6.6 shows the predicted charge distributions with various values of κ . We use Fig. 6.5 (a) as the input distribution of the light yield from the main cube.

The χ^2 defined below is used to compare the predicted and observed charge distribution:

$$\chi^2 = \sum_{pe=4}^{10} \frac{(N_{pe,observed} - N_{pe,estimated})^2}{N_{pe,estimated}}. \quad (6.2)$$

We do not use hits below 4 p.e. because they are affected by the threshold. Also, we do

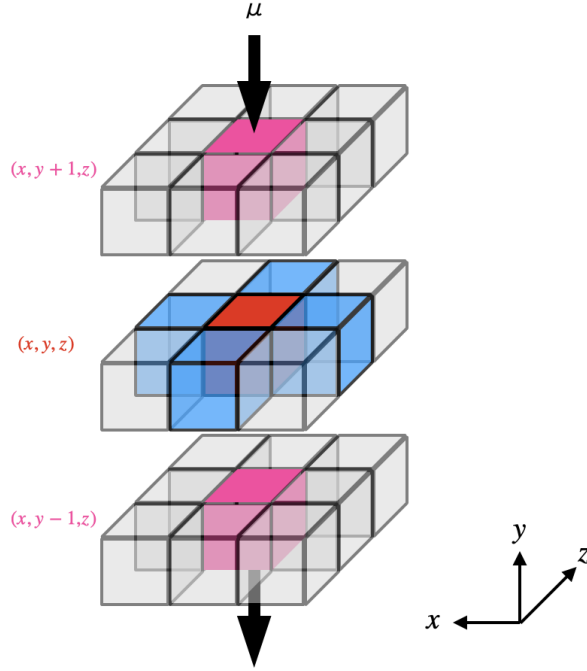


Figure 6.4. Three successive single-cube hits. The red cube is the main cube and the blue cubes are the crosstalk cubes.

not use hits above 10 p.e. because we have few events in that region as shown in Fig. 6.5. Figure 6.7 shows χ^2 as a function of κ . χ^2 has a minimum around $\kappa = 0.035$. The true value is $\kappa = 0.034$ so the minimized point is slightly shifted to the upper side. This 0.001 change makes the light yield from the crosstalk cube in the simulation larger only by about $40 \times 0.001 = 0.04$ p.e. This variation is small enough compared with other sources of variations.

For the study above, 6,441 events are used. It is smaller than the required number of events for basic light yield calibration. Depending on the number of events, we divide SuperFGD into segments to check the position dependence of the crosstalk.

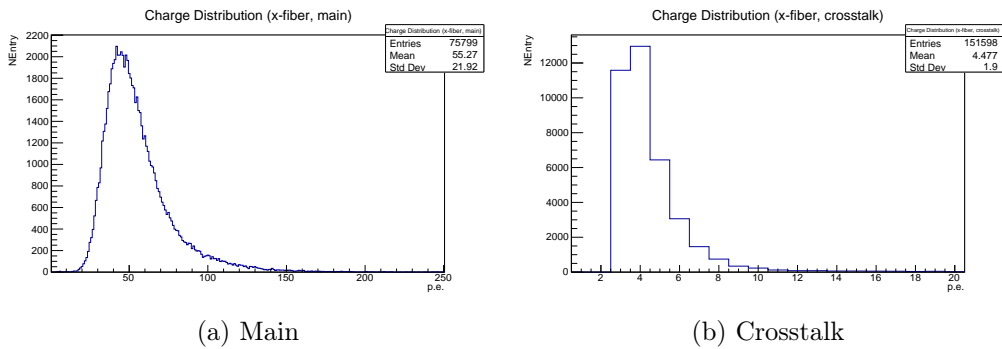


Figure 6.5. Observed light distribution of main and crosstalk channels.

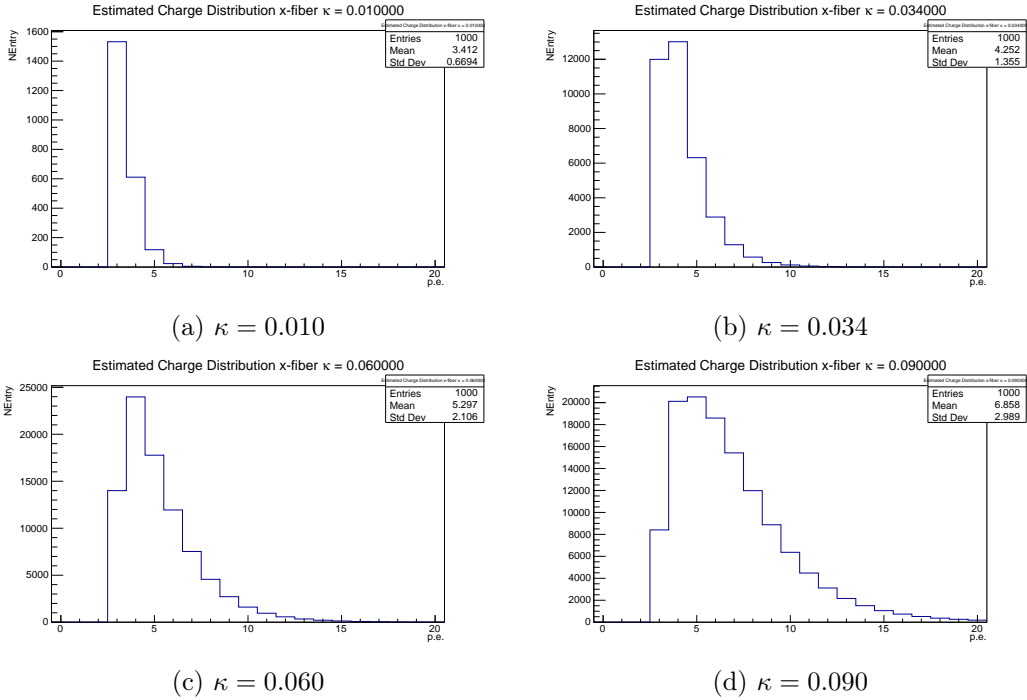


Figure 6.6. Predicted charge distributions by changing κ . $\kappa = 0.034$ is the same as what we use in the simulation.

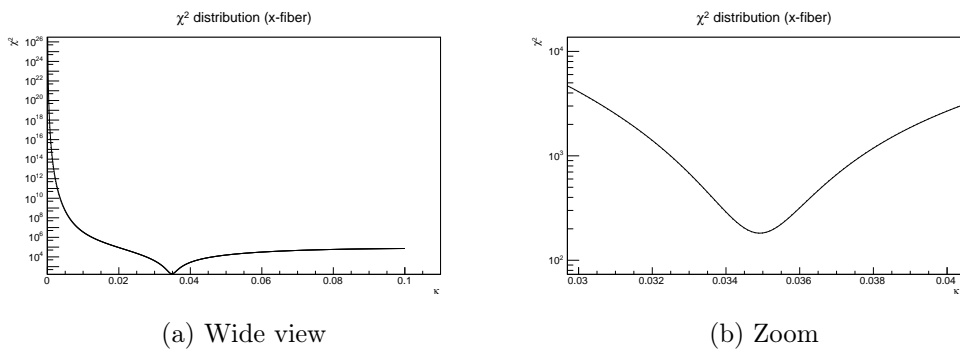


Figure 6.7. χ^2 distribution by changing κ . The number of degrees of freedom is 7.

6.3 Quenching effect

6.3.1 Empirical formula

The linearity of deposited energy dE/dX in the scintillator and light yield dL/dX becomes worse if the deposited energy is large. The empirical formula called Birks' law is

$$\frac{dL}{dX} = \frac{A}{1 + B \frac{dE}{dX}} \frac{dE}{dX}, \quad (6.3)$$

where A is the proportional constant if there is no quenching effect, and B is a parameter to describe the quenching of scintillating light (Birks' constant).

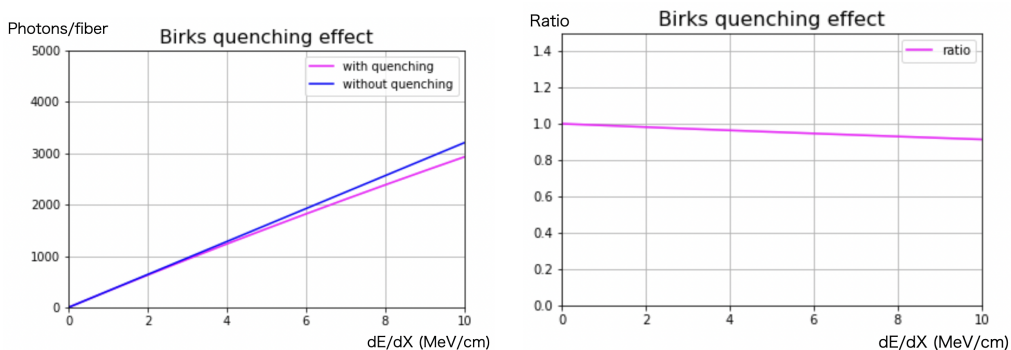
6.3.2 Estimation of the effect

In the simulation, we use $B = 0.009429$ cm/MeV. This value comes from the past measurement [35], taking the average of the plastic scintillators written in the paper and the density of the scintillator, 1.050 g/cm³. Figure 6.8 shows the quenching effect. For minimum ionizing particles, such as cosmic muons with $dE/dX \simeq 1.5$ MeV/cm, the difference between the two is about 1% and the effect is negligible.

6.3.3 Future prospects

To know the Birks' constant, we need the particle whose energy is known and which loses a large amount of energy in a cube, such as a proton beam. Two possibilities can be considered. One is performing a beam test. We place scintillator cubes in a row and inject a particle beam along the cubes. The momentum of the beam should be small enough so that the particle stops in the scintillator cubes. By comparing the data with the true information generated using the MC simulation, we estimate the effect of quenching.

Another possibility is using a proton generated in neutrino CCQE interaction in actual SuperFGD. Using the final lepton energy, momentum, angle between the initial and final leptons, and masses of particles, we can estimate the proton momentum and angle. Since the direction of the proton might not be along the cubes, the correction of light yield is difficult in this case.



(a) dE/dX and dL/dX with and without Birks quenching effect (b) Ratio of with and without Birks quenching effect

Figure 6.8. The effect of Birks quenching effect. For cosmic muons $dE/dX = 1.5$.

Chapter 7

Timing Calibration

7.1 Required precision

Required precision for the timing resolution is determined based on beam bunch separation, neutron analysis, and background rejection with ToF detectors.

Beam bunch separation The beam spill of the T2K experiment comes every 1.32 s in the run in 2023, and every 1.16 s by 2027. Each spill consists of 8 bunches and their intervals are 580 ns. We need a timing resolution better than 100 ns for each channel to distinguish the bunches.

Neutron analysis In the SuperFGD analysis, we reconstruct neutron kinetic energy using the timing difference between two vertices: the generation point of the neutron and the secondary interaction point as shown in Fig. 7.1. Ninety-nine percent of neutrons with a kinetic energy of 40 MeV, which is around the peak of the neutron energy spectrum in neutrino interaction events observed at ND280 after applying the neutron detection efficiency, travel more than 15 cm before the interaction. The time of flight of 40 MeV neutrons for 15 cm is 1.65 ns. The time resolution of the neutron generation point is neglected because it can be measured by charged tracks with a precision much better than those for the secondary interaction vertex. We require 0.82 ns time resolution of the secondary interaction vertex, which is half of the time of flight and comes from the requirement of the momentum resolution of the neutron. In this case, the energy resolution for a 15 cm flight length is 25%. Assuming we have three readouts, we need $0.82 \text{ ns} \times \sqrt{3} = 1.42 \text{ ns}$ as a time resolution of each channel.

Background rejection with ToF detectors The timing information of SuperFGD and the ToF detectors is used for rejecting the backgrounds due to particles coming from the outside of the detector. Because there are spaces between SuperFGD and TOF for HA-TPC on the top and bottom sides, it is relatively easy to distinguish the particle with the vertical direction. The horizontal distance between the SuperFGD and the ToF detector is about 10 cm. If the particle goes through 20 cm in the SuperFGD, it takes about 0.67 ns from the center of the track in the SuperFGD to the ToF detector, assuming the speed of light. The ToF detector has a 0.2 ns time resolution. To distinguish the particle coming from outside and inside at 3σ , we need $\sqrt{(0.67 \times 2/3)^2 - 0.2^2} = 0.39 \text{ ns}$

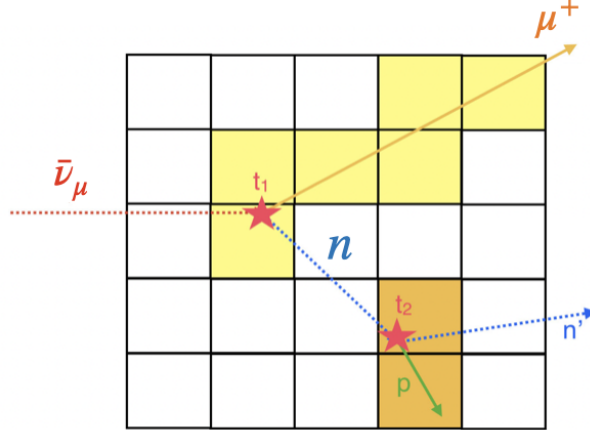


Figure 7.1. A schematic view of muon antineutrino events. The energy of the neutron is estimated using two timing, t_1 and t_2 [36].

item	required precision
Data taking	100 ns
Neutron analysis	1.42 ns
Background rejection	1.74 ns

Table 7.1. Required precision for the time resolution of each channel of SuperFGD.

as a time resolution of a track. Assuming 20 measurement points for the track, we need $0.39 \text{ ns} \times \sqrt{20} = 1.74 \text{ ns}$ as a time resolution of each channel.

7.1.1 Summary of required precision

The timing precision requirements are summarized in Table 7.1. We set 1.42 ns as a requirement for the timing resolution.

7.1.2 Source of time resolution

There are sources of time variation such as the electronics jitter, the light emission time constant (decay time) of the wavelength-shifting fiber, and cable length. We cannot eliminate the electronics' jitter and the decay time of the fiber. According to the beam test at CERN [29], the electronics' intrinsic time resolution is 0.72 ns.

As for the decay time of the fiber, lower light yields make time resolution worse. There are past measurements of the decay time of Y-11(200)M [37] [38] as shown in Table 7.2. Kuraray also reports the decay time using a small polystyrene plate with dye to be 6.9 ns [39].

Reference	decay time (ns)
[37]	7.37 ± 0.11
[38]	8.8 ± 1.5

Table 7.2. Some results for decay time measurements for Y-11.

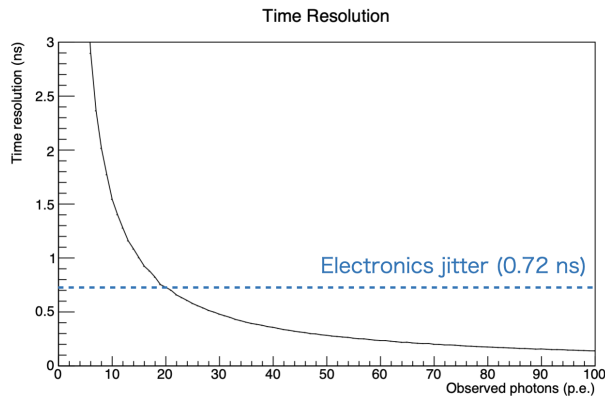


Figure 7.2. True time resolution coming from the decay time of the fiber. The time difference between 3rd photons (2.5 p.e. threshold) is considered. We assume 8 ns as a decay time.

Figure 7.2 shows the relationship between the decay time and time resolution assuming a 2.5 p.e. threshold and 8 ns for the decay time of the fiber. The standard deviation of the time distribution of the third photon reaching the MPPC is defined as the resolution. The time resolution coming from the electronics jitter (0.72 ns) is also shown.

For 40 p.e., which is around the average light yield of the minimum ionizing particle, the intrinsic time resolution σ_i from the electronics and fiber is

$$\sigma_i = \sqrt{0.72^2 + 0.36^2} \simeq 0.80 \text{ ns.} \quad (7.1)$$

Therefore we need to reduce the time variation from other sources to smaller than

$$\sqrt{1.42^2 - 0.80^2} \simeq 1.17 \text{ ns.} \quad (7.2)$$

7.2 Time offset calibration

The time origin of each channel can vary due to the difference in channels, such as cable lengths. Also, time offsets of boards can vary. We need to measure it and calibrate the time offsets.

7.2.1 Basic methods

Muon tracks are reconstructed using single fiber hits (Fig. 5.2). By correcting the propagation time in the fiber and the muon time of flight, the time that the muon passes through the top layer of the SuperFGD t_{top} is estimated from the recorded time of each single fiber hit. Only hits with more than 20 p.e. are used to avoid the effect of time-walk. The average of t_{top} is used as the reference time in an event, t_{ref} :

$$t_{\text{ref}} = \frac{\sum_{\text{single fiber hit} > 20 \text{ p.e.}} t_{\text{top}}}{\#(\text{single fiber hit} > 20 \text{ p.e.})}. \quad (7.3)$$

For each fiber with more than 20 p.e., the scintillator cube which has hits on both of two other fibers than the fiber in question and the closest to the MPPC is identified as

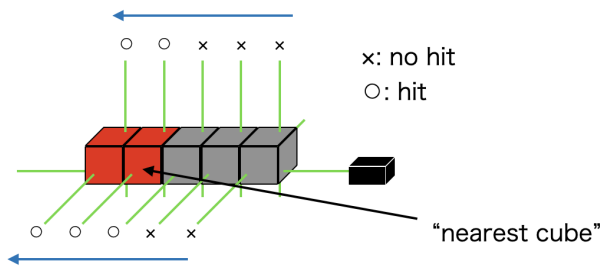


Figure 7.3. The scintillator cube which also has hits on both of two other fibers than the fiber in question and the closest to the MPPC is identified as the position of the track.

shown in Fig. 7.3. Assuming the position of this cube as the position of the muon track along the fiber, the time of flight t_{muon} and the propagation time in the fiber t_{photon} are added to t_{ref} to calculate the hit timing t_{hit} :

$$t_{\text{hit}} = t_{\text{ref}} + t_{\text{muon}} + t_{\text{photon}}. \quad (7.4)$$

The time offset of a channel is estimated from the difference between t_{hit} and the recorded time t_{record} , t_{diff} :

$$t_{\text{diff}} = t_{\text{record}} - t_{\text{hit}}. \quad (7.5)$$

Figure 7.4 shows the distribution of t_{diff} . We sum up the resulting distributions over all the fibers for each x , y , and z fibers because there are no differences between fibers in the simulation. The mean of the y fiber's distribution is smaller than that of the others. It is because the light yield of y fiber tends to be larger than the other fibers. The distributions of observed light yield are also shown in Fig. 7.4. We do not use this method for y fiber because of the bias coming from the time-walk. We calibrate y fiber simultaneously with time-walk.

7.2.2 Capability of time offset calibration

To evaluate the capability of time offset calibration, we add offsets to all channels in the simulation. The offsets are randomly determined by a Gaussian distribution with a standard deviation of 10 ns as shown in Fig. 7.5. We use 6,441 events in this study.

The t_{diff} distribution of each channel is shown in Fig. 7.6. By taking the average of t_{diff} , we calibrate the offset of each channel. Figure 7.7 shows the relationship between the input offsets and obtained offsets, and the residual distribution. The residuals are distributed around zero and its standard deviation is about 0.63 ns, so the correction is well performed.

We perform the correction one more time using the corrected time offset. The distribution of t_{diff} for the second round is shown in Fig. 7.8. Results of the second iteration are shown in Fig. 7.9. The standard deviation of the time offset distribution is changed from 0.63 ns to 0.61 ns. From this result, the second iteration is not needed. Achievable time offset variations are 0.63 and 0.62 ns for x and z fiber, respectively.

In Fig. 7.6 and Fig. 7.8, there are some events with early timing. They are due to a bug in the simulation. Sometimes the timing is a few thousand ns later in a channel. In this

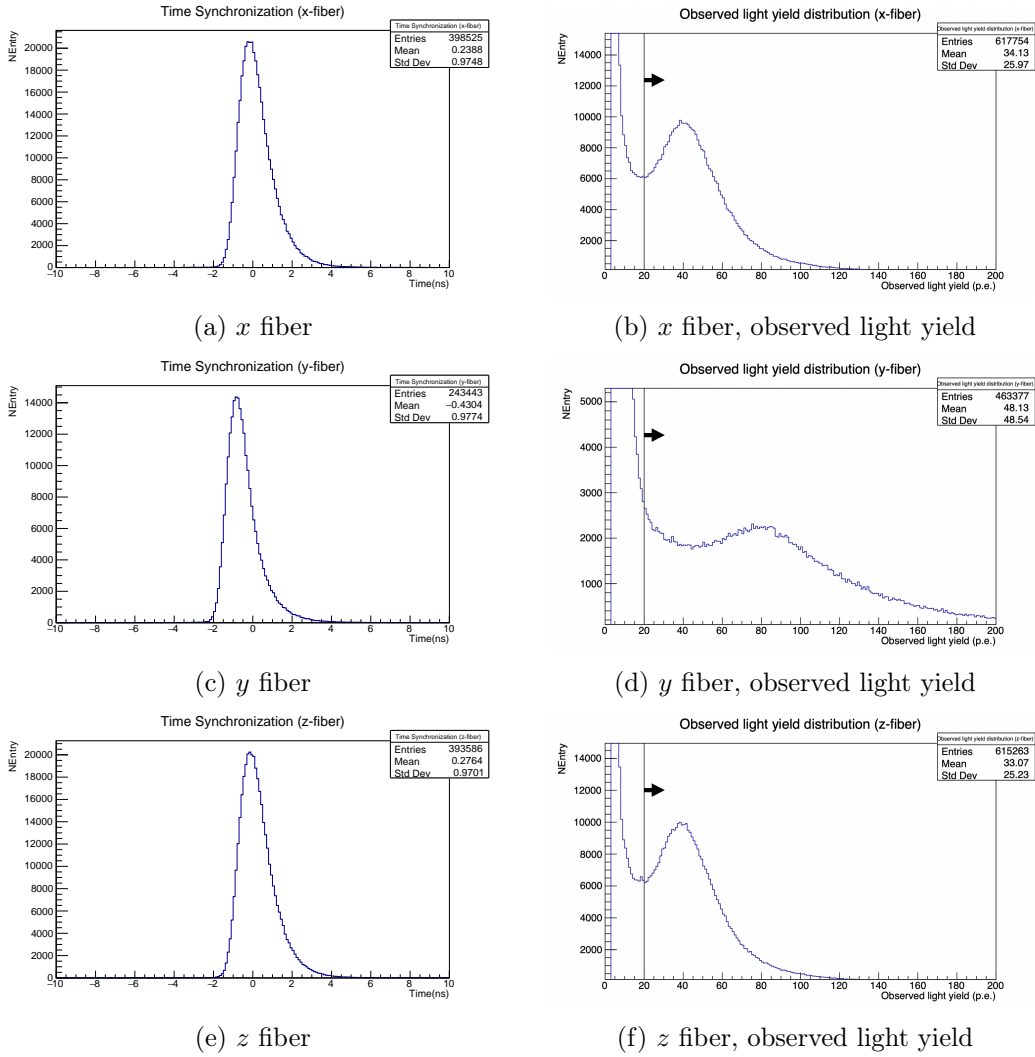


Figure 7.4. Distributions of t_{diff} (left). The distribution is asymmetry because of the time-walk effect. Distributions of observed light yield (right). Events with more than 20 p.e. are used for time offset calibration.

case, the t_{ref} is not estimated properly and the t_{diff} becomes early. However, such events are less than 1%, so we ignore them here.

Systematic uncertainties come from the propagation time in the fiber and the muon time of flight. As for the muon time of flight, we approximate the speed of muon as the speed of light. For a muon with its momentum of 1 GeV/c, the relativistic factor β is about 0.995. If the particle travels 60 cm, the time of flight is 2 ns assuming the speed of light. The difference between them is about 0.01 ns and this is negligible. For the propagation time in the fiber, we can calculate it accurately using the known refractive index of the fiber and its variation is negligible. In conclusion, the systematic uncertainty is small enough and ignore here.

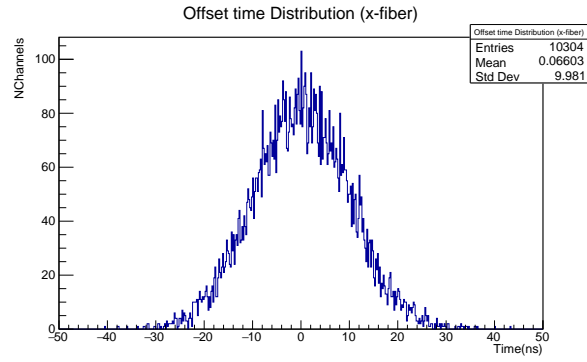


Figure 7.5. Input offset distribution of x fibers.

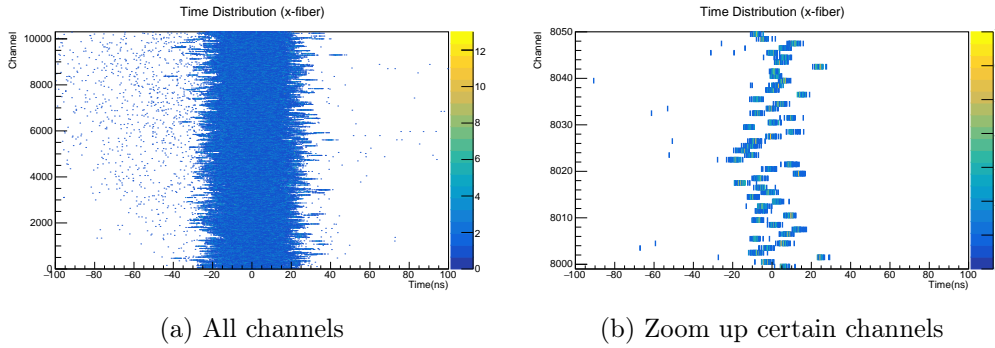


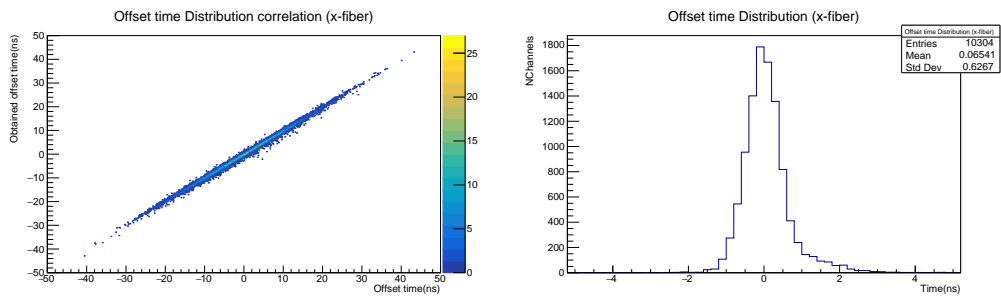
Figure 7.6. t_{diff} distribution of each channel (x fiber, before correction).

Assuming one-day cosmic data, we achieve the time offset variations $\sigma_{o,x}$ and $\sigma_{o,z}$ as:

$$\sigma_{o,x} = 0.63 \times \sqrt{\frac{6441}{864000}} = 0.054 \text{ ns} \quad (7.6)$$

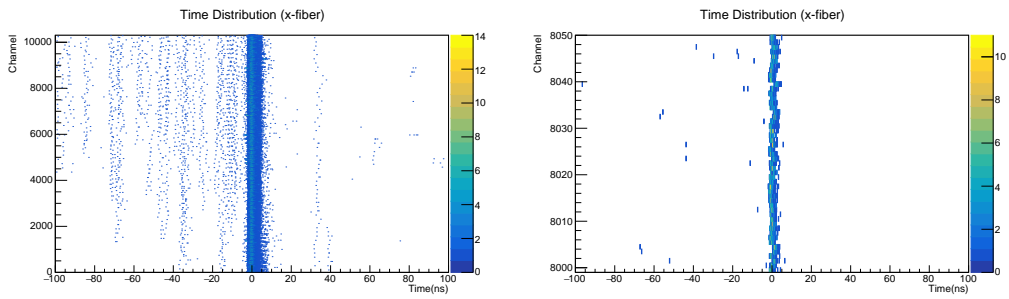
$$\sigma_{o,z} = 0.62 \times \sqrt{\frac{6441}{864000}} = 0.054 \text{ ns} \quad (7.7)$$

for x and z fibers.



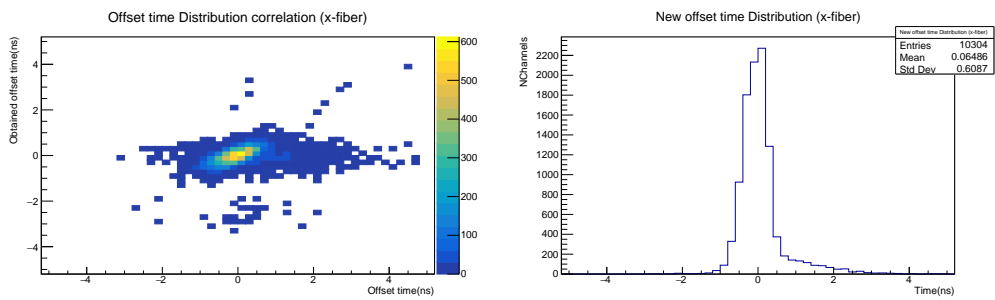
(a) Input offsets and obtained offsets (b) Corrected offset distribution of x fibers

Figure 7.7. Result of the first iteration.



(a) All channels (b) Zoom up certain channels

Figure 7.8. t_{diff} distribution of each channel (x fiber, after correction).



(a) Obtained offsets relationship between the first and second iteration (b) distribution of corrected offsets after the second iteration for x fibers

Figure 7.9. Result of the second iteration.

7.3 Time-walk correction

7.3.1 Fiber time-walk

The fiber time-walk can be modeled using an analytical function. Considering the threshold n , we need to know the probability that $n-1$ photons are already observed. This probability can be written as:

$$P = C \cdot \exp\left(\frac{-t(N-n+1)}{\tau_f}\right) \left(1 - \exp\left(\frac{-t}{\tau}\right)\right)^{(n-1)}, \quad (7.8)$$

where C is the normalization constant. N is the observed photons and τ_f is the decay time of the fiber. We want to know the average time of n -th photon detection.

$$\langle t \rangle = \frac{\int_0^\infty tP dt}{\int_0^\infty P dt}. \quad (7.9)$$

In the case of $n = 3$, the average time can be written as:

$$\langle t \rangle = \frac{3N^2 - 6N + 2}{N(N-1)(N-2)}\tau. \quad (7.10)$$

Figure 7.10 shows the correction function of the fiber time-walk. Here, we assume $\tau = 12$ ns based on the measurement of existing detectors at ND280 [11], and this value is used in the simulation. In the actual calibration, we should obtain the decay time of the wavelength-shifting fiber by external measurement or using actual SuperFGD.

7.3.2 MPPC-Electronics time-walk

The other source of the time-walk effect is coming from the threshold of electronics and pulse height. Assuming a simple exponential rise of the waveform, the timing passing the threshold depends on the pulse height as shown in Fig. 7.11. The threshold charge Q_{th} is written as:

$$Q_{th} = Q_0 \left(1 - \exp\left(-\frac{t_{th}}{\tau_e}\right)\right), \quad (7.11)$$

where Q_0 is the pulse height, and τ_e is the rising time. t_{th} is the timing passing the threshold:

$$t_{th} = -\tau \times \ln\left(1 - \frac{Q_{th}}{Q_0}\right). \quad (7.12)$$

Figure 7.12 shows the correction function of the MPPC-electronics time-walk. Here, we assume a simple exponential rise but the actual waveform goes down with time so this assumption is not good.

7.3.3 Methods for time-walk correction

We have two sources of the time-walk effect but we cannot completely separate them. We use one function to correct the time-walk effect.

The method to estimate the reference time in an event t_{ref} and the time difference t_{diff} is the same as for time offset calibration. However, we use events not only with more than 20 p.e. but also less than 20 p.e. for time-walk correction. In the case that the timing

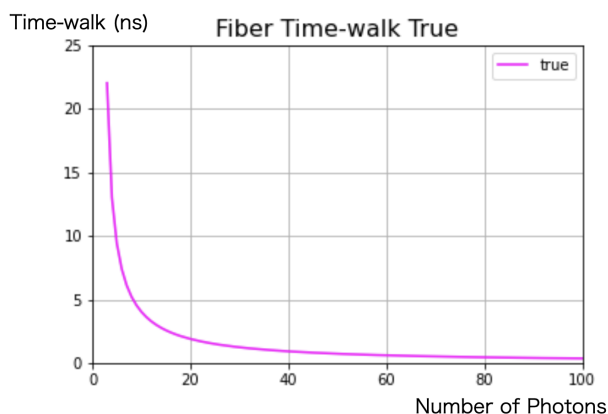


Figure 7.10. Fiber time-walk. We need to subtract time from the observed time according to this function.

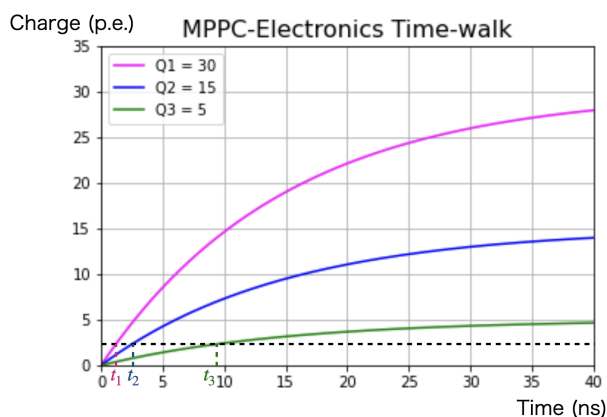


Figure 7.11. Charges as a function of time assuming simple exponential rise. The threshold is 2.5 p.e.

of each channel is completely synchronized, the relationship between the timing and the observed photons is shown in Fig. 7.13. Here, we sum up all the x fibers to increase the number of events. By taking the average of t_{diff} in certain regions of observed light yield, we know the relationship between the observed number of photons and timing, as shown in Fig. 7.14. We take the average over every 5 p.e. from 5 to 20 p.e., every 10 p.e. from 20 to 50 p.e., and every 20 p.e. from 50 to 150 p.e. We fit the average time with the function

$$t = t_0 + \frac{a}{q + b}, \quad (7.13)$$

where t and q are the timing and number of photons, respectively. t_0 , a , and b are the fitting parameters. t_0 corresponds to the timing of an infinite number of photons (no time-walk effect). t_0 should be the same for all the directions because we have no time offset here. Based on the fit results, they are consistent within 0.3 ns, even for y fibers. We use this method for the time synchronization of y fibers.

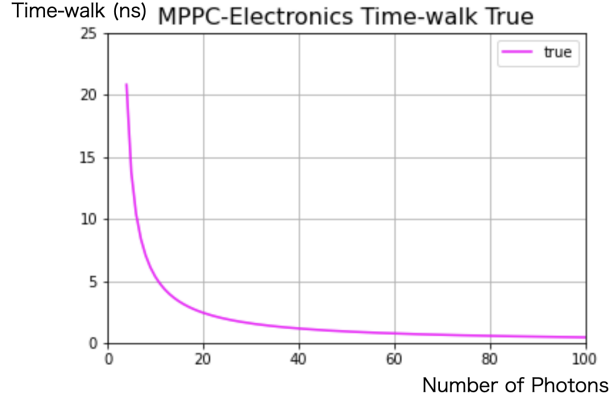


Figure 7.12. MPPC-electronics time-walk. We need to subtract time from the observed time according to this distribution.

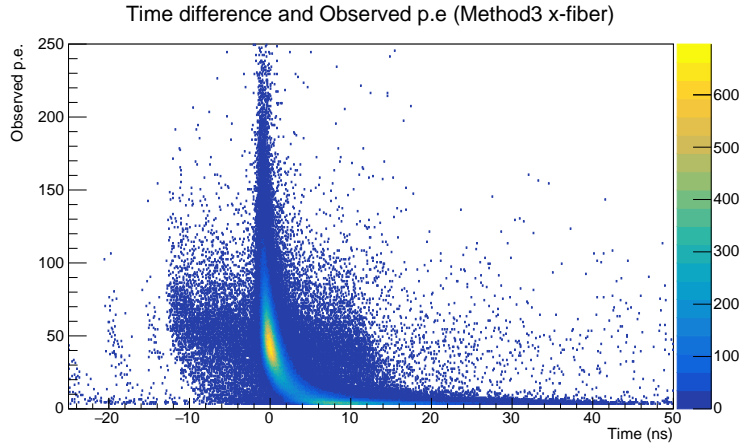


Figure 7.13. Timing and observed number of photons (x fiber).

7.3.4 Capability of time-walk correction and time synchronization

We sum up all the fibers above. As shown in Fig. 7.14, fitting errors of t_0 are 0.007 ns for y fiber. Since there are about 40,000 y fibers and assuming one-day cosmic data, the achievable time offset variation for y fiber $\sigma_{o,y}$ is

$$\sigma_{o,y} = 0.007 \times \sqrt{40000} \times \sqrt{\frac{6441}{864000}} = 0.12 \text{ ns}. \quad (7.14)$$

For the time-walk correction, Fig. 7.15 shows the average t_{diff} with respect to the observed light yield and 1σ confidence interval. We have a 0.25 ns deviation at most between the plot point and fitting function. We assume that this variation remains if the number of events increases and assume 0.25 ns as a systematic uncertainty. Above 40 p.e., the maximum widths of the confidence interval are 0.0055, 0.0044, and 0.0045 ns for x , y , and z fiber, respectively. Since we sum up about 10,000 fibers for horizontal fibers and about 40,000 fibers for vertical fibers and assume one-day cosmic data, the achievable

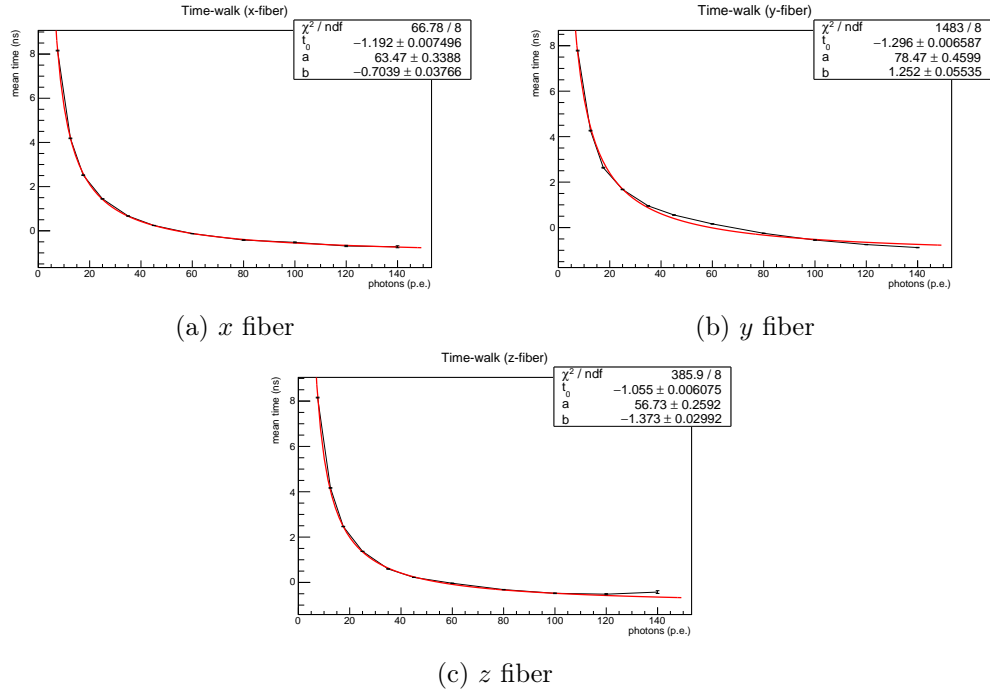


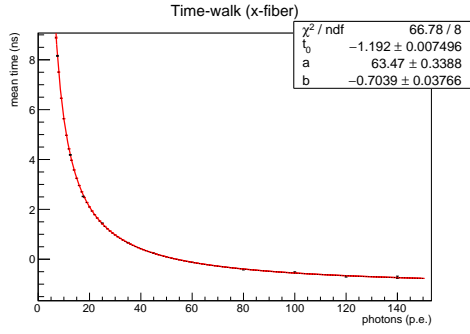
Figure 7.14. Average t_{diff} with respect to the observed light yield.

statistical uncertainties related to the time-walk correction are 0.047, 0.076, and 0.039 ns, respectively. By taking the sum of statistical and systematic uncertainties, we estimate achievable uncertainties related to the time-walk correction $\sigma_{w,x}$, $\sigma_{w,y}$, and $\sigma_{w,z}$ to be:

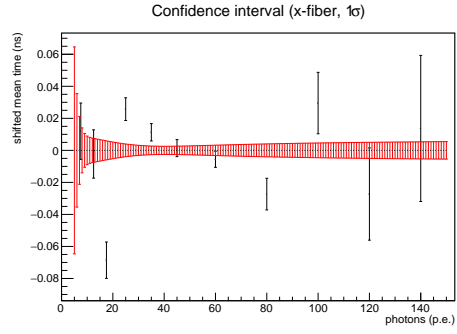
$$\sigma_{w,x} = 0.30 \text{ ns} \quad (7.15)$$

$$\sigma_{w,y} = 0.33 \text{ ns} \quad (7.16)$$

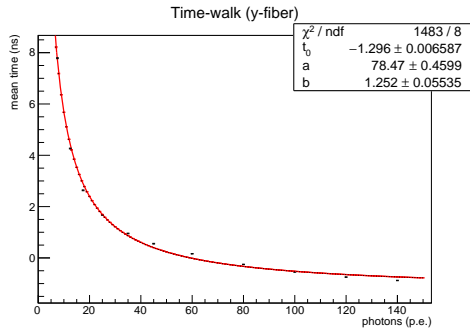
$$\sigma_{w,z} = 0.29 \text{ ns}. \quad (7.17)$$



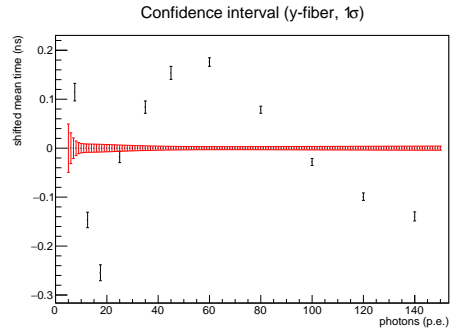
(a) x fiber



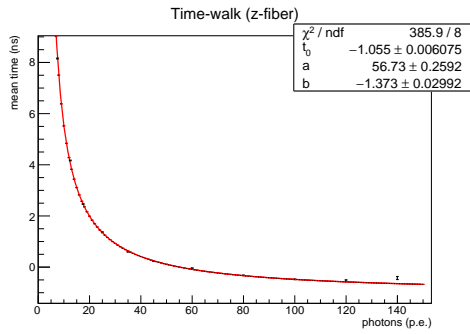
(b) x fiber, shifted



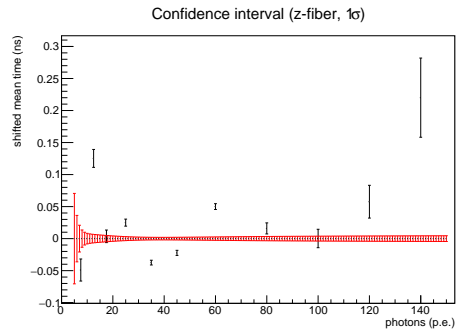
(c) y fiber



(d) y fiber, shifted



(e) z fiber



(f) z fiber, shifted

Figure 7.15. Average t_{diff} with respect to the observed light yield together with 1σ confidence interval. The right figures are the average time shifted by the fit curve. 6,441 events are used and all the channels are summed up.

7.4 Expected precision of timing calibration

The uncertainties related to the time offset calibration and time-walk correction are summarized in Table 7.3. We assume cosmic data for one day. They are within the requirement of 1.17 ns.

Direction	time offset	time-walk	total
<i>x</i> fiber	0.054 ns	0.30 ns	0.30 ns
<i>y</i> fiber	0.12 ns	0.33 ns	0.35 ns
<i>z</i> fiber	0.054 ns	0.29 ns	0.29 ns

Table 7.3. Uncertainties related to time offset calibration and time-walk correction assuming cosmic data of one day.

Chapter 8

Measurement of new wavelength-shifting fiber products with short decay time

In addition to developing calibration methods for SuperFGD, we measure new types of wavelength-shifting fibers for possible use in future detectors. As mentioned in Chap. 7, the decay time of the wavelength-shifting fiber is a non-negligible source of the time resolution, especially if the observed number of photons is small. For SuperFGD, the electronics jitter is the primary source of timing uncertainty for larger light yield. However, it can be improved for a future detector. For smaller light yield and future detectors using wavelength-shifting fiber, the scintillation decay time of the fiber becomes the main source of the time resolution.

Recently, Kuraray produced some new types of wavelength-shifting fibers, called the YS series [39]. According to the company, the key feature of these fibers is their short decay time. We report the measurement of the decay time of these fibers.

8.1 Experimental setup

A schematic layout of the decay time measurement is shown in Fig. 8.1. Laser light whose

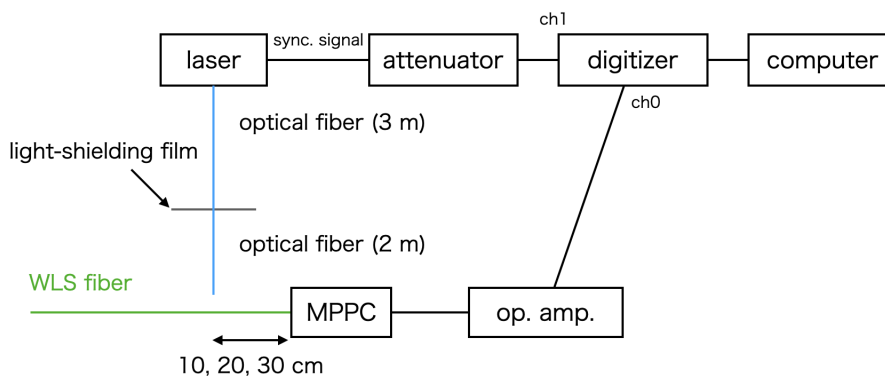


Figure 8.1. Schematic layout of the decay time measurement.



Figure 8.2. Picture of the dark box.

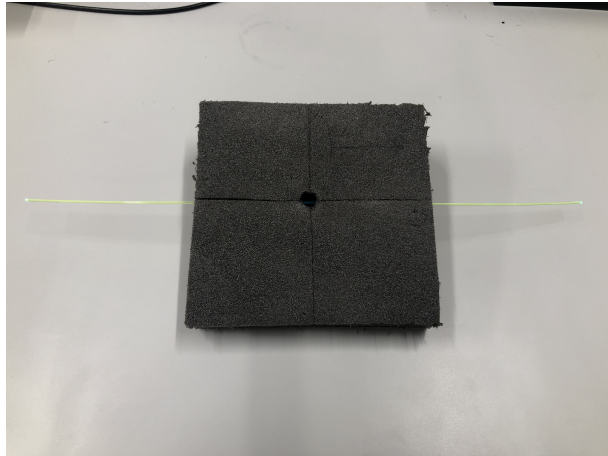


Figure 8.3. Jig for injecting laser into the fiber (hard foam).

intensity is reduced to the single photon level is injected into the wavelength-shifting fiber by changing the distance between MPPC and the position of the injection of laser, to 10 cm, 20 cm, and 30 cm. The frequency of the laser is 10 kHz and we take each data for about two minutes.

8.1.1 Dark box and jigs

We make a dark box for the measurement of fibers. The picture of the dark box is shown in Fig. 8.2. The dark box consists of black anodized aluminum frames and panels. The length of the box is 3.5 m so that the 3 m fiber can be put without bending. Light tightness is checked by comparing the counting rates of an MPPC in the dark box with turning the room light on and off. We confirm the count rates are not changed.

Figure 8.3 shows the jig we use to inject light into the fiber. It is made of hard foam, and a connector of optical fiber is attached at the center of the jig. Inside the dark box, we have two frames on which hard foams are fixed as shown in Fig. 8.4.



Figure 8.4. Inside the dark box. Two frames run in the center to put the jigs.



Figure 8.5. Laser PLP-10 (C10196, M10306-30).

8.1.2 Laser

We use PLP-10 (C10196, M10306-30) produced by Hamamatsu Photonics K.K. shown in Fig. 8.5. The wavelength of the laser is 405 nm. This wavelength is within the absorption peak of each wavelength-shifting fiber. There are TTL and NIM outputs synchronized with the laser pulse. We can control the intensity but not down to the single photon level. The laser pulses are transferred by optical fibers with FC connectors.

8.1.3 MPPC and circuit

We use an MPPC S13081-050CS with a sensitive area of $1.3 \text{ mm} \times 1.3 \text{ mm}$ and a pixel pitch of $50 \mu\text{m}$. Figure 8.6 shows the diagram of the MPPC readout circuit. We have five input and output connectors. One is used for applying the bias voltage to MPPC and another is used to read the signal. Two connectors are used to supply voltages to the operational amplifier AD8033 [40]. For debugging purposes, we have one more input

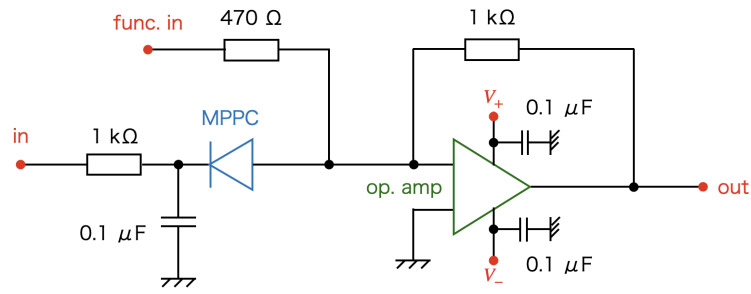


Figure 8.6. Diagram of readout circuit.



Figure 8.7. Digitizer DT5730.

to check the function of the operational amplifier by injecting a signal from a function generator.

8.1.4 Digitizer

We use CAEN DT5730 (Fig. 8.7) a 14-bit, 500 MS/s 8-channel digitizer to record the signal waveform. We record the MPPC output and the synchronized signal with the laser. All the waveforms triggered with the synchronized signal are recorded for analysis.

8.1.5 Wavelength-shifting fiber

We have four types of wavelength-shifting fibers, Y-11, YS-2, YS-4, and YS-6. We measure five fibers of Y-11 and one fiber each of YS-2, 4, and 6. The length of each fiber is about 3 m. The edges of the fibers are blackened to reduce the reflection.

8.1.6 Light-shielding films

The direct light from the laser is at a level of a few tens of photons. We use light-shielding films to reduce the intensity to the single photon level. We have two types of films. The

item	film1	film2
type	clear	smoak
transmittance (sunlight)	24%	15%
absorption (sunlight)	39%	80%
transmittance (UV light)	33%	3%

Table 8.1. Transmission rate of two light-shielding films.



Figure 8.8. Cut film placed in the connector.

difference between the two is the transmittance of the light as listed in Table 8.1. We cut the film into a piece of about $2 \text{ mm} \times 2 \text{ mm}$ and put it into the connecting adopter of optical fibers as shown in Fig. 8.8.

8.2 Analysis method

8.2.1 Waveform and timing determination

An example of the waveform is shown in Fig. 8.9. The figure also shows how to estimate the timing. The pedestal is calculated using the first 100 points (200 ns). The timing of the pulse is defined as the point at which the signal height is half the height of the peak in the falling edge. Ten points around half the peak height of the pulse are fit with a linear function to define the timing.

The number of photons of each event is estimated by two methods: the pulse height and the integrated ADC value below the pedestal.

8.2.2 Event selection

To select single photon events, we check the signal height and integrated ADC distribution shown in Fig. 8.10. This example is the case of Y-11 with the distance between the MPPC and laser injection point of 10 cm. The mean light intensity is about 2 p.e. The red rectangular region in Fig. 8.10 is defined to include all bins whose number of events is

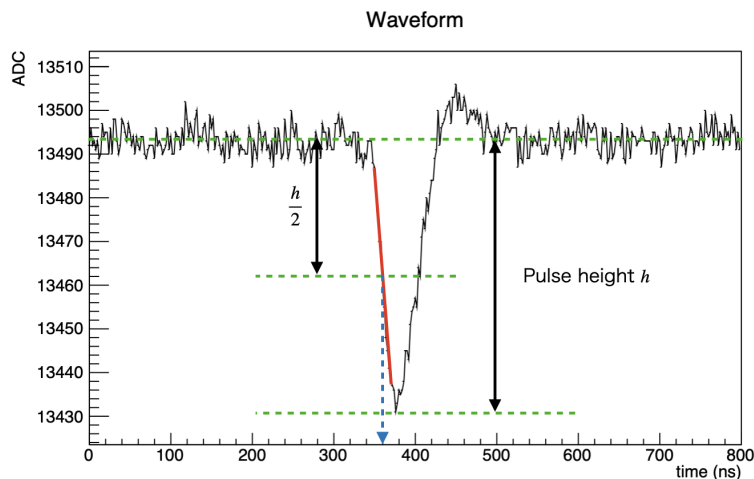


Figure 8.9. Waveform of single photon event.

more than 10% compared to the bin of single photon peak. We use events inside the red rectangular region as single photon events.

We need to reject events that have hits in the region we calculate the pedestal. If the difference between the minimum and maximum ADC in the region is more than 30 ADC counts, the event is rejected. By this selection, 3.8% of events are rejected.

8.2.3 Fitting function

The fitting function is the convolution function of an exponential decay $f(t)$ and normalized Gaussian distribution $g(t)$:

$$f(t) = \begin{cases} 0 & (t < t_0) \\ A \exp\left(-\frac{t-t_0}{\tau}\right) & (t > t_0) \end{cases} \quad (8.1)$$

$$g(t) = \frac{1}{\sqrt{2\pi}\sigma} \exp\left(-\frac{t^2}{2\sigma^2}\right) \quad (8.2)$$

$$f(t) * g(t) = C \left\{ 1 + \operatorname{erf}\left(\frac{t-t_0-\frac{\sigma^2}{\tau}}{\sqrt{2}\sigma}\right) \right\} \cdot \exp\left(-\frac{t-t_0}{\tau}\right), \quad (8.3)$$

where C is the normalization factor, t_0 is the start time of the decay including the delay of the signal, and t is the time difference between the laser and MPPC signal. σ is the time resolution for a single photon signal and τ is the decay time of the fiber. Because we have an accidental coincidence between the timing of the laser and the dark noise of MPPC, we need a constant background. We obtain the fitting function as:

$$N(t) = C \left\{ 1 + \operatorname{erf}\left(\frac{t-t_0-\frac{\sigma^2}{\tau}}{\sqrt{2}\sigma}\right) \right\} \cdot \exp\left(-\frac{t-t_0}{\tau}\right) + \text{const.} \quad (8.4)$$

8.2.4 Single photon time resolution

In order to evaluate the time resolution of the measurement system, we inject the laser into the MPPC without a wavelength-shifting fiber. Figure 8.11 shows the result of time

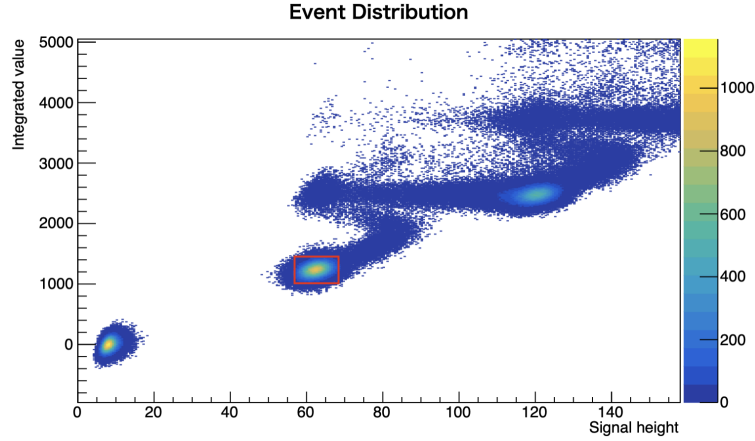


Figure 8.10. Signal height and integrated ADC distribution. We use events inside the red rectangular region as single photon events.

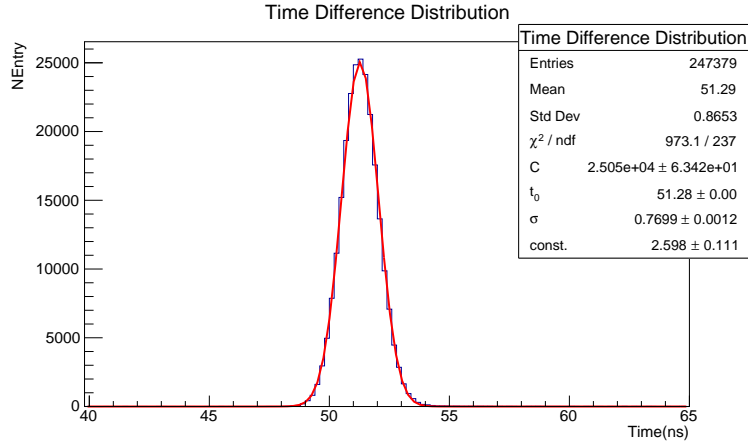


Figure 8.11. Time resolution of our setup.

resolution measurement. The fitting function is the sum of a Gaussian and a constant background:

$$N(t) = C \times \exp \left\{ -\frac{(t - t_0)^2}{2\sigma^2} \right\} + \text{const.} \quad (8.5)$$

The time resolution of our setup is about 0.77 ns.

8.3 Results and discussions

Examples of time distribution and fit results are shown in Fig. 8.12. The results are summarized in Table 8.2. We estimate the systematic uncertainty of the measurement from the measurement of five Y-11 fibers. We assume they have the same decay time. By taking the difference between the maximum and minimum average values of five Y-11 fibers, we assign the systematic uncertainty of 0.065 ns.

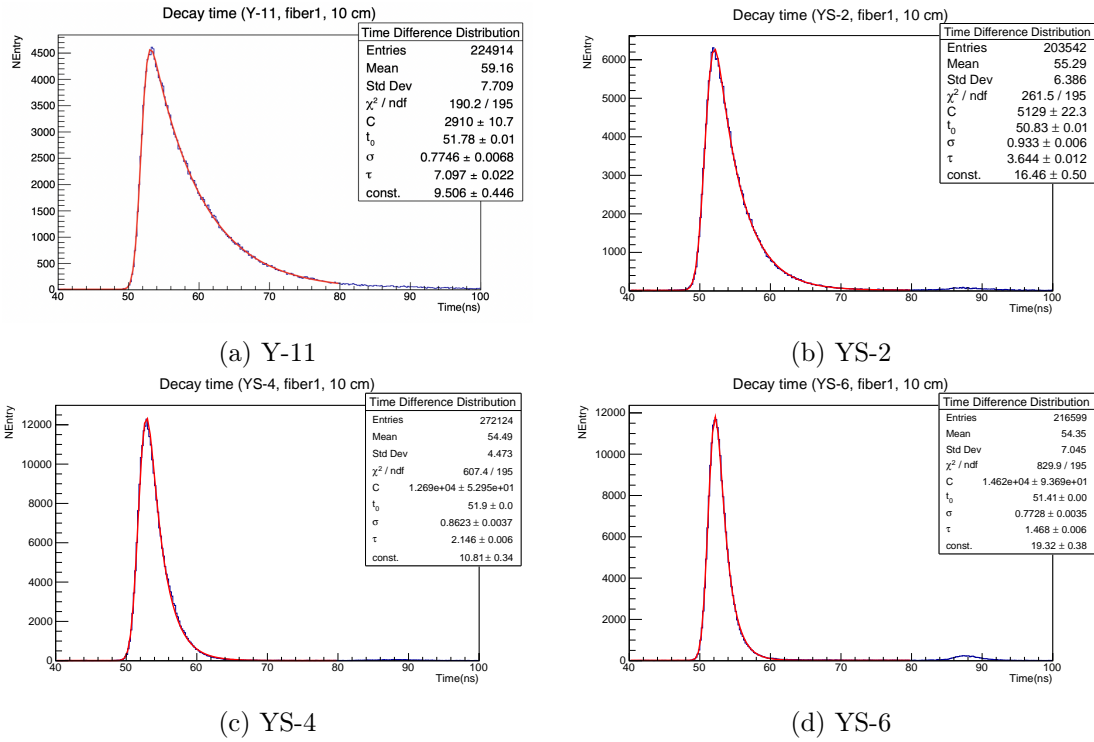


Figure 8.12. Examples of time distributions and fit results. The position of injecting laser is 10 cm from the MPPC. The fitting range is below 80 p.e. to avoid the effect of the reflection seen around 87 ns.

The decay time τ of each fiber is summarized in Table 8.3. The table also shows the decay time measured by another group using plastic sheets instead of fibers as reference values [41]. In the past measurement, synchrotron radiations were injected into the thin films of the plastic scintillator used for the wavelength-shifting fibers and reemitted light was detected with a PMT. Our results are larger than the results of the past measurement. The differences between the two measurements are the wavelength of injected light, the path length in the plastic (fiber), and the shape, summarized in Table 8.4. In the past measurement, the wavelength was from 418 to 460 nm. In our measurement, the wavelength of the laser is 405 nm. This difference changes the efficiency of the absorption of light. It can change the decay time if the excited states are different. The path length in the fiber can change the decay time. The self-reabsorption of photons by the fiber occurs if the path length is large because absorption and emission spectra overlap. We estimate the effect of self-reabsorption by extrapolating the decay time to 0 cm using the data with 10, 20, and 30 cm because the plastic used in the past measurement is thin. However, even if considering this effect, the decay time changes up to 0.1 ns. The results of our measurement are still larger than the results of the past measurement. The shapes are also different but it is unlikely to affect the decay time. Table 8.3 also shows the decay times of Y-11 and YS-2 measured by another group. The method of measurement is similar to ours. The result is consistent within a few σ .

Type	number	10 cm (ns)	20 cm (ns)	30 cm (ns)	average (ns)
Y-11	fiber1	7.097 ± 0.022	7.168 ± 0.023	7.231 ± 0.024	7.165 ± 0.023
	fiber2	7.155 ± 0.030	7.126 ± 0.024	7.239 ± 0.025	7.173 ± 0.026
	fiber3	7.022 ± 0.022	7.119 ± 0.022	7.202 ± 0.023	7.114 ± 0.022
	fiber4	7.125 ± 0.023	7.152 ± 0.024	7.259 ± 0.024	7.179 ± 0.024
	fiber5	7.098 ± 0.023	7.177 ± 0.024	7.222 ± 0.024	7.166 ± 0.024
YS-2	fiber1	3.644 ± 0.012	3.71 ± 0.01	3.732 ± 0.012	3.695 ± 0.011
YS-4	fiber1	2.146 ± 0.006	1.919 ± 0.006	2.125 ± 0.022	2.063 ± 0.014
YS-6	fiber1	1.468 ± 0.006	1.509 ± 0.006	1.53 ± 0.01	1.502 ± 0.008

Table 8.2. Results of decay time measurements. The position of injecting laser from MPPC is 10, 20, and 30 cm. Only statistical errors are shown.

type	reference value 1	reference value 2	obtained value
Y-11	6.44 ns	7.37 ± 0.11 ns	7.159 ± 0.024 (stat.) ± 0.065 (syst.) ns
YS-2	3.16 ns	3.99 ± 0.03 ns	3.695 ± 0.011 (stat.) ± 0.065 (syst.) ns
YS-4	1.37 ns		2.063 ± 0.014 (stat.) ± 0.065 (syst.) ns
YS-6	1.27 ns		1.502 ± 0.008 (stat.) ± 0.065 (syst.) ns

Table 8.3. Summary of decay times. Reference values 1 are obtained using pieces of plastic [41]. Reference values 2 are obtained using fibers [37].

item	past measurement [41]	our measurement
wavelength of injection light	418 to 460 nm	405 nm
path length in fiber	1 mm	10 to 30 cm
shape	5 mm \times 5 mm	1 mm round shape

Table 8.4. Different conditions of reference measurement and our measurement.

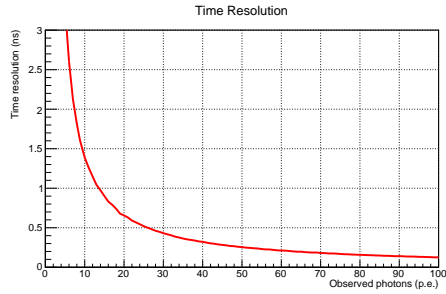
8.4 Possible improvement of neutron measurement

We consider the improvement of neutron measurement with new fibers. Figure 8.13 shows the relationship between the decay time and time resolution assuming a 2.5 p.e. threshold with various decay times.

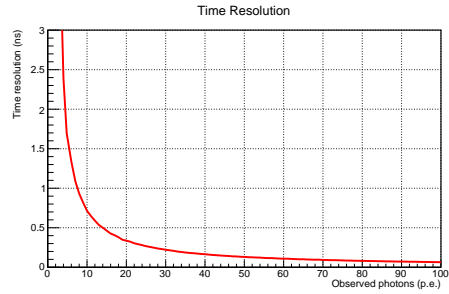
For neutron detection in SuperFGD, we use channels with 40 or more p.e. to assure sufficient timing resolution [36]. This 40 p.e. corresponds to about 22, 12, and 10 p.e. for YS-2, 4, and 6, respectively, for the same time resolution. Figure 8.14 shows the distribution of the observed light yield from neutron interaction. The numbers of readouts with more than 40, 22, 12, and 10 p.e. are summarized in Table 8.5. The table also shows the number of events whose largest light yield is more than 40, 22, 12, and 10 p.e. If we have a light yield with 40 p.e. or more, we detect the neutron using Y-11. The efficiency of neutron detection becomes 1.2 times larger using YS-6 compared to Y-11. Because we have a 3 times larger number of readouts for YS-6 compared to Y-11, the time resolution becomes $\sqrt{3}$ times better if the light yield is the same for both fibers, assuming the difference of time resolution above the detection threshold is negligible. The energy reconstruction of neutrons is improved.

threshold (p.e.)	all	largest
40	1362	754
22	2221	874
12	3576	925
10	4094	932
total	8647	1000

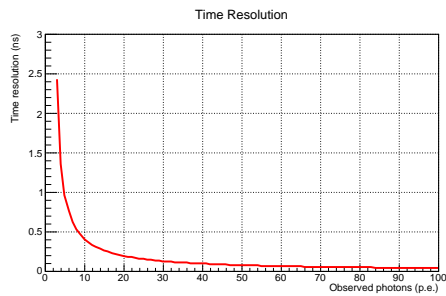
Table 8.5. Numbers of readouts with more than 40, 22, 12, and 10 p.e.



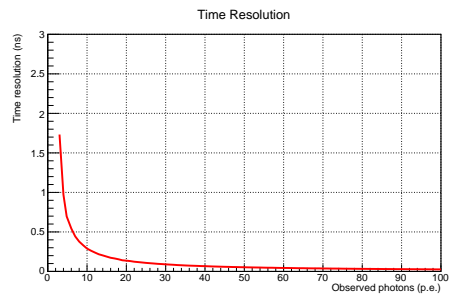
(a) decay time 7.2 ns (Y-11)



(b) decay time 3.7 ns (YS-2)

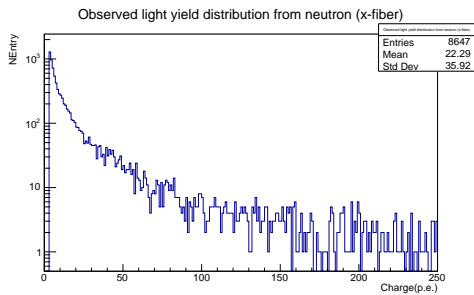


(c) decay time 2.1 ns (YS-4)

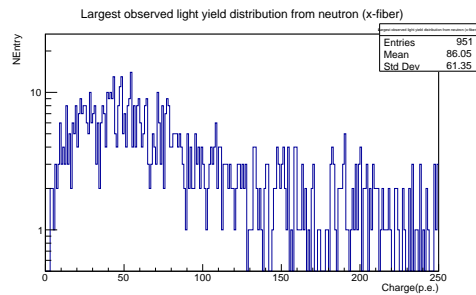


(d) decay time 1.5 ns (YS-6)

Figure 8.13. Time resolution coming from the decay time of the fiber assuming 2.5 p.e. threshold. We assume 7.2, 3.7, 2.1, and 1.5 ns as decay times.



(a) All light yields



(b) Largest light yields

Figure 8.14. Observed p.e. from neutron simulation in SuperFGD. The left figure shows all light yields. The right figure shows the largest light yields in one event.

Chapter 9

Summary and Conclusion

The T2K (Tokai to Kamioka) experiment is a long baseline neutrino oscillation experiment in Japan. The goal of the T2K experiment is the observation and precise study of CP violation in the lepton sector. Until now, T2K excludes the conservation of CP symmetry in neutrino oscillation at the 2σ level for both mass ordering. To achieve higher precision, we are upgrading each component and are about to start the T2K-II phase.

To reduce systematic uncertainties related to the limitation of the current near detectors, we are working on upgrading the near detector. We install a new target detector: SuperFGD (Super Fine Grained Detector). To extract its performance, calibration is necessary. We report the development of the calibration method for fiber, scintillator, and timing in this thesis. The requirement for light yield uniformity is 8.1% assuming the resolution of the momentum of a particle. Table 9.1 shows the achievable light yield uniformity of each channel using one-day cosmic data, assuming 10 Hz. They are within the requirement.

direction	light yield uniformity (%)
requirement	8.1
x fiber	3.6
y fiber	4.5
z fiber	2.7

Table 9.1. Achievable energy resolution of each channel using one-day cosmic data.

We also need to measure the crosstalk rate and quenching effect of the scintillator. For the crosstalk, we develop a method to measure it. For the quenching effect, we need to measure the Birks' constant by a beam test or actual interaction in SuperFGD.

As for timing calibration, we need a 1.17 ns time resolution without intrinsic time resolution for 40 p.e., which is around the light yield from MIP, considering the neutron analysis. Table 9.2 shows the expected precision of timing calibration using one-day cosmic data, assuming 10 Hz. They are within the requirement.

In addition to the development of calibration methods for SuperFGD, we report the measurement of the new type of wavelength-shifting fibers. Their key feature is short decay

direction	time resolution (ns)
requirement	1.17
x fiber	0.30
y fiber	0.35
z fiber	0.29

Table 9.2. Expected precision of timing calibration using one-day cosmic data.

time. We measure the decay time of those fibers. The results are

$$\tau(\text{Y-11}) = 7.159 \pm 0.024 \text{ (stat.)} \pm 0.065 \text{ (syst.)}$$

$$\tau(\text{YS-2}) = 3.695 \pm 0.011 \text{ (stat.)} \pm 0.065 \text{ (syst.)}$$

$$\tau(\text{YS-4}) = 2.063 \pm 0.014 \text{ (stat.)} \pm 0.065 \text{ (syst.)}$$

$$\tau(\text{YS-6}) = 1.502 \pm 0.008 \text{ (stat.)} \pm 0.065 \text{ (syst.)}.$$

We confirm that the decay time of the YS series is shorter than that of Y-11.

Acknowledgments

I would like to my heartfelt thanks to my supervisor, Prof. M. Yokoyama for giving me a special opportunity to conduct my research. I also would like to thank Prof. Y. Nakajima and Prof. K. Nakagiri for their support during my master's course and helpful advice. I want to express my appreciation to the members of the Yokoyama-Nakajima group: Eguchi-san, Yoshimi, Li-Cheng, Shima-san, Okinaga-kun, Kobayashi-kun, Watanabe-kun, and Kono-san. The discussion with all the people in the Yokoyama-Nakajima group was fruitful.

I am grateful to the members of the ND280 calibration group: P. Jonsson, M. Lawe, T. Matsubara, C. Lin, J. McKean, Arihara-san, Koto-kun, and Furui-kun. I am also grateful to the members of the SuperFGD simulation and reconstruction group: C. McGrew and D. Sgalaberna. It was very helpful to discuss with them the simulation and calibration methods.

I would like to thank KURARAY for their offer of the new types of wavelength-shifting fibers.

Finally, I would like to express my greatest appreciation to my family for their consideration and encouragement.

List of Figures

1.1	Cross-section of neutrino-nucleus interactions for neutrino mode [1]. The shape of the expected neutrino beam flux in T2K is shown with the shaded area.	8
1.2	A diagram of CCQE [1].	8
1.3	A diagram of CC RES pion production [1].	9
1.4	A diagram of CC DIS [1].	9
2.1	Overview of the T2K experiment.	11
2.2	Overview of the T2K neutrino beamline [7].	12
2.3	Side view of the secondary beamline [7].	13
2.4	Muon neutrino survival probability at 295 km and neutrino fluxes for different off-axis angles [9].	14
2.5	The current ND280 [10].	15
2.6	One sub-module structure of FGD [12].	15
2.7	$\Delta\chi^2$ and obtained 3σ Feldman-Cousins (FC) confidence intervals [13].	16
2.8	Reconstructed momentum and angle for muons selected at ND280 (left) and electrons selected at SK (right) [14].	17
2.9	Schematic view of the upgraded ND280 [15].	19
2.10	Schematic view of the HA-TPC [14].	19
2.11	Schematic layout of the ToF detector planes [14].	20
2.12	Measured time resolution with MPPC at both ends of a 2.3 m long bar as a function of the beam impact position along the bar [14].	21
3.1	Schematic view of the SuperFGD. The number of cubes is reduced for ease of viewing. The size of each cube is $1 \times 1 \times 1 \text{ cm}^3$. The number of readout channels is 55,888 [14].	23
3.2	Cross-section and cladding thickness of wavelength-shifting fiber Y-11 [18].	23
3.3	Absorption and emission spectra of Y series wavelength shifting fiber [18]. We use Y-11 for SuperFGD.	24
3.4	Block diagram of CITIROC.	25
3.5	Cosmic trigger detection from FEB HITS_OUT signals to MCB EVT_TRIGGER signal.	26
3.6	Conceptual drawing of the light injection method for a large number of channels and a picture of the LGP prototype [21].	26
3.7	Muon reconstruction efficiency as a function of true muon polar angle [22].	27
3.8	Proton reconstruction efficiency in current ND280 (red plots) and spectrum of generated protons according to NEUT MC (grey region) [14].	28

3.9	Proton reconstruction efficiency as a function of the true proton momentum. [15]	28
3.10	2D image of crosstalks.	30
3.11	Brief summary of the construction and installation.	31
4.1	Input detector geometries for Geant4 simulation without ECals, magnet, and sand walls (side view).	34
4.2	SuperFGD cube in the Geant4 simulation.	34
4.3	An example of the generated waveform.	38
4.4	2D and 3D event display of a cosmic event. The unit of 2D readouts is the number of photons.	38
4.5	Number of hits at each cube for one million cosmic events of our simulation. For the center of the top layer, the number of hits is about fifteen on average. For the edge of the bottom layer, the number of hits is about three on average.	39
5.1	Mean energy loss rate in some substances [31].	41
5.2	Display of hits for z fibers in a simulated cosmic ray event. Color represents the number of photoelectrons observed by each MPPC. The ‘single fiber hits’ are indicated by arrows.	42
5.3	Normalized charge distribution for four cubes.	43
5.4	Mean of q as a function of the distance to MPPC together with the fitting results.	43
5.5	Mean of q as a function of the distance to MPPC (black) with 1σ confidence interval at each position of the cube (red) using one million events for x and z fibers. Observed light yields are normalized by obtained attenuation curve.	44
5.6	Results of horizontal slice fits.	45
5.7	Mean of q as a function of the distance to MPPC (black) with 1σ confidence interval at each position of the cube (red) using 86 events for x and z fibers. Observed light yields normalized by obtained attenuation curve are also shown. Blue lines show the requirement (8.1%).	46
5.8	Distribution of length of tracks in each channel along the y direction.	46
5.9	Mean of q as a function of the distance to MPPC together with the fitting results.	47
5.10	Mean of q as a function of the distance to MPPC (black) with 1σ confidence interval at each position of the cube (red) using one million events for y fiber. Observed light yields are normalized by obtained attenuation curve. Points between the two blue vertical dot lines are used for fitting.	47
5.11	Mean of q as a function of the distance to MPPC (black) with 1σ confidence interval at each position of the cube (red) using 22 events for y fiber. Observed light yields are normalized by obtained attenuation curve. Horizontal blue lines show the requirement (8.1%) and points between the two blue vertical dot lines are used for fitting.	48
5.12	Time distribution of one photon events.	50
5.13	Attenuation curve including reflection $R = 0.05$ (pink) as the function of x in the case of 2 m fiber. Each component L_1 to L_4 is also shown.	52
5.14	Fitting result of fiber attenuation. R in the simulation is 5%. The fitting function includes reflection terms.	53

5.15	True mean of q as a function of the distance to MPPC together with fitting curve not including attenuation term (left). The ratio of true points and fit curve (right).	54
6.1	Definition and result of the beam test at CERN [30].	56
6.2	Crosstalk from the central cube to adjacent cubes [28].	56
6.3	True energy deposit in a channel normalized by path length for x fiber.	57
6.4	Three successive single-cube hits. The red cube is the main cube and the blue cubes are the crosstalk cubes.	58
6.5	Observed light distribution of main and crosstalk channels.	58
6.6	Predicted charge distributions by changing κ . $\kappa = 0.034$ is the same as what we use in the simulation.	59
6.7	χ^2 distribution by changing κ . The number of degrees of freedom is 7.	59
6.8	The effect of Birks quenching effect. For cosmic muons $dE/dX = 1.5$.	60
7.1	A schematic view of muon antineutrino events. The energy of the neutron is estimated using two timing, t_1 and t_2 [36].	62
7.2	True time resolution coming from the decay time of the fiber. The time difference between 3rd photons (2.5 p.e. threshold) is considered. We assume 8 ns as a decay time.	63
7.3	The scintillator cube which also has hits on both of two other fibers than the fiber in question and the closest to the MPPC is identified as the position of the track.	64
7.4	Distributions of t_{diff} (left). The distribution is asymmetry because of the time-walk effect. Distributions of observed light yield (right). Events with more than 20 p.e. are used for time offset calibration.	65
7.5	Input offset distribution of x fibers.	66
7.6	t_{diff} distribution of each channel (x fiber, before correction).	66
7.7	Result of the first iteration.	67
7.8	t_{diff} distribution of each channel (x fiber, after correction).	67
7.9	Result of the second iteration.	67
7.10	Fiber time-walk. We need to subtract time from the observed time according to this function.	69
7.11	Charges as a function of time assuming simple exponential rise. The threshold is 2.5 p.e.	69
7.12	MPPC-electronics time-walk. We need to subtract time from the observed time according to this distribution.	70
7.13	Timing and observed number of photons (x fiber).	70
7.14	Average t_{diff} with respect to the observed light yield.	71
7.15	Average t_{diff} with respect to the observed light yield together with 1σ confidence interval. The right figures are the average time shifted by the fit curve. 6,441 events are used and all the channels are summed up.	72
8.1	Schematic layout of the decay time measurement.	74
8.2	Picture of the dark box.	75
8.3	Jig for injecting laser into the fiber (hard foam).	75
8.4	Inside the dark box. Two frames run in the center to put the jigs.	76
8.5	Laser PLP-10 (C10196, M10306-30).	76

8.6	Diagram of readout circuit.	77
8.7	Digitizer DT5730.	77
8.8	Cut film placed in the connector.	78
8.9	Waveform of single photon event.	79
8.10	Signal height and integrated ADC distribution. We use events inside the red rectangular region as single photon events.	80
8.11	Time resolution of our setup.	80
8.12	Examples of time distributions and fit results. The position of injecting laser is 10 cm from the MPPC. The fitting range is below 80 p.e. to avoid the effect of the reflection seen around 87 ns.	81
8.13	Time resolution coming from the decay time of the fiber assuming 2.5 p.e. threshold. We assume 7.2, 3.7, 2.1, and 1.5 ns as decay times.	84
8.14	Observed p.e. from neutron simulation in SuperFGD. The left figure shows all light yields. The right figure shows the largest light yields in one event.	84

List of Tables

2.1	Accelerator upgrade summary.	18
3.1	The refractive index of each part of wavelength-shifting fiber Y-11 and its material.	22
4.1	Parameter value describing optical crosstalk used in the detector response simulation.	35
4.2	Parameter lists and values describing attenuation and reflection used in the detector response simulation.	35
4.3	Parameter lists and values describing MPPC in the detector response simulation	36
4.4	Parameter lists and values describing MPPC avalanche in the detector response simulation	37
4.5	Regions of integration for the calculation of cosmic muon flux.	39
5.1	Parameters used in the simulation and obtained by fittings.	42
5.2	Summary of statistical uncertainty assuming one-day data-taking and the systematic uncertainties for horizontal fibers.	44
5.3	Parameter values used in MC simulation and the obtained values for y fiber.	44
5.4	Summary of statistical uncertainty assuming one-day data-taking and systematic uncertainties for vertical fibers.	46
5.5	Parameters and values used for the calculation taken from [32].	51
5.6	Results of reflection measurement.	51
5.7	Statistical and systematic uncertainties related to fiber and light yield assuming cosmic data of one day.	54
6.1	Beam test results.	57
7.1	Required precision for the time resolution of each channel of SuperFGD.	62
7.2	Some results for decay time measurements for Y-11.	62
7.3	Uncertainties related to time offset calibration and time-walk correction assuming cosmic data of one day.	73
8.1	Transmission rate of two light-shielding films.	78
8.2	Results of decay time measurements. The position of injecting laser from MPPC is 10, 20, and 30 cm. Only statistical errors are shown.	82
8.3	Summary of decay times. Reference values 1 are obtained using pieces of plastic [41]. Reference values 2 are obtained using fibers [37].	82
8.4	Different conditions of reference measurement and our measurement.	82

8.5	Numbers of readouts with more than 40, 22, 12, and 10 p.e.	83
9.1	Achievable energy resolution of each channel using one-day cosmic data. . .	85
9.2	Expected precision of timing calibration using one-day cosmic data.	86

Bibliography

- [1] N. Chikuma. “Measurements of neutrino charged-current interactions on water and hydrocarbon targets using a sub-GeV anti-neutrino beam”. PhD thesis. The University of Tokyo, 2019. URL: https://hep.phys.s.u-tokyo.ac.jp/wp-content/uploads/2021/05/phd2019_nchikuma.pdf.
- [2] R.A. Smith et al. “Neutrino reactions on nuclear targets”. In: *Nuclear Physics B* 43 (1972), pp. 605–622. ISSN: 0550-3213. DOI: [https://doi.org/10.1016/0550-3213\(72\)90040-5](https://doi.org/10.1016/0550-3213(72)90040-5). URL: <https://www.sciencedirect.com/science/article/pii/0550321372900405>.
- [3] J. Nieves et al. “A theoretical approach to pionic atoms and the problem of anomalies”. In: *Nuclear Physics A* 554.4 (1993), pp. 509–553. ISSN: 0375-9474. DOI: [https://doi.org/10.1016/0375-9474\(93\)90245-S](https://doi.org/10.1016/0375-9474(93)90245-S). URL: <https://www.sciencedirect.com/science/article/pii/037594749390245S>.
- [4] Benhar et al. “Two-nucleon spectral function in infinite nuclear matter”. In: *Phys. Rev. C* 62 (3 Aug. 2000), p. 034304. DOI: [10.1103/PhysRevC.62.034304](https://doi.org/10.1103/PhysRevC.62.034304). URL: <https://link.aps.org/doi/10.1103/PhysRevC.62.034304>.
- [5] J. Nieves et al. “Inclusive charged-current neutrino-nucleus reactions”. In: *Phys. Rev. C* 83 (4 Apr. 2011), p. 045501. DOI: [10.1103/PhysRevC.83.045501](https://doi.org/10.1103/PhysRevC.83.045501). URL: <https://link.aps.org/doi/10.1103/PhysRevC.83.045501>.
- [6] M. Martini et al. “Unified approach for nucleon knock-out and coherent and incoherent pion production in neutrino interactions with nuclei”. In: *Phys. Rev. C* 80 (6 Dec. 2009), p. 065501. DOI: [10.1103/PhysRevC.80.065501](https://doi.org/10.1103/PhysRevC.80.065501). URL: <https://link.aps.org/doi/10.1103/PhysRevC.80.065501>.
- [7] K. Abe et al. “The T2K experiment”. In: *Nuclear Instruments and Methods in Physics Research Section A: Accelerators, Spectrometers, Detectors and Associated Equipment* 659.1 (2011), pp. 106–135. ISSN: 0168-9002. DOI: <https://doi.org/10.1016/j.nima.2011.06.067>. URL: <https://www.sciencedirect.com/science/article/pii/S0168900211011910>.
- [8] K. Matsuoka et al. “Design and performance of the muon monitor for the T2K neutrino oscillation experiment”. In: *Nuclear Instruments and Methods in Physics Research Section A: Accelerators, Spectrometers, Detectors and Associated Equipment* 624.3 (2010), pp. 591–600. ISSN: 0168-9002. DOI: <https://doi.org/10.1016/j.nima.2010.09.074>. URL: <https://www.sciencedirect.com/science/article/pii/S016890021002098X>.

- [9] K. Abe et al. “T2K neutrino flux prediction”. In: *Phys. Rev. D* 87 (1 Jan. 2013), p. 012001. DOI: [10.1103/PhysRevD.87.012001](https://doi.org/10.1103/PhysRevD.87.012001). URL: <https://link.aps.org/doi/10.1103/PhysRevD.87.012001>.
- [10] D Allan et al. “The electromagnetic calorimeter for the T2K near detector ND280”. In: *Journal of Instrumentation* 8.10 (Oct. 2013), P10019. DOI: [10.1088/1748-0221/8/10/P10019](https://doi.org/10.1088/1748-0221/8/10/P10019). URL: <https://dx.doi.org/10.1088/1748-0221/8/10/P10019>.
- [11] P.-A. Amaudruz et al. “The T2K fine-grained detectors”. In: *Nuclear Instruments and Methods in Physics Research Section A: Accelerators, Spectrometers, Detectors and Associated Equipment* 696 (2012), pp. 1–31. ISSN: 0168-9002. DOI: <https://doi.org/10.1016/j.nima.2012.08.020>. URL: <https://www.sciencedirect.com/science/article/pii/S0168900212008789>.
- [12] Dana Douqa on behalf of the T2K ND280 Upgrade group. “The SuperFGD for the T2K near detector upgrade”. In: *Journal of Physics: Conference Series* 1690.1 (Dec. 2020), p. 012070. DOI: [10.1088/1742-6596/1690/1/012070](https://doi.org/10.1088/1742-6596/1690/1/012070). URL: <https://dx.doi.org/10.1088/1742-6596/1690/1/012070>.
- [13] K. Abe et al. “Improved constraints on neutrino mixing from the T2K experiment with 3.13×10^{21} protons on target”. In: *Phys. Rev. D* 103 (11 June 2021), p. 112008. DOI: [10.1103/PhysRevD.103.112008](https://doi.org/10.1103/PhysRevD.103.112008). URL: <https://link.aps.org/doi/10.1103/PhysRevD.103.112008>.
- [14] K. Abe et al. “T2K ND280 Upgrade – Technical Design Report”. In: (2019). eprint: [arXiv:1901.03750](https://arxiv.org/abs/1901.03750).
- [15] A Blondel, M Zito, and M Yokoyama. *The T2K-ND280 upgrade proposal*. Tech. rep. 2018. URL: <https://cds.cern.ch/record/2299599/files/SPSC-P-357.pdf>.
- [16] *General Purpose Plastic Scintillator*. 2021. URL: https://eljentechnology.com/images/products/data_sheets/EJ-200_EJ-204_EJ-208_EJ-212.pdf.
- [17] Sergei Fedotov et al. “Scintillator cubes for 3D neutrino detector SuperFGD”. In: (2021). DOI: [10.48550/ARXIV.2111.07305](https://doi.org/10.48550/ARXIV.2111.07305). URL: <https://arxiv.org/abs/2111.07305>.
- [18] *Plastic Scintillating Fibers*. URL: https://www.kuraray.co.jp/uploads/5a717515df6f5/PR0150_psf01.pdf.
- [19] *MPPC S13360 Series*. 2022. URL: https://www.hamamatsu.com/content/dam/hamamatsu-photronics/sites/documents/99_SALES_LIBRARY/ssd/s13360_series_kapd1052e.pdf.
- [20] *Datasheet Citiroc1A*. URL: <https://www.weeroc.com/my-weeroc/download-center/citiroc-1a/16-citiroc1a-datasheet-v2-5/file>.
- [21] T Arihara et al. “Development of the in-situ Calibration System using LEDs and Light Guide Plates for the SuperFGD”. In: *Journal of Physics: Conference Series* 2374.1 (Nov. 2022), p. 012118. DOI: [10.1088/1742-6596/2374/1/012118](https://doi.org/10.1088/1742-6596/2374/1/012118). URL: <https://dx.doi.org/10.1088/1742-6596/2374/1/012118>.
- [22] Davide Sgalaberna. “The T2K ND280 upgrade”. In: vol. 390. 2021. URL: <https://www.scopus.com/inward/record.uri?eid=2-s2.0-85105444274&partnerID=40&md5=67d681a3016f88c373547c6d54eb3461>.

- [23] A. Eguchi. “Development of Selection Algorithms for Electron Neutrino Interaction Events with New T2K Near Detectors”. MA thesis. The University of Tokyo, 2021. URL: https://hep.phys.s.u-tokyo.ac.jp/wp-content/uploads/2021/05/mth2021_eguchi.pdf.
- [24] S. Kuribayashi. “T2K 実験における新型ニュートリノ検出器 Super FGD のための研究開発”. Japanese. MA thesis. Kyoto University, 2020. URL: https://www-he.scphys.kyoto-u.ac.jp/theses/master/kuri_mt.pdf.
- [25] *Overview*. URL: <https://geant4.web.cern.ch>.
- [26] D. Reyna. “A Simple Parameterization of the Cosmic-Ray Muon Momentum Spectra at the Surface as a Function of Zenith Angle”. In: (2006). eprint: [arXiv:hep-ph/0604145](https://arxiv.org/abs/hep-ph/0604145).
- [27] V. Khachatryan et al. “Measurement of the charge ratio of atmospheric muons with the CMS detector”. In: *Physics Letters B* 692.2 (2010), pp. 83–104. ISSN: 0370-2693. DOI: <https://doi.org/10.1016/j.physletb.2010.07.033>. URL: <https://www.sciencedirect.com/science/article/pii/S0370269310008725>.
- [28] O. Mineev et al. “Beam test results of 3D fine-grained scintillator detector prototype for a T2K ND280 neutrino active target”. In: *Nuclear Instruments and Methods in Physics Research Section A: Accelerators, Spectrometers, Detectors and Associated Equipment* 923 (2019), pp. 134–138. ISSN: 0168-9002. DOI: <https://doi.org/10.1016/j.nima.2019.01.080>. URL: <https://www.sciencedirect.com/science/article/pii/S0168900219301500>.
- [29] I. Alekseev et al. “SuperFGD prototype time resolution studies”. In: (2022). eprint: [arXiv:2206.10507](https://arxiv.org/abs/2206.10507).
- [30] A. Blondel et al. “The SuperFGD Prototype charged particle beam tests”. In: *Journal of Instrumentation* 15.12 (Dec. 2020), P12003. DOI: [10.1088/1748-0221/15/12/P12003](https://doi.org/10.1088/1748-0221/15/12/P12003). URL: <https://dx.doi.org/10.1088/1748-0221/15/12/P12003>.
- [31] Particle Data Group. “Review of Particle Physics”. In: *Progress of Theoretical and Experimental Physics* 2022.8 (Aug. 2022). 083C01. ISSN: 2050-3911. DOI: [10.1093/ptep/ptac097](https://doi.org/10.1093/ptep/ptac097). eprint: <https://academic.oup.com/ptep/article-pdf/2022/8/083C01/45434166/ptac097.pdf>. URL: <https://doi.org/10.1093/ptep/ptac097>.
- [32] S. Fedotov. “New 3D fine-grained scintillation detector for the T2K experiment”. In: *Journal of Instrumentation* 15.07 (July 2020), p. C07042. DOI: [10.1088/1748-0221/15/07/C07042](https://doi.org/10.1088/1748-0221/15/07/C07042). URL: <https://dx.doi.org/10.1088/1748-0221/15/07/C07042>.
- [33] K. Iwamoto et al. “Performance Evaluation of a Fine-Grained Scintillator Tracker for the T2K Near Detector Upgrade Project”. In: *ELPH annual report* (2019), pp. 70–76. ISSN: 21867968. URL: <https://cir.nii.ac.jp/crid/1520572360187054208>.
- [34] M. Hasegawa. “Measurement of Neutrino Oscillation Parameters with Neutrino-Nucleus Interaction Studies in the K2K Experiment”. PhD thesis. Kyoto University, 2006. URL: https://www-he.scphys.kyoto-u.ac.jp/theses/doctor/masaya_dt.pdf.
- [35] M. Hirschberg et al. “Precise measurement of Birks kB parameter in plastic scintillators”. In: *IEEE Transactions on Nuclear Science* 39.4 (1992), pp. 511–514. DOI: [10.1109/23.159657](https://doi.org/10.1109/23.159657).

- [36] L. Munteanu et al. “New method for an improved antineutrino energy reconstruction with charged-current interactions in next-generation detectors”. In: *Phys. Rev. D* 101 (9 May 2020), p. 092003. DOI: [10.1103/PhysRevD.101.092003](https://doi.org/10.1103/PhysRevD.101.092003). URL: <https://link.aps.org/doi/10.1103/PhysRevD.101.092003>.
- [37] I. Alekseev et al. “The performance of a new Kuraray wavelength shifting fiber YS-2”. In: *Journal of Instrumentation* 17.01 (Jan. 2022), P01031. DOI: [10.1088/1748-0221/17/01/P01031](https://doi.org/10.1088/1748-0221/17/01/P01031). URL: <https://dx.doi.org/10.1088/1748-0221/17/01/P01031>.
- [38] V Brekhovskikh et al. *The WLS fiber time properties study*. Tech. rep. Geneva: CERN, 2000. URL: <https://cds.cern.ch/record/691514>.
- [39] *Short Decay time Wavelength Shifter(YS-series)*. Only YS-2 information is officially released. 2020. URL: http://kuraraypsf.jp/pdf/YSSeries_201007.pdf.
- [40] *Low Cost, 80 MHz FastFET Op Amps AD8033/AD8034*. URL: https://www.analog.com/media/en/technical-documentation/data-sheets/AD8033_8034.pdf.
- [41] R. Abe et al. サンドイッチ型カロリメーターへの応用をめざした放射光を使った短寿命波長変換シンチレーターの蛍光寿命測定. Japanese. 日本物理学会年次大会. Mar. 2022.